

2015

# Optical based thermal probing and characterization

Shen Xu

*Iowa State University*

Follow this and additional works at: <https://lib.dr.iastate.edu/etd>

 Part of the [Mechanical Engineering Commons](#)

## Recommended Citation

Xu, Shen, "Optical based thermal probing and characterization" (2015). *Graduate Theses and Dissertations*. 14738.  
<https://lib.dr.iastate.edu/etd/14738>

This Dissertation is brought to you for free and open access by the Iowa State University Capstones, Theses and Dissertations at Iowa State University Digital Repository. It has been accepted for inclusion in Graduate Theses and Dissertations by an authorized administrator of Iowa State University Digital Repository. For more information, please contact [digirep@iastate.edu](mailto:digirep@iastate.edu).

# Optical based thermal probing and characterization

by

**Shen Xu**

A dissertation submitted to the graduate faculty  
in partial fulfillment of the requirements for the degree of

DOCTOR OF PHILOSOPHY

Major: Mechanical Engineering

Program of Study Committee:  
Xinwei Wang, Major Professor  
Gap-Yong Kim  
Hui Hu  
Shan Hu  
Sriram Sundararajan

Iowa State University

Ames, Iowa

2015

Copyright © Shen Xu, 2015. All rights reserved.

## TABLE OF CONTENTS

	Page
LIST OF FIGURES .....	iv
LIST OF TABLES .....	viii
ACKNOWLEDGEMENTS .....	ix
ABSTRACT .....	xi
CHAPTER 1 INTRODUCTION .....	1
1.1. Photothermal technique development and applications in spider silk films .....	1
1.2. Raman scattering for structural characterization and thermometry .....	6
1.3. Scope of present work .....	12
CHAPTER 2 PHOTOTHERMAL TECHNIQUE USING AMPLITUDE PROFILE .....	13
2.1. Physics of the method .....	13
2.2. Across-plane thermal characterization of SiC and SiO <sub>2</sub> films on Si .....	19
2.3. Sensitivity study of parameters .....	28
CHAPTER 3 PHOTOTHERMAL CHARACTERIZATION OF CROSS-PLANE THERMAL TRANSPORT IN SPIDER SILK FILM .....	34
3.1. Sample preparations .....	34
3.2. Structure characterization using Raman spectroscopy .....	36
3.3. Thermal energy transport .....	41
CHAPTER 4 RAMAN SPECTROSCOPY FOR NANOSTRUCTURE PROBING .....	55
4.1. Experimental details .....	55
4.2. Results and discussions .....	58
CHAPTER 5 TIME-DOMAIN DIFFERENTIAL RAMAN FOR THERMAL PROBING .....	68
5.1. Time-domain differential Raman: physics and experimental setup .....	68
5.2. Si cantilever measurement: Raman spectrum variation against $t_e$ .....	73
5.3. Physical model for temperature evolution .....	78
5.4. Physical model and numerical reconstruction of Raman spectrum .....	79
5.5. Thermal diffusivity determination based on $\omega$ and $E^*$ .....	83
5.6. Physical analysis and experimental uncertainty evaluation .....	85
5.7. Thermal diffusivity determination based on total Raman emission .....	89

CHAPTER 6 SUMMARY AND FUTURE WORK .....	93
6.1. Summary .....	93
6.2. Future work: extended application of TD Raman.....	96
REFERENCES .....	99

## LIST OF FIGURES

- |   | Page |
|---|------|
| Figure 2.1. (a) Schematic of an N-layer sample. It shows the multiple layers model. The $x$ axis is along the thickness direction of the model. (b) The experimental setup of the PT technique.   | 14   |
| Figure 2.2. (a) The fitting result based on the phase shift method for the 2.5 $\mu\text{m}$ SiC film on Si. The thermal conductivity is determined at 3.72 W/m K. The statistical uncertainty $\xi$ is much smaller than $\phi_{nor}$ , indicating the accuracy of the measurement. Curves with thermal conductivities of 3.42 W/m·K and 4.02 W/m·K demonstrate the fitting uncertainty. (b) The raw data of samples and the calibration amplitude (inset plot). (c) The fitting result based on the amplitude method. The normalized amplitude $A_{nor}$ (black dots) increases against the frequency $f$ . The thermal conductivity is determined at 3.58 W/m K.   | 21   |
| Figure 2.3. Raman spectra of the SiC samples and bulk 4H-SiC single crystal under the same measurement condition. The bulk SiC single crystal shows clear sharp peaks indicating good crystalline structures, while the CVD SiC samples only have broad peaks demonstrating their amorphous structures.   | 25   |
| Figure 2.4. Fitting results based on the phase shift and the amplitude methods for the 500 nm thick SiO <sub>2</sub> film on Si. With the phase shift method, the thermal conductivity is determined to be 1.31 W/m K. Theoretical curves with thermal conductivities of 1.24 W/m·K and 1.37 W/m·K demonstrate the fitting uncertainty. Based on the amplitude method, the thermal conductivity is determined to be 1.68 W/m K. The fitting uncertainty is illustrated with curves of thermal conductivities of 1.51 W/m·K and 1.85 W/m·K.  | 28   |
| Figure 2.5. (a) Residual of the least square method against the thermal contact resistance $R''_{\text{Si,SiC}}$ for sample 1. The residual does not change much against $R''_{\text{Si,SiC}}$ until it is larger than $10^{-7} \text{ m}^2 \cdot \text{K/W}$ , so the amplitude method is not sensitive to $R''_{\text{Si,SiC}}$ . (b) The ratio $A_{nor,f}/A_{nor,400 \text{ Hz}}$ against the frequency with all parameters from sample 1. The rest parameters for sample 1 are fixed for these two plots: $k$ is 3.58 W/m K, $\rho$ is 3160 kg/m <sup>3</sup> , $c_p$ is 690 J/kg K, and $d$ is 2.5 $\mu\text{m}$ , and $R''_{\text{Si,SiC}}$ is $1.51 \times 10^{-7} \text{ m}^2 \text{ K/W}$ for Fig. 2.4b. | 30   |
| Figure 3.1. (a) <i>L. hesperus</i> major ampullate gland, scale bar = 1 mm. (b) <i>N. clavipes</i> major ampullate gland (left image, scale bar = 1 mm) and HFIP film (right image). Note translucence and bright yellow color of the silk.   | 35   |
| Figure 3.2. Raman spectra from 500 $\text{cm}^{-1}$ to 1750 $\text{cm}^{-1}$ for <i>N. clavipes</i> (a) HFIP film (b) fresh film, and for <i>L. hesperus</i> (c) HFIP film and (d) fresh film. This region is tightly related to internal structures of silk films.   | 37   |

Figure 3.3. (a) The mechanism of the PT experiment showing the sample structure. (b) Raw phase shift  $\phi_{raw}$  (purple squares), real phase shift  $\phi_{re}$  after calibration (red dots), and the fitting curve (black line). The thermal conductivity is determined at 0.270 W/m·K. Theoretical curves with thermal conductivity of 0.243 W/m·K (green line) and 0.297 W/m·K (blue line) demonstrate the fitting uncertainty. The theoretical fitting agrees well with experimental data. (c) Normalized amplitude  $A_{nor}$  (red dots) and raw amplitude  $A_{raw}$  (purple squares) change with the frequency. 42

Figure 3.4. (a) Raman spectra of the thickened major ampullate HFIP silk film of *N. clavipes* heated under different temperatures. The observed crystallization happens at 60 °C as peaks shift to the wavenumber representing  $\alpha$ -helices in the Raman spectrum. These Raman peaks weaken and disappear gradually under continued heating processes. (b) The effusivity with error bars of this film after heat treatment at different temperatures. 50

Figure 3.5. (a) Raman spectra of the thickened major ampullate HFIP silk film of *L. hesperus* heated under different temperatures. The observed crystallization happens at 60 °C as some clear and representative peaks appear in the Raman spectrum. This crystal structure disappears after being heated at 80 °C. (b) The effusivity with error bars of this film after heat treatment at different temperatures. 52

Figure 4.1. (a) is a schematic of the experimental setup for Raman experiment with a 100× objective lens (not to scale). The relative location of the laser spot moves along the x direction shown by green arrow. Red dots show the approximate positions of A, B, C spots. A is mostly near the edge, then B, and C is farthest to the edge; (b) are three the Raman spectra of silicon near 521 cm<sup>-1</sup> at selected spots A, B, and C. The dots represent the raw data and curves are from Gaussian fitting, and both of them have the baseline subtracted. For clear comparison, the curves A and B are shifted up, and 0 points of their y coordinates are shown in the plot; (c) scanning electron micrograph (SEM) shows a smooth surface. The right half of the image is the area which is out focus and shown black, while the left half is the silicon wafer surface. The boundary of the silicon wafer is indicated by white arrows. (d) Atomic force microscopy (AFM) image of the silicon wafer surface is also taken in the same place like that in SEM. The inset plot is the profile of the cross-section measured along the direction of black dash arrow in upper right side of Fig. 4.1d. The boundary of the silicon wafer is indicated by black arrows. 57

Figure 4.2. Raman imaging results from the center to the edge of 270 μm thick silicon wafer. (a) Peak intensity ( $I$ ). The laser spot size is calculated from the highest intensity to 10% of maximum intensity in this plot, (b) width ( $\Gamma$ ), (c) 521 cm<sup>-1</sup> peak wavenumber shift ( $\omega$ ), and (d) size of nanocrystalline silicon grain ( $d$ ) change with focal spot from the center to the edge, calculated from  $d = 2\pi\sqrt{B/\Delta\omega}$  in ref.[52]. The red line in this plot shows the actual position of the edge. 59

- Figure 4.3. Variation of the Raman spectrum from different focal levels on two single crystal silicon wafers. (a) Peak intensity ( $I$ ), (b) width ( $\Gamma$ ), and (c)  $521\text{ cm}^{-1}$  peak wavenumber shift ( $\omega$ ) change with the distance to the focal point. The solid legends represent Raman information for the  $270\text{ }\mu\text{m}$  thick Si wafer and the hollow ones are for the  $7\text{ }\mu\text{m}$  thick Si wafer. The red line in this plot shows the  $0\text{ nm}$  position in the  $z$  direction and the laser beam is well focused on this level. 61
- Figure 4.4. Relationship between Raman intensity  $I$  and nanocrystalline grain size  $d$  in the  $270\text{ }\mu\text{m}$  thick silicon wafer and  $7\text{ }\mu\text{m}$  thick silicon wafers.  $I$  is decreasing with the grain size increasing. The solid line is used to guide eyes for the data trend. 65
- Figure 4.5. Raman imaging results from the center to the edge of  $7\text{ }\mu\text{m}$  thick silicon wafer. (a) Peak intensity ( $I$ ), (b) width ( $\Gamma$ ), (c)  $521\text{ cm}^{-1}$  peak wavenumber shift ( $\omega$ ), (d) size of nanocrystalline silicon ( $d$ ) change with focal spot from the center to the edge. The red line in this plot shows the actual position of the edge. (e) AFM image of the silicon wafer surface close to Raman testing area. The inset plot is the cross-sectional profile measured along the direction of black dash arrow in the left, and the edge of the wafer is located in the lower left (black area). 67
- Figure 5.1. (a) Timing profiles of the laser pulse and the temperature evolution, and instant changes of Raman peak intensity ( $I$ ), peak shift ( $\omega$ ) and linewidth ( $\Gamma$ ). Along with the heating, the temperature in the sample increases, and then the Raman peak intensity decreases, the wavenumber softens and linewidth broadens. In TD Raman, the laser heating time is increased a little bit ( $\Delta t_e$ ) each time from Case 1 to Case 3. Therefore, the temperature of the heated region will experience more increase (before reaching the steady state) from Case 1 to Case 3. This extended temperature rise will give rise to a slight change in the Raman spectrum collected during the heating period. (b) The corresponding temporally accumulative Raman spectra of one cycle in three cases. Slight Raman peak softening due to the increased differential heating time is marked in the figure. The peak intensity increases largely because of the longer excitation period. The heating induced intensity decrease is less obvious in these spectra, but is visible via further peak analysis. 70
- Figure 5.2. (a) The optical microscope view of the tipless Si cantilever. It is  $450.35\text{ }\mu\text{m}$  long and  $49\text{ }\mu\text{m}$  wide. The tip has a height of  $22.95\text{ }\mu\text{m}$ . (b) Schematic of laser spot position on the cantilever tip. The effective heating region is marked with  $x_1$  and  $x_2$  on the  $x$  coordinate in the physical model.  $l_e (= x_2 - x_1)$  is  $19.9\text{ }\mu\text{m}$  indicating the effective length of the heating region on the cantilever.  $L$  is the total effective length ( $438.9\text{ }\mu\text{m}$ ) used for the cantilever in the physical model. 74
- Figure 5.3. The evolution of the Si Raman peak against the increase of excitation/heating duty in the experiment. (a) Spectra per cycle under different excitation time of  $t_e$ : —  $0.24\text{ ms}$ , —  $0.4\text{ ms}$ , —  $0.68\text{ ms}$ , —  $1.16\text{ ms}$ , —  $1.72\text{ ms}$ , —  $4.2\text{ ms}$ , and —  $10\text{ ms}$ . As the excitation/heating time becomes longer, the Raman peak in one cycle increases and softens to the left. (b) Raman emission  $E_\omega$  ( $\blacktriangle$  to

the left y axis) increase against  $t_e$ , but the rate  $\partial E_\omega / \partial t_e$  declines quickly at the beginning and then slows down to a constant. The normalized Raman emission  $E_\omega^*$  (♦ to the right y axis) decreases to a steady state value as  $t_e$  become longer.  $E_\omega^*$  directly illustrates that the Raman emission per unit time decreases against the heating time. (c) Raman linewidth variation against the excitation time. Although an increasing trend is observed for the linewidth against increased excitation time, large noises are observed in linewidth data due to the less sensitivity of linewidth to temperature variation. So this data is less applicable for thermal diffusivity determination. (d) A clear decline in the wavenumber against  $t_e$  makes wavenumber  $\omega$  a good parameter for determining  $\alpha$  of the cantilever. 76

Figure 5.4. (a) The evolution of the reconstructed Si Raman spectrum per cycle with the numerical method against the increase of Fourier number  $Fo_e(t_e)$ : — 0.028, — 0.047, — 0.079, — 0.14, — 0.20, — 0.49, and — 1.17. The Raman peak in one cycle increases and softens to the left against the increased  $Fo_e$ . This echoes the one in Fig. 5.3a. (b) The decreasing trends of the normalized Raman intensity  $E_\omega^*$  and (c) the Raman shift  $\omega$  against the Fourier number  $Fo_e$  well agree with the trends in the experiment. 82

Figure 5.5. (a) Variation of normalized intensity against the excitation time. It decreases as  $t_e$  is increasing to a steady state value. The red curve with  $\alpha_{E_\omega^*}$  of  $9.17 \times 10^{-5} \text{ m}^2/\text{s}$  best fits the experimental data based on the intensity method. (b) Wavenumber shift to the steady state against the excitation time. The best fitted curve with  $\alpha_\omega$  of  $8.14 \times 10^{-5} \text{ m}^2/\text{s}$  is shown red. Error bars in both figures show the uncertainty in the measurement, and curves with 10% deviation in both thermal diffusivities are shown in blue and green. They show obvious difference from the best fitted results indicating the sensitivity of the normalized Raman intensity method and wavenumber shift method, respectively. 85

Figure 5.6. The experimental data fitting based on the peak area with the best fitted curve with  $\alpha_{E^*} = 9.51 \times 10^{-5} \text{ m}^2/\text{s}$ . The measurement uncertainty is shown using error bars. The sensitivity of the total Raman emission method to  $\alpha$  is shown with  $\alpha = 8.56 \times 10^{-5} \text{ m}^2/\text{s}$  and  $\alpha = 10.47 \times 10^{-5} \text{ m}^2/\text{s}$ , respectively. A visible deviation is observed from the best fitted result when  $\alpha$  changes with 10%. 91

## LIST OF TABLES

	Page
Table 2.1. Thermal conductivity determination based on phase shift and amplitude.	24
Table 3.1. Detailed assignment of major peaks in Raman spectra of <i>N. clavipes</i> and <i>L. hesperus</i> major ampullate silk films [85, 86].	38
Table 3.2. Thermophysical properties determination based on phase shift and amplitude.	44

## ACKNOWLEDGEMENTS

I would like first offer my appreciation to my advisor and also my committee chair, Dr. Xinwei Wang for the opportunity of joining the Micro/Nanoscale Thermal Science Laboratory and engaging in my Ph. D. projects. His expertise in thermal science and experimental skills improved my research ability and prepared me for future challenges. Without Dr. Wang's guidance, I would not have been able to obtain these great achievements. Next, I would like to sincerely thank my committee members, Dr. Gap-Yong Kim, Dr. Hui Hu, Dr. Sriram Sundararajan, Dr. Shan Hu, and Dr. Terry Meyer, for their suggestion throughout the course of my Ph. D. project and research and for their helpful comments on my preliminary exam, and Dr. Reza Montazami for his substituting for Dr. Sriram Sundararajan on my final examination committee. I am also grateful to Dr. Cheryl Hayashi, Dr. David Hurley, and Dr. Yongfeng Lu for their valuable advices on my works.

Next, I would like to thank all my colleagues in the Micro/Nanoscale Thermal Science Laboratory for supporting my research, especially Zaoli Xu, Tianyu Wang, Xiaoduan Tang, and Yanan Yue, Xiangwen Chen, Nathan Van Velson, and James Starrett of University of California, Riverside. Greatly appreciate to the help from Chris Reilly and Kelsey Burney for proofreading my manuscript. Also thanks very much to my friends, the department faculty and staff for making my time at Iowa State University a wonderful experience. Also thanks to my family for their support and encouragement.

Finally, the financial support of these researches by the National Science Foundation (CMMI-0926704, CMMI-1200397, and CBET-1235852), Army Research Office (W911NF-12-

1-0272), and Office of Naval Research (N000141210603), “Taishan Scholar” program of Shandong Province, China are gratefully acknowledged.

## ABSTRACT

Optical methods are promising tools for small-scale thermal probing and characterization. A lab-developed photothermal (PT) technique provides a noncontact method to characterize the thermal transport along the thickness direction of a multilayered film by analyzing the phase shift of the thermal radiation from the sample's surface. Aiming to reduce the calibration in the phase shift method, a new amplitude method is developed on the basis of the amplitude of the thermal radiation signal. The new method successfully performs the thermal measurements for chemical vapor deposited SiC films, thermally oxidized SiO<sub>2</sub> film on silicon substrates, and spider silk films. Furthermore, weak-sensitivity to the thermal contact resistance enables the amplitude method to lower the effect of thermal contact resistance on thermal conductivity determination. The normalized amplitude ratio of a high frequency to a low frequency provides a reliable way to evaluate the effusivity ratio of the film to that of the substrate. For spider silk films, the contribution to the thermal conductivity from  $\alpha$ -helices and antiparallel  $\beta$ -sheets in silk proteins against the temperature has been studied.

Raman spectroscopy is better than PT since its scatterings involve not only the structure information of a sample but also physical properties, like temperature and stress. The edge area of a mechanically cleaved Si wafer is studied using Raman spectroscopy. The appearance of nanocrystals there is proved and it accounts for the abnormal increase in Raman intensity when the grain size of nanocrystals varies from 20 to 10 nm. For transient thermal probing and characterization, a time-domain differential Raman technique is developed using a square-wave modulated laser. The varying duty cycle of the modulation signal realizes controlled heating and

transient thermal probing based on Raman thermometry and transient electrothermal technique. A validation experiment is conducted on a tipless Si cantilever. Physical models are later constructed to simulate the variation of the cumulative Raman spectra over one excitation period and to determine the thermal diffusivity of the cantilever. The resulting thermal diffusivity is well agreed with the theoretically determined reference value.

## CHAPTER 1

### INTRODUCTION

Optical based probing methods attract more attentions than others in recent scientific and industrial fields due to the unique features of laser sources: high accuracy of collimation, high special resolution, good controllability, non-invasiveness and nondestructiveness. Therefore, the advancement of optical based thermal probing and characterization methods become more important.

#### 1.1. Photothermal technique development and applications in spider silk films

Film materials play a basic role in today's industry, since the knowledge of the thermophysical properties of films in and cross plane is necessary in the thermal design of devices. Many techniques have been developed over past decades to measure the thermophysical properties of thin films. One important class is the  $3\omega$  method [1-3]. It utilizes a microfabricated metal line deposited on the specimen to act as a resistive heater. An AC current is then fed through the metal line with a frequency of  $\omega$ . The periodic heating generates a temperature variation and oscillations in the electrical resistance at the second harmonic frequency, thus leading to a  $3\omega$  variation in the voltage. The resulting amplitude and phase shift of this third harmonic voltage signal reflect the thermophysical properties of the film. The  $3\omega$  method gives a relatively high signal-to-noise ratio. The  $I$ - $V$  behavior and the temperature coefficient of the resistance of the studied film need to be known or calibrated separately, which may increase the complexity of the measurement.

Another class of techniques, known as the pump-probe technique, employs optical and noncontact measurements to study thin films' properties. A feature of the pump-probe technique is the use of ultrafast lasers to measure transient events on picoseconds time. The technique has been widely applied in diverse fields such as ultrafast spectroscopy [4, 5], photo-acoustics [6, 7], Terahertz imaging [8], and etc. Among typical thermal characterization methods, transient thermoreflectance (TTR) technique [9] is a widely used pump-probe type of measurement. Two ultrafast laser pulses of a few picoseconds pulse width or shorter irradiate the sample surface. The first pulse heats the sample and leads to the reflectance change of the sample surface, while the second pulse is weaker and slightly delayed to probe this reflectance variation. The resulting change in the reflectivity is linearly proportional to the temperature change within a small temperature range [10, 11]. The TTR technique using ultrashort pulsed lasers has been demonstrated as an effective tool for measuring the thermophysical and mechanical properties of thin film materials, but challenges exist when one wants to study the interfacial thermal transport between layers [12].

The photoacoustic (PA) technique, another class of the pump-probe methods, correlates acoustic signals with the incident light for thermophysical property measurements. Rosencwaig and Gersho [13] first developed the RG model to understand the PA phenomenon. Since then, many works based on this model have been carried out and focused on thermal transport in multilayer samples [14-17]. Briefly, a modulated laser is focused on the sample surface to generate local heating. The sample surface temperature variation is then detected by measuring the small pressure variations in the gas adjacent to the surface [18]. In the PA measurement, the

experimental setup for detecting sound wave needs to be carefully designed to reduce noises in the circumstance.

On the basis of the principle of the PA technology, the photothermal (PT) technique [19-21], developed in our lab, improves the measurement by detecting thermal radiation instead of acoustic signals from a sample's surface. In the PT technique, the phase shift between the measured thermal response (radiation) and the incident laser is frequently used. It is sensitive to the thermal conductivity along the thickness direction and interfacial resistances. As an extension of the PT technique, pulsed laser-assisted thermal relaxation (PLTR) technique [22, 23] has the capability of measuring the thermophysical properties of one-dimensional structures along the axial direction in a transient process. Photon works as a heat source and the voltage variation over a filament reflects the temperature change. PLTR2 technique [24] is a further improvement on the PLTR technique. It can simultaneously measure thermal properties of free-standing films along both in-plane and thickness directions. The amplitude of the radiation in the PT measurement, however, was not used so much for the characterization in previous work due to its susceptibleness to the circumstance.

The thermophysical properties of the film of interest are tightly related to its internal structures, such as crystalline or amorphous structures. The PT technique provides us with a new manner for structural characterization in a film through its thermal response after heated. It could even be applicable to study the structural evolution of the proteins in biomaterials during a special treatment, like spider silks. For over 50 years, spider silk has been recognized as a promising material due to its outstanding mechanical properties. With tensile strengths as high as

1.75 GPa and elongations of 26% - 35% [25-27], some spider silks surpass the toughness of steel. Spider silk also behaves like rubber on a weight to weight basis and can be two to three times as tough as Nylon or Kevlar [28]. In addition to these superb features, spider silk offers further advantages over inorganic polymers with its biocompatibility and biodegradability. The medical application of spider silks was described as early as 1901 [29, 30]. Spider silk outperforms almost all synthetic materials [31] due to its combination of mechanical strength and elasticity [32]. Moreover, the biomedical functionality of this material could be deployed for applications in tissue replacement [33, 34], suture [30, 35], drug carrier [33], ligament/tendon tissue [36], biomaterial scaffold [37, 38], and artificial blood vessels [29].

Compared with other kinds of fibers, the preeminent properties of spider silk come from its unique internal structure. A spider produces more than one type of silk for different usages. Among them, dragline silk is the most widely studied and has more desirable mechanical properties than others. Dragline silk, synthesized in the major ampullate glands in the abdomen of a spider, is composed of many parallel fibrils [39-41]. Spidroins (spider fibroins) are the main component of a silk fibril, and dragline silk in particular is composed of two spidroins, major ampullate spidroin 1 (MaSp1) and major ampullate spidroin 2 (MaSp2). In major ampullate silk, antiparallel  $\beta$ -sheets and random coils are the main secondary structures. Silk proteins are stored in high concentration inside of the glands lumens as a liquid crystalline solution [42]. The synthesis of dragline silk happens at the tail of the gland within specialized cells. The antiparallel  $\beta$ -sheets form during spinning.

One general approach to study the structure and properties of spider silk is to dissolve the silk protein in a solution, make a coating material to understand how the structure determines the physical properties, and then manipulate the structure [43]. Transmission electron microscopy (TEM) [44] has a higher resolution than standard optical microscopy making it very useful to observe the internal structure of spider silk film at the nanometer-scale. Fourier transform infrared spectroscopy (FTIR) [44, 45] can characterize detailed chemical bonds in spider silk proteins. Circular dichroism (CD) spectroscopy [45, 46] can analyze the  $\alpha$ -helices and the antiparallel  $\beta$ -sheets conformation of spider silk protein in a solvent.

In addition to the aforementioned techniques, Raman spectroscopy is a powerful method to characterize the internal structure of spider silks and it has been employed in many studies [43]. Most Raman spectra of different silk samples from various spiders show two major peaks about amide III ( $1220\text{-}1279\text{ cm}^{-1}$ ) and amide I ( $1650\text{-}1680\text{ cm}^{-1}$ ). These represent antiparallel  $\beta$ -sheets, which silks from silkworm also have. These two peaks have their own distinct locations when they are in the antiparallel  $\beta$ -sheets and their wavenumber shift when they are in random coils.

In spider silks, the intrinsic thermal transport capacity strongly depends on molecular weight, structure, crystallinity and alignment, while defects are the main source of reduction in strength and thermal conductivity. Under the same measurement condition, better internal structures (e.g., less defect, higher crystallinity, and better alignment) will lead to higher thermal transport properties. Therefore, thermal diffusivity and conductivity can be used as signatures to reflect protein structures of spider silks. These thermal transport properties can complement the

structural information determined by other techniques (e.g., XRD, SEM, FTIR), and provide new perspectives and understanding of the structure regularity and energy coupling in spider silk, as well as other synthetic and natural polymers. Unfortunately, very little research has been done on the thermal transport capacity in spider silks, thus, there has been very little use of this property to characterize its structure variation. According to Huang's discovery, the observed exceptionally high thermal conductivity of spider silk, from  $348.7 \pm 33.4$  to  $415.9 \pm 33.0$  W/m·K, is largely attributed to its extraordinary well-organized and less defective structures formed from strong self-assembly [47].

### 1.2. Raman scattering for structural characterization and thermometry

Raman scattering is not only available for structural characterization of molecular configuration and conformation in chemistry, but also relevant to physical properties of bulks, such as temperature and stress. In the Raman scattering, incident photons interact with optical phonons and exchange energy with those phonons. An inelastic scattering occurs in the meanwhile with emitting Raman signals: new photons have different frequency to the incident ones. Raman signals generally produce a Gauss or Lorentz peak in the spectrum. Intensity, wavenumber (or Raman shift) and linewidth (full width at half maximum, or FWHM) of Raman signals are tightly related to phonons' emission efficiency, frequency and finite lifetime [48, 49]. When temperature variation and stress effect are negligible in materials, the intensity, wavenumber, and linewidth can characterize the crystalline structures in nanocrystalline structure.

Nanocrystalline silicon, which is defined as a material composed of nano-size silicon crystalline grains [50], is popular in microelectronics and optoelectronic industry, such as gates, load resistors, and solar cells, because of its high performance. Compared with single crystalline silicon, nanocrystalline silicon can be easily recognized with visible grains and produced through various methods in different sizes, shape and purity [51]. Although amorphous silicon also has the above advantages, nanocrystalline silicon has a larger quantity of mobile charge carriers and is more stable under electric field and light-induced stresses.

In engineering applications of nanocrystalline silicon, it is important to obtain the knowledge of crystalline structures and relate such information to the desired functionality. Among different techniques, Raman spectroscopy is an effective way to characterize structure of crystals. In Raman spectrum, the lattice vibration mode in single crystalline silicon is observed as a sharp peak around  $521\text{ cm}^{-1}$ , while a broad peak centered at  $480\text{ cm}^{-1}$  represents the amorphous state because the breakdown of lattice periodicity relaxes the symmetry restrictions and permits scattering from all other vibrational modes. Nanocrystalline silicon is the intermediate state between these two forms so it is easily recognizable by fitting these two peaks in the spectrum [50]. The resulting peak intensity, linewidth, and wavenumber have a close and direct relationship with the structure of crystals. In Tong *et al.*'s work, the crystalline perfection can be detected from the intensity of the Raman peak by analyzing the ratio of intensity between the peaks at  $521\text{ cm}^{-1}$  and  $480\text{ cm}^{-1}$ . From the linewidth of the peak, the amount of lattice perturbation and residual internal strain can be investigated. Additionally, many models were developed to calculate the actual size of nanograin from the peak shift [52]. However, the Raman peak intensity is rarely used to characterize the profile of the nanocrystalline structure due to the

fact that the intensity can be influenced by many factors, such as the excitation laser level, optical alignment, and material surface roughness.

The information from the Raman spectrum mentioned above has also been used to characterize strains and stresses, and measure temperature in crystalline materials. Through Raman scanning near-field optical microscopy (RSNOM), Webster *et al.* [53] found that the degree of shift depended on the nature of stresses. The residual stress decreased with the positive shifts of the peak position of the Si's  $521\text{ cm}^{-1}$  peak as a function of the distance when approaching the scratch in their silicon sample.

Temperature variation will affect the thermal state of phonons and so as Raman signals. When the temperature of the detected surface goes up, wavenumber will become smaller, intensity will decrease, and linewidth will broaden. The relationship between temperature and wavenumber was calculated by Balkanski [54] and was also verified by many other researchers [55, 56]. Raman thermometry is then a manner analyzing Raman signal's variation to obtain the temperature and thermophysical properties of a system of interest.

Furthermore, due to its less invasive and nondestructive feature and high resolution in space, Raman thermometry has been widely used to determine the temperature of complicated and highly compacted structures and devices [57, 58]. Song, *et al.* [59] studied the thermal stability of single-walled carbon nanotube (SWCNT) rings with the Raman shift method in the range of 80-550 K. Beechem, *et al.* [60] mapped both temperature and stress distribution simultaneously with Raman shift of functioning polysilicon microheater. Lundt, *et al.* [61]

developed a micro-Raman thermometry with a spatial resolution of 280 nm by employing anatase TiO<sub>2</sub> microparticles.

Since the temperature of a studied system can be measured using Raman thermometry, the intrinsic thermal conductivity of the targeted material in the system can also be quantified. In popular 2D materials investigation, the thermal conductivity of a suspended thin layer of material can be determined from the correlation between input energy increase and resulting temperature increase, while the temperature rise is determined by variation in the Raman peak shift with a thermal coefficient from additional calibration. This optical based thermal properties characterization technique becomes a common tool to study the thermal conductivity of Raman active 2D materials, such as graphene [62] and extended materials from graphene family [63, 64], silicon nano-membranes [65], TaSe<sub>2</sub> thin films [66], and few-layer MoS<sub>2</sub> [67].

Interface energy coupling also can be investigated with Raman thermometry. Yue, *et al.* [68] successfully used a combination of Raman spectroscopy and Joule heating to achieve nanoscale temperature mapping for interfacial thermal contact resistance probing between graphene and SiC. Joule heating acted as the heating source, while the Raman spectroscopy probed the temperature rise and difference. A large interfacial thermal resistance was observed. Additional calibration of temperature coefficients of graphene and SiC were conducted from room temperature to 250 °C to determine the temperature variation in experiment. Tang, *et al.* improved Raman thermometry for interface energy coupling measurement by using two separated lasers: one for well-defined localized heating and one for Raman excitation and temperature probing [69, 70]. Naturally corrugated graphene on Si, SiO<sub>2</sub>, and SiC were studied

respectively. Loose contact or point contact between graphene substrate was the main reason for low energy coupling at the interface. In Tang's work, calibration for temperature coefficients of graphene and substrate materials was also carried out to determine the temperature during interface probing.

With the decrease of the size of micro-devices, higher resolution temperature mapping techniques are badly needed. Near-field optics technique makes it possible for scanning delicate nanostructures at a resolution lower than the diffraction limit. Tang's work [71-73] utilized different structures, such as silica nanoparticles and fibers, to focus the excitation laser into an extremely small size and realized a probing resolution of 20 nm in the near-field. In that work, the effect of temperature, stress and optical field on the Raman spectrum was de-conjugated. For the first time, the stress and temperature distribution was characterized successfully with 20 nm resolution. Furthermore, Yue, *et al.* [48] employed an atomic force microscope tip to conduct near field heating and thermal probing at sub-10 nm resolution. The Raman laser acted as both exciting and heating source in Tang's and Yue's works.

To precisely determine the temperature for each layer of a multilayered sample in previous works on interface energy coupling study, additional calibration was needed to build the relation between peak position, linewidth, intensity and temperature. Also the precise knowledge of the amount of absorbed laser energy was needed for calculation of the temperature rise. Besides, other effects induced by temperature rise, like microstage shift, stress build-up in the sample holder due to extended heating, and the resulting out-of-focus effect, would all contribute to large measurement errors. The microstage shift and the out-of-focus effect induced the same

trends of change in peak position, linewidth and intensity as those induced by temperature rise. They were rigorously treated and carefully removed in previous works [73, 74]. The stress effect could be de-conjugated from the difference between changes in linewidth and peak position.

It is critical to develop a method to eliminate the aforementioned disadvantages, but still take advantage of the Raman thermometry's unique features: high spatial resolution and the capability of distinguishing temperatures of materials in immediate contact. The inspiration for novel Raman method comes from the transient electro-thermal (TET) which was developed in our lab for effective thermal characterization of one-dimensional solid materials [75]. The thermal diffusivity of various solid materials has been successfully and precisely determined by this technique [76-78]. In the TET technique, the sample is suspended between two electrodes where a step electrical current is applied. The sample's temperature evolution is obtained by probing its tiny temperature-induced resistance change. This technique is applicable for both electrical conductive and nonconductive materials. For nonconductive samples, a thin layer of metal coating is needed to make the sample electrically conductive and also to give a suitable resistance for Joule heating. The TET technique relies on electric connection and cannot be applied to interface study. Although Raman thermometry has unprecedented selective temperature measurement capacity and a very high spatial resolution, normal Raman technology is not able to probe transient temperature variation to achieve the same capacity of the TET technique.

### 1.3. Scope of present work

Improving and developing new optical based techniques for thermal transport characterization is the main object of this work. The development of the amplitude profile method for the lab-developed PT technique and the corresponding application to inorganic thin films characterization are presented in Chapter 2. To extend the application of the developed PT technique, Chapter 3 investigates the correlation between the internal structures of spider silk films and the overall thermophysical properties. Raman spectroscopy is introduced to further probe structure information as well as the thermal properties. Using Raman spectroscopy to detect the size of Si nanocrystals induced by mechanically cleaving process is demonstrated in Chapter 4. The decrease of the grain sizes of Si nanocrystals accounts for the observed exceptional increasing in Raman intensity. In Chapter 5, the development of time-domain differential Raman is described in details, including the design of the experiment and the construction of appropriate physical models for data analyzing. A good agreement is obtained between the resulting thermal diffusivity for a Si cantilever with the literature value of its bulk counterpart. Chapter 6 includes a summary of my work and a brief introduction of possible future improvement on my present work.

## CHAPTER 2

## PHOTOTHERMAL TECHNIQUE USING AMPLITUDE PROFILE

In this chapter, a lab developed PT technique is improved to employ the amplitude of thermal radiation to determine the thermophysical properties of films in the thickness direction. Amplitude has rarely been used in previous work because of its complexity. The absolute amplitude of thermal radiation is affected by many factors, like the sample's surface reflection, absorption, emissivity, the experimental setup, and the sensitivity of the infrared detector. Instead of its absolute value, the reducing trend of the amplitude of radiation signal against modulation frequencies is used for thermophysical properties determination. The evaluation of the new amplitude method is conducted on SiC films of 2~3  $\mu\text{m}$  thickness on Si. Its accuracy is examined by comparing the results with that of those determined using phase shift fitting, and its sensitivity is also studied in detail.

## 2.1. Physics of the method

To study the thermal transport across a multilayered film sample, the PT technique [19-21] applied a modulated laser beam to the surface of the sample as a heat source, causing thermal radiation from the sample's surface, which contain the information about thermoproperties of the layers beneath the top layer. Given that the thermal diffusion length in gas and the target layer is much smaller than the diameter of the laser beam as the laser focal spot is large enough, the PT experiment can be simplified to one-dimensional cross-plane thermal transport for describing temperature distribution and evolution. The cross-sectional view of the multilayer model is shown in Fig. 2.1a.

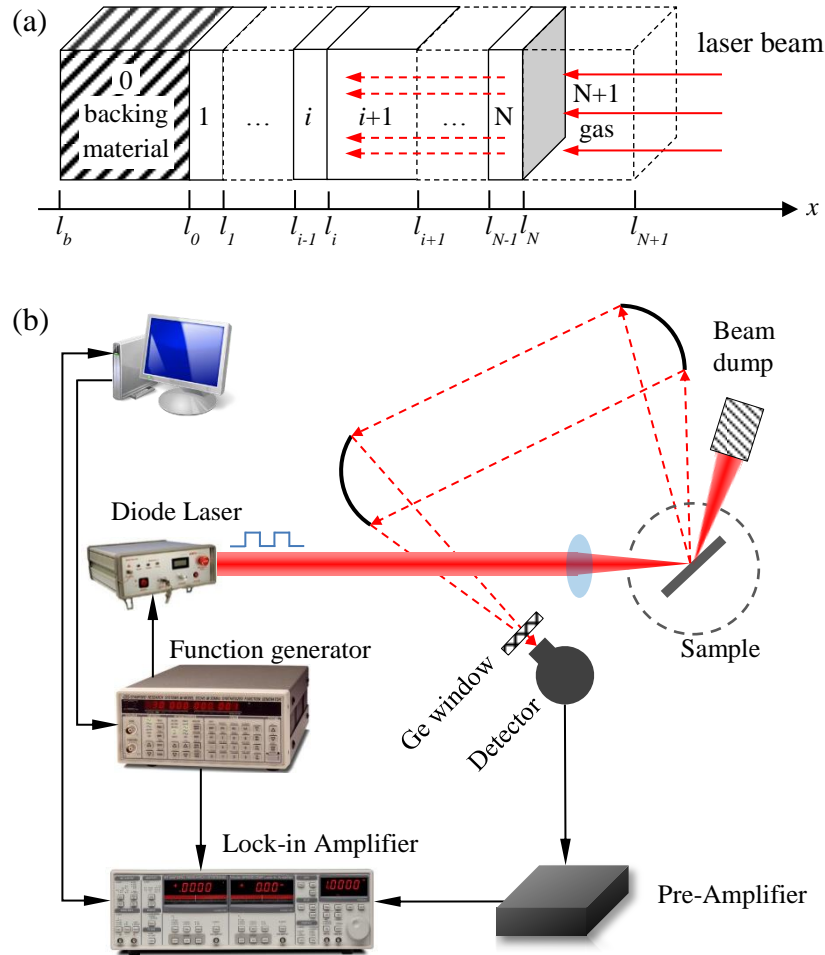


**Figure 2.1.** (a) Schematic of an N-layer sample. It shows the multiple layers model. The  $x$  axis is along the thickness direction of the model. (b) The experimental setup of the PT technique.

Layers from 1 to N are sample layers between the substrate (layer 0) and the gas layer (layer N+1). The incident laser is a square-wave modulated monochromatic laser beam with a modulation frequency  $f$ . Layer  $i$  thereby has a thickness of  $L_i = l_i - l_{i-1}$ . Other thermophysical properties of the layer  $i$  are noted as: thermal conductivity  $k_i$ , specific heat  $c_{p,i}$ , thermal diffusivity  $\alpha_i$ , and optical absorption coefficient  $\beta_i$ . Other parameters needed in the physical model are the thermal diffusion length  $\mu_i = \sqrt{\alpha_i / \pi f}$ , thermal diffusion coefficient  $a_i = 1 / \mu_i$ , and thermal

contact resistance between layer  $i$  and  $(i+1)$ ,  $R_{i,i+1}$ . Therefore, the governing equation for a multilayer 1D thermal diffusion problem in layer  $i$  can be expressed as

$$\frac{\partial^2 \theta_i}{\partial x^2} = \frac{1}{\alpha_i} \frac{\partial \theta_i}{\partial t} - \frac{\beta_i I_0}{2k_i} \exp\left(\sum_{m=i+1}^N -\beta_m L_m\right) \times e^{\beta_i(x-l_i)} (1 + e^{j\omega t}) \quad (2.1)$$

where  $\theta_i = T_i - T_{amb}$  is the modified temperature of layer  $i$ , and  $T_{amb}$  is the ambient temperature.  $\omega$  is angular frequency ( $2\pi f$ ). The solution  $\theta_i$  to Eq. 2.1 is composed of the transient component  $\theta_{i,t}$ , the steady DC component  $\bar{\theta}_{i,s}$  and the steady AC component  $\theta_{i,s}$ . Among the previous three terms, only the AC component  $\theta_{i,s}$  will be collected for further evaluation and data processing.

The general solution of  $\theta_{i,s}$  can be expressed as following equation:

$$\theta_{i,s} = [A_i e^{\sigma_i(x-l_i)} + B_i e^{-\sigma_i(x-l_i)} - E_i e^{\beta_i(x-l_i)}] e^{j\omega t} \quad (2.2)$$

where  $E_i = G_i / (\beta_i^2 - \sigma_i^2)$  with  $G_i = \frac{\beta_i I_0}{2k_i} \exp(-\sum_{m=i+1}^N \beta_m L_m)$ , and for  $i < N$ ,  $G_N = \beta_N I_0 / 2k_N$ , and  $G_{N+1} = 0$ .  $\sigma_i$  is defined as  $(1 + j) a_i$  with  $j = \sqrt{-1}$ .

To obtain coefficients  $A_i$  and  $B_i$ , both the gas layer and backing material are assumed to be thermally thick (sufficiently met in the experiment), so that  $A_{N+1} = 0$  and  $B_0 = 0$ . The rest of coefficients are determined by using the interfacial conditions at  $x = l_i$ , as

$$\begin{bmatrix} A_i \\ B_i \end{bmatrix} = U_i \begin{bmatrix} A_{i+1} \\ B_{i+1} \end{bmatrix} + V_i \begin{bmatrix} E_i \\ E_{i+1} \end{bmatrix} \quad (2.3)$$

where  $U_i$  is the interfacial transmission matrix of heat and  $V_i$  is the absorption matrix of light from layer  $i+1$  to  $i$ . [79] They are expressed as

$$U_i = \frac{1}{2} \begin{bmatrix} u_{11,i} & u_{12,i} \\ u_{21,i} & u_{22,i} \end{bmatrix}; \quad V_i = \frac{1}{2} \begin{bmatrix} v_{11,i} & v_{12,i} \\ v_{21,i} & v_{22,i} \end{bmatrix}, \quad (2.4)$$

$$\text{where } u_{1n,i} = (1 \pm k_{i+1}\sigma_{i+1} / k_i\sigma_i \mp k_{i+1}\sigma_{i+1}R_{i,i+1}) \times \exp[\mp\sigma_{i+1}(l_{i+1} - l_i)], \quad n = 1, 2, \quad (2.4a)$$

$$u_{2n,i} = (1 \mp k_{i+1}\sigma_{i+1} / k_i\sigma_i \mp k_{i+1}\sigma_{i+1}R_{i,i+1}) \times \exp[\mp\sigma_{i+1}(l_{i+1} - l_i)], \quad n = 1, 2, \quad (2.4b)$$

$$v_{n1,i} = 1 \mp \beta_i / \sigma_i, \quad n = 1, 2, \quad (2.4c)$$

$$\text{and } v_{2n,i} = (-1 \mp k_{i+1}\beta_{i+1} / k_i\sigma_i \mp k_{i+1}\beta_{i+1}R_{i,i+1}) \times \exp[-\beta_{i+1}(l_{i+1} - l_i)], \quad n = 1, 2. \quad (2.4d)$$

Thus, the coefficients  $A_i$  and  $B_i$  are obtained using

$$B_{N+1} = - \frac{[0 \quad 1] \sum_{m=0}^N (\prod_{i=0}^{m-1} U_i) V_m \begin{bmatrix} E_m \\ E_{m+1} \end{bmatrix}}{[0 \quad 1] (\prod_{i=0}^{m-1} U_i) \begin{bmatrix} 0 \\ 1 \end{bmatrix}} \quad (2.5a)$$

$$\begin{bmatrix} A_i \\ B_i \end{bmatrix} = (\prod_{m=i}^N U_m) \begin{bmatrix} 0 \\ B_{N+1} \end{bmatrix} + \sum_{m=i}^N (\prod_{k=i}^{m-1} U_k) V_m \begin{bmatrix} E_m \\ E_{m+1} \end{bmatrix} \quad (2.5b)$$

The PT signal can be expressed in terms of surface temperature  $T$  of the top layer, since the measured radiation variation is proportional to the surface temperature change. Detailed calculations are provided in the reference [18]. These equations are listed here for further discussion of physical meanings and sensitivity in our amplitude method.

In previous studies with the PT technique, the amplitude data was not used to determine a film's properties due to the fact that the absolute amplitude (raw data,  $A_{raw}$ ) is affected by many factors other than the rise in temperature, such as the experimental setup (optical alignment), the sample's surface properties, and the sensitivity of the infrared detector. An amplitude normalizing procedure is thus introduced to process  $A_{raw}$  before it is used for fitting.

The measured radiation signals are directly affected by the amplitude variations of the incident laser amplitude variation due to the inevitable systematic uncertainty and energy loss produced. Thus calibration data from a metal coated substrate with a large thermal conductivity is required before the PT measurement to exclude the random oscillation in the amplitude of the incident laser. With the reflected laser amplitude ( $A_{cal}$ ) from this metallic surface, the laser output variation effect can be eliminated by dividing  $A_{raw}$  by  $A_{cal}$ . Meanwhile, the sample's surface properties should also be considered, like surface emissivity and absorptivity. The influence of other parameters can be grouped in a universal constant during data fitting discussed later.

Additionally, the frequency  $f$  also affects the raw amplitude by modulating the incident laser during the entire PT experiment. The measured amplitude decreases quickly as the frequency increases since the heating time is shorter in each period as the frequency becomes higher. The sensitivity is also lower in the higher frequency range, so the modulation effect should be taken into consideration. The total energy input depends on the irradiation time and the incident intensity. For physical analysis, when the modulated laser irradiates the metallic film, the total incident energy arriving at the sample surface ( $\Delta E$ ) in one heating period is  $\Delta E = 0.5\varepsilon I_0 / f$ , where  $I_0$  is the laser intensity, and  $\varepsilon$  the surface absorptivity.  $I_0$  is proportional to the reflected laser amplitude  $A_{cal}$ . The modulation frequency in the denominator illustrates that the longer the laser irradiates ( $1/f$ ), the higher the temperature rises on the metallic surface. Another involved parameter, the thermal diffusion length  $\mu = \sqrt{\alpha/\pi f}$ , depends on both the thermal diffusivity  $\alpha$  and the frequency  $f$ . A higher frequency will shorten the diffusion length and concentrate the absorbed energy into a smaller depth. Amplitude  $A_{raw}$  is the combination of these two factors as

$$\frac{A_{raw}}{A_{cal}} \sim \frac{\zeta / f}{\sqrt{\alpha / f} \cdot \rho c_p} = \frac{1}{\sqrt{f}} \cdot \frac{\zeta}{\sqrt{k \rho c_p}}, \quad (2.6)$$

where  $\zeta$  is a coefficient related to  $\varepsilon$  and other factors in the experiment, including detector sensitivity, surface emissivity, and collection angle of the paraboloidal mirrors.  $\zeta$  is recognized as a constant across all the frequencies, so  $f$  is the only changing variable in Eq. 2.6. The resulted  $A_{raw}/A_{cal}$  is further normalized by multiplying  $\sqrt{f}$  to get rid of the frequency effect. The normalized amplitude  $A_{nor}$ , can be expressed as

$$A_{nor} = \frac{A_{raw} \cdot \sqrt{f}}{A_{cal}} \sim \frac{\zeta}{\sqrt{k \rho c_p}} = \frac{\zeta}{e} \quad (2.7)$$

where  $e$  is the effusivity of the sample with the expression  $e = \sqrt{k \rho c_p}$ . The physical meaning of thermal effusivity is the thermal energy needed for 1 K temperature rise in the characteristic thermal diffusion length per unit area per second. Equation 2.7 shows that  $A_{nor}$  is inversely proportional to  $e$  of the sample, including the sample layer and the substrate.

After the amplitude normalization, the fitting program is run to fit the trend of the normalized amplitude against frequency. With the guessed initial thermal conductivity and specific heat of the layer of interest, the program starts calculating the theoretical amplitude at each experimental frequency and compares the resulted curve with the  $A_{nor}$  curve using the least square method. During the fitting process, a universal constant  $C$  is introduced to group all the aforementioned constant parameters, and then the normalized theoretical amplitude  $A_{nor,the}$  is multiplied by  $C$  and compared with the normalized experiment amplitude  $A_{nor,exp}$  at each frequency,  $(A_{nor,exp} - C A_{nor,the})_f$ . Theoretically, the best fitted values can be obtained when the sum of the square of  $[(A_{nor,exp} - C A_{nor,the})_f]$  over all the frequencies is the minimum value. Thus,

the derivative should be 0 and  $C$  can be determined using  $\sum_f A_{nor,exp,i} A_{nor,the,i} / \sum_f A_{nor,the,i}^2$ . The thermal conductivity and specific heat will be adjusted around the initial guessed values until finding the best theoretical curve that fits the shape of the experimental curve. The corresponding thermal conductivity and specific heat are taken as the properties of the layer of interest.

## 2.2. Across-plane thermal characterization of SiC and SiO<sub>2</sub> films on Si

### 2.2.1. Sample and experiment details

We first measure SiC films grown on Si to demonstrate the capacity of the amplitude method and compare the results with the phase shift method which has been used and verified extensively in the past [19-21]. The chemical vapor deposited (CVD) SiC samples on the Si substrate are from Veeco with a size of 1”x1”. Two different ratios of Si and C are used in their film growth: 50% Si / 50% C for sample 1 and 2, and 20% Si / 80% C for sample 3. An 80 nm-thick Cr film is sputter-coated on the top of the SiC layer to absorb the laser energy and generate heat in the experiment. The very fine thickness (80 nm) of the Cr coating has very little effect on the measurement result.

Both the principle and the experimental setup of the PT technique are shown in Fig. 2.1b. A continuous infrared diode laser (809 nm) is modulated by a function generator and focused on the sample surface with a convex lens. The metallic layer on top of the sample absorbs the periodic energy from the modulated laser and generates heat as a heating source. A periodic temperature variation on the surface arises which causes a variation in the thermal emission from the sample surface. The thermal emission is collected by two off-axis paraboloidal mirrors and then collected and identified by an infrared detector (J15D12-M204-S01M-60, Jusdon

Technologies). In front of the detector, a Ge window filters out the reflected laser beam from the sample and only allows the thermal radiation to pass. The thermal radiation will be converted into electrical signals, pre-amplified and then sent to a lock-in amplifier. The whole experiment is controlled by a program for automatic data acquisition and noise suppression. The experimental frequency range in this work is 400 Hz to 20 kHz.

### 2.2.2. The phase shift method

To evaluate the accuracy of the amplitude method, the phase shift method is conducted first to determine the sample's thermal conductivity and interfacial resistance for comparison. In our fitting, the properties of the air layer, the metal coating, the sample layer, and the substrate are taken from references [80]: The 80 nm thick Cr film has a thermal conductivity  $k$  of 93.7 W/m·K, a specific heat  $c_p$  of 449 J/kg·K, and density  $\rho$  of 7160 kg/m<sup>3</sup>. The Si substrate has a thermal conductivity  $k$  of 148 W/m·K, the specific heat  $c_p$  of 712 J/kg·K, and the density  $\rho$  of 2330 kg/m<sup>3</sup>. The bulk density and specific heat of SiC, 690 J/kg·K and 3160 kg/m<sup>3</sup>, are used here because these two properties for the CVD SiC are weakly determined by the structure. They should have little deviation from the bulk's values.

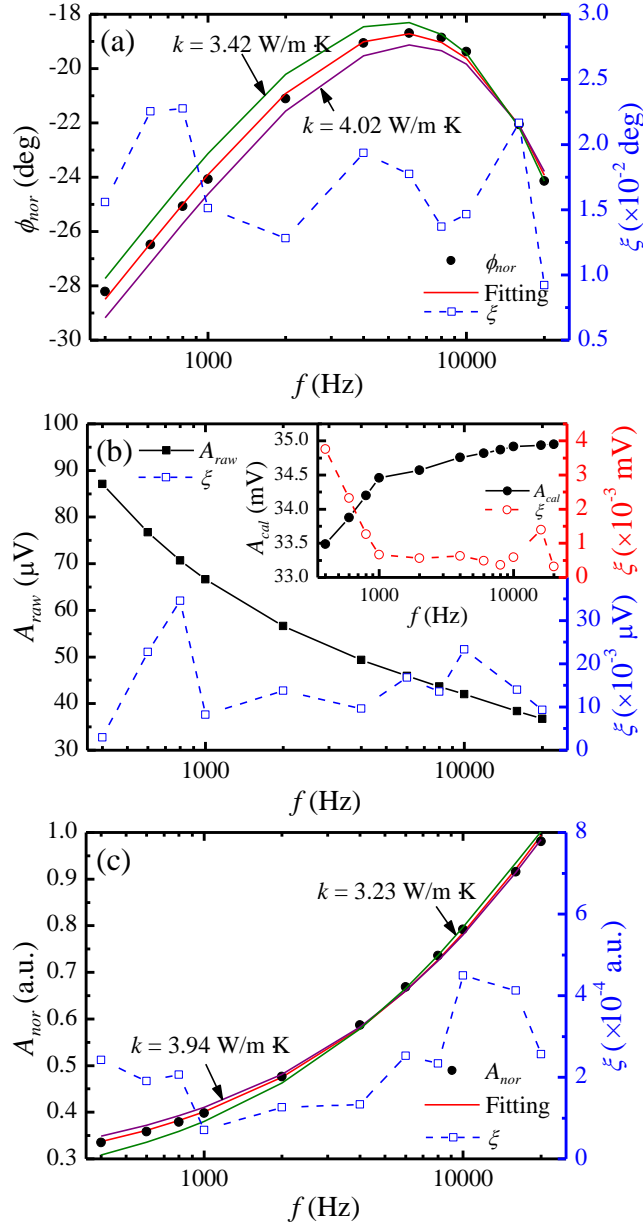


**Figure 2.2.** (a) The fitting result based on the phase shift method for the 2.5  $\mu\text{m}$  SiC film on Si. The thermal conductivity is determined at 3.72 W/m K. The statistical uncertainty  $\xi$  is much smaller than  $\phi_{nor}$ , indicating the accuracy of the measurement. Curves with thermal conductivities of 3.42 W/m K and 4.02 W/m K demonstrate the fitting uncertainty. (b) The raw data of samples and the calibration amplitude (inset plot). (c) The fitting result based on the amplitude method. The normalized amplitude  $A_{nor}$  (black dots) increases against the frequency  $f$ . The thermal conductivity is determined at 3.58 W/m K.

The fitted result for sample 1 using the phase shift method is plotted in Fig. 2.2a. Sound agreement is observed between the fitting result and the experimental data. The thermal conductivity is fitted as 3.72 W/m·K and the thermal contact resistance  $R_{Si,SiC}''$  is determined to be  $1.5 \times 10^{-7} \text{ m}^2 \cdot \text{K}/\text{W}$ . The experimental statistical uncertainty (the blue hollow squares in Fig. 2.2a) is calculated using  $\sqrt{\xi_{\phi_{raw}}^2 + \xi_{\phi_{cal}}^2}$ , where  $\xi_{\phi_{raw}}$  and  $\xi_{\phi_{cal}}$  are statistical uncertainty of the phase shift for the raw data and calibration data, respectively. Both  $\xi_{\phi_{raw}}$  and  $\xi_{\phi_{cal}}$  are acquired during the PT measurement and calibration. For the fitting uncertainty of thermal conductivity, the theoretical curves with  $k$  of 3.42 W/m·K and 4.02 W/m·K ( $\pm 8\%$  deviation from best fitted  $k$ ) show obvious deviation from the best fitting result. In fact, the deviation is much larger than the experimental uncertainty of the phase shift. We can therefore conclude the fitting uncertainty of the thermal conductivity is  $\pm 8\%$ .

### 2.2.3. The amplitude method

For the amplitude method, the raw amplitude of radiation signal  $A_{raw}$  and the reflected laser intensity (the calibration amplitude)  $A_{cal}$  for sample 1 are shown in Fig. 2.2b. The statistical uncertainty  $\xi_{A_{raw}}$  is collected while the raw amplitude is being recorded during the measurement.  $A_{raw}$  decreases quickly as the frequency increases. For all samples, the raw amplitude has a very similar trend so that the differences in heat transfer for different samples are difficult to distinguish from the raw amplitude. This significantly illustrates the fact that the effect of  $f$  lowers the sensitivity of  $A_{raw}$ . By multiplying  $A_{raw}$  by  $\sqrt{f}$  in the normalization, we easily extract the difference in heat transfer for each sample over the entire frequency range and thereby fit the variation of the amplitude and obtain its thermophysical properties. The reflected intensity of the

laser  $A_{cal}$  (black dots in the inset plot of Fig. 2.2b) is very steady with only 4.8% variation across the whole measurement. Although it is affected by the modulation frequency to a very limited extent, the tiny change of the irradiation laser is considered in our amplitude fitting as described above. Its statistical uncertainty  $\xi_{A_{cal}}$  in the inset plot is much lower, about 0.1% of  $A_{cal}$ , indicating the sound steadiness of the laser source.

After excluding influences from the systematic noise, experimental setup and frequency, the final normalized amplitude  $A_{nor}$  (black dots in Fig. 2.2c) for sample 1 gradually increase relative to the frequency from 0.3 to 1.  $A_{nor}$  at a higher frequency becomes more significant for the shape determination of the  $A_{nor}$  curve and thereby the  $k$  fitting. Opposite to the raw data,  $A_{nor}$  becomes more sensitive. Its small variation can be easily detected especially in the high frequency range due to the fact that the modulation effect is removed. With the same parameters used in the phase shift method, a thermal conductivity  $k$  of 3.58 W/m K is obtained based on the amplitude method. Also the curves with  $k = 3.23$  W/m·K and  $k = 3.94$  W/m·K clearly show  $\pm 10\%$  deviation of the thermal conductivity. On the other side, the experimental statistical

uncertainty  $\xi_{A_{nor}}$  is calculated using  $|A_{nor}| \times \sqrt{\left(\frac{\xi_{A_{raw}}}{A_{raw}}\right)^2 + \left(\frac{\xi_{A_{cal}}}{A_{cal}}\right)^2}$ . Its value is about five orders of magnitude less than  $A_{nor}$  which is much smaller than  $\pm 10\%$ . Therefore, the fitting uncertainty of the thermal conductivity for the amplitude method is determined to be  $\pm 10\%$ .

The fitted thermal conductivity for all SiC/Si samples with both the phase shift and amplitude methods are listed in the Table 2.1. The amplitude method gives very close fitting results of thermal conductivity to the phase shift method. The deviations between these two

methods are 4%, 7%, and 16% for samples 1, 2, and 3, respectively. However, the thermal contact resistance is hard to be precisely determined by the amplitude method. We find the fitting result is not sensitive to the interface thermal resistance.  $R''_{\text{Si,SiC}} = 1.5 \times 10^{-7} \text{ m}^2 \cdot \text{K/W}$  and  $R''_{\text{Si,SiC}} = 0 \text{ m}^2 \cdot \text{K/W}$  give undistinguishable fitting curves when other parameters are fixed. More detailed studies are given in the next section.

**Table 2.1.** Thermal conductivity determination based on phase shift and amplitude.

Sample	Description	Thickness	Thermal conductivity $k$ (W/m K)		$R''_{\text{Si,SiC}}$ ( $\text{m}^2 \cdot \text{K/W}$ )
			Phase shift	Amplitude	Phase shift
1	Si <sub>50</sub> C <sub>50</sub>	2.5 $\mu\text{m}$	3.72	3.58	$1.5 \times 10^{-7}$
2	Si <sub>50</sub> C <sub>50</sub>	2.5 $\mu\text{m}$	3.86	3.59	$1.1 \times 10^{-7}$
3	Si <sub>20</sub> C <sub>80</sub>	3.5 $\mu\text{m}$	2.21	2.59	$1.5 \times 10^{-7}$
4	SiO <sub>2</sub>	500 nm	1.31	1.68	$< 10^{-8}$

#### 2.2.4. Raman characterization

Compared with the results from the phase shift method, the amplitude method excellently determines the thermal conductivity of the SiC film. However, it is noticed that the thermal conductivity of the SiC films reported in Table 2.1 is obviously lower than that of bulk SiC: from 360 W/m K to higher [81]. This significant reduction in thermal conductivity is mainly attributed to structures of CVD SiC. To characterize the internal structure of those films, a confocal Raman spectrometer (Voyage, B&W Tek, Inc.) installed with a 532 nm excitation laser and a microscope (BX51, Olympus) are used for structure characterization. The Raman laser beam is focused using a 50 $\times$  microscope objective, with a focal point size of about 8  $\mu\text{m}^2$ . The resolution of this Raman spectrum is 1.05-1.99  $\text{cm}^{-1}$ . All samples are characterized and spectra are all recorded at room temperature (20 °C) in the open air.

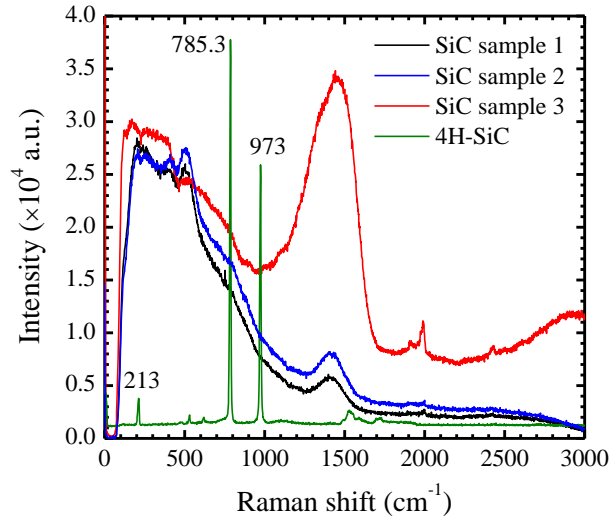


**Figure 2.3.** Raman spectra of the SiC samples and bulk 4H-SiC single crystal under the same measurement condition. The bulk SiC single crystal shows clear sharp peaks indicating good crystalline structures, while the CVD SiC samples only have broad peaks demonstrating their amorphous structures.

The clear differences between samples 1, 2, 3, and the crystal 4H-SiC are shown in the Raman spectra in Fig. 2.3. For the 4H-SiC crystal, its Raman spectrum has several sharp peaks at  $212\text{ cm}^{-1}$  (FTA mode for 4H polytype),  $785\text{ cm}^{-1}$  (TO band) and  $973\text{ cm}^{-1}$  (LO band) [82, 83]. But, for the CVD SiC films, only several broad peaks are observed. Samples 1 and 2 have the same composition of Si and C in the SiC film, so their Raman spectra are almost the same and have a small broad peak at  $1410\text{ cm}^{-1}$ . Due to the different ratio of Si and C from sample 1 and 2, sample 3 shows a slightly different spectrum. It also has the broad  $1410\text{ cm}^{-1}$  peak, but the peak is much stronger than that of samples 1 and 2. The  $1410\text{ cm}^{-1}$  is associated to stretching vibration mode of the C-C bond [84], which indicates the formation of carbon clusters in all three CVD SiC films. Sample 3 has more percent of C than sample 1 and 2. A large amount of C may form homonuclear C-C bond in the carbon clusters instead of forming Si-C bonds. The weak peak around  $500\text{ cm}^{-1}$  indicates some silicon clusters in the films. According to the Raman spectra, the crystal SiC has several sharp peaks showing high crystallinity, while the CVD samples have only

a broad and weak peak around  $700\text{ cm}^{-1}$  for Si-C bond (shown as a shoulder in Fig. 2.3) indicating the small grain size of SiC crystals within the film and other amorphous structures.

Since the single crystalline 4H-SiC is a long range ordered crystal, its optical phonons are largely restricted to one scattering mode and produce a narrow peak. However, the nanocrystalline SiC optically allows more phonon scattering modes to broaden peaks due to its smaller grain size [74]. The SiC films measured here are grown on a Si substrate. Lattice mismatch at the SiC/Si interface will occur at the beginning of growth, leading to significantly reduced crystallinity of the film. Additionally, if the growth is not epitaxial, nanograins will exist in the film. Such small size grains will significantly enhance phonon scattering mainly at the grain boundary, and broaden the Raman peak. The grain boundaries induced phonon scattering changes the wavelength and wavenumber of the phonon. As a result, a substantially reduced thermal conductivity is expected. Moreover, sample 3 contains more carbon clusters than sample 1 and 2 due to the strong  $1410\text{ cm}^{-1}$  peak in its Raman spectrum. The low thermal conductivity of amorphous structures in carbon clusters further lowers the overall thermal conductivity of sample 3.

### **2.2.5. Thermal transport across 500 nm thick SiO<sub>2</sub> film**

For the purpose of comparison and studying the accuracy of the amplitude method, we also measure another non-crystalline sample (Sample 4) that is composed of a thin layer of SiO<sub>2</sub> on a Si substrate. The SiO<sub>2</sub> layer is grown via thermal oxidation and has a thickness of 500 nm. A 60 nm Ir coating covers the top of SiO<sub>2</sub> layer and performs the same function as the Cr film for SiC samples. The Ir coating has a thermal conductivity of  $147\text{ W/m}\cdot\text{K}$ , density of  $2.26\times 10^4$

kg/m<sup>3</sup>, and specific heat of 131 J/kg·K. For the SiO<sub>2</sub> film, density (2200 kg/m<sup>3</sup>) and specific heat (745 J/kg·K) of bulk SiO<sub>2</sub> are used here for the 500 nm thermal oxidation layer during data processing.

The fitted curves for both the phase shift and amplitude methods are plotted in Fig. 2.4 and fitted thermal conductivities are listed in Table 2.1. The best fitted thermal conductivity of SiO<sub>2</sub> is 1.31 W/m K based on the phase shift method. The corresponding interfacial thermal resistance is less than 10<sup>-8</sup> m<sup>2</sup>·K/W, which is too small to be precisely determined. The  $k$  from the phase shift method is very close to the reference bulk's value (1.38 W/m K). For the amplitude fitting method,  $k$  of SiO<sub>2</sub> is determined to be 1.68±0.17 W/m K and  $R''_{\text{Si/SiO}_2}$  is also less than 10<sup>-8</sup> m<sup>2</sup>·K/W. This  $k$  is 24% higher than that from the phase shift method or the value in literature. The thin thickness of SiO<sub>2</sub> is one reason that causes this deviation and raises large uncertainty. Usually when the film is very thin, its own thermal resistance  $L/k$  (thermal resistance per unit area) is very small. For the SiO<sub>2</sub> layer (500 nm),  $L/k$  is about 3.8×10<sup>-7</sup> m<sup>2</sup>·K/W, which will produce a weaker effect on the phase shift and amplitude than the thick SiC films (2.5 μm). In the experiment, the small variation in normalized amplitude will lower the sensitivity of  $k$  in the fitting process. As shown in Fig. 2.4, the percentage of the increment of  $A_{nor}$  in the SiO<sub>2</sub>/Si sample is smaller than that in the SiC/Si sample. More thermal energy penetrates into the substrate and the effusivity of Si strongly affects the amplitude of thermal radiation which is detailed in the next section. If a pure bulk sample is measured by using the amplitude method, the normalized amplitude variation would be 0 (flat  $A_{nor}$  against frequency).

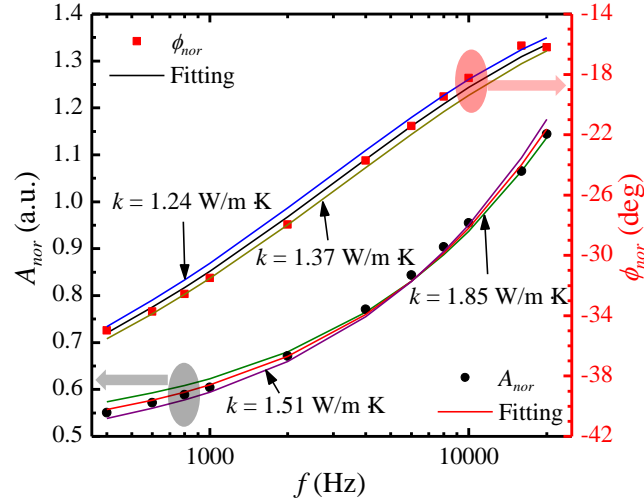


**Figure 2.4.** Fitting results based on the phase shift and the amplitude methods for the 500 nm thick SiO<sub>2</sub> film on Si. With the phase shift method, the thermal conductivity is determined to be 1.31 W/m·K. Theoretical curves with thermal conductivities of 1.24 W/m·K and 1.37 W/m·K demonstrate the fitting uncertainty. Based on the amplitude method, the thermal conductivity is determined to be 1.68 W/m·K. The fitting uncertainty is illustrated with curves of thermal conductivities of 1.51 W/m·K and 1.85 W/m·K.

### 2.3. Sensitivity study of parameters

#### 2.3.1. Sensitivity study of thermal contact resistance

As mentioned above, the interfacial thermal resistance cannot be precisely determined in the amplitude method even though it is very sensitive to the film's thermal conductivity. In the theoretical calculation, the role of the interface resistance is illustrated in Eq. 2.4a. The term  $k_{i+1}\sigma_{i+1}/k_i\sigma_i$  can be simplified to  $e_{i+1}/e_i$ , where  $e_i$  is the effusivity of the layer  $i$ . It is the ratio of effusivity  $e$  between the sample layer and the substrate in a two-layered sample. In our case study, the interaction between SiC layer and Si substrate dominates the thermal transport through the whole sample. Therefore, the term  $k_{i+1}\sigma_{i+1}/k_i\sigma_i$  can be expressed as  $e_{\text{SiC}}/e_{\text{Si}}$ , which is the effusivity ratio of SiC layer to Si substrate. This ratio is usually smaller than 1 depending on how the sample is designed and is calculated to be around 0.18 with the fitting result for our samples.

$k_{i+1}\sigma_{i+1}R_{i,i+1}$  is the only term relevant to the interfacial thermal contact resistance in the theoretical calculation. It can be deduced as  $(1+j)\sqrt{\pi f} \cdot e_{i+1} \cdot R_{i,i+1}$ , in which  $f$  is the only variable in the PT measurement.  $R_{i,i+1}$  is  $R''_{\text{Si,SiC}}$  in the present work. Clearly, the effect of  $R_{i,i+1}$  is mainly dependent upon the frequency. Furthermore, the SiC is grown on the Si surface using a CVD method, thus the connection between these two layers should be good. A small  $R_{i,i+1}$  is expected, around  $10^{-7} \text{ m}^2 \cdot \text{K/W}$  according to our fitting result. At a very high frequency, the resistance effect becomes more important and contributes to the total value of Eq. 2.4a. For example, the value of this term reaches  $10^{-2}$  at 10 kHz. Compared with the terms “1” and  $k_{i+1}\sigma_{i+1} / k_i\sigma_i$ ,  $(1+j)\sqrt{\pi f} \cdot e_{i+1} \cdot R_{i,i+1}$  is still much smaller, especially in the low frequency range in Eq. 2.4a. However, in the phase shift method, the phase shift changes more relative to the amplitude with the same variation of  $R_{i,i+1}$ . Therefore, the phase shift method is more sensitive to the interfacial resistance. For the exponent term  $\exp[\mp\sigma_{i+1}(l_{i+1} - l_i)]$ , its value is determined by the thickness of the sample layer. Samples measured by the PT technique in our case have a thickness of several micrometers or fewer, so the value of this term is approximately equal to 1.

A study of  $R''_{\text{Si,SiC}}$  is conducted for sample 1 to reveal the sensitivity of the thermal contact resistance in the amplitude method. The residual ( $r$ ) of the least square calculation determines the quality of the resulting curve in the fitting process. It is defined as the standard deviation of  $(A_{nor,exp} - C A_{nor,the})$  at all recorded frequencies. The relationship between  $r$  and the thermal resistance  $R''_{\text{Si,SiC}}$  is plotted in Fig. 2.5a. The residual  $r$  clearly begins to increase when  $R''_{\text{Si,SiC}}$  is larger than  $10^{-7} \text{ m}^2 \cdot \text{K/W}$ . It should be noted that the interface between the CVD SiC film and the

Si substrate has a good contact so that  $R''_{\text{Si,SiC}}$  should not be larger than  $10^{-6} \text{ m}^2 \cdot \text{K/W}$ . Thus, the thermal contact resistance is not sensitive in our case.

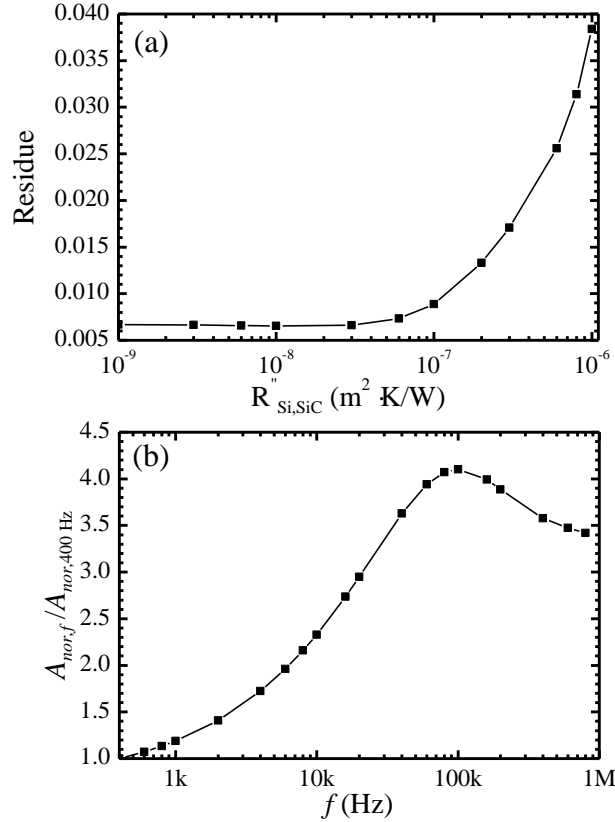


**Figure 2.5.** (a) Residual of the least square method against the thermal contact resistance  $R''_{\text{Si,SiC}}$  for sample 1. The residual does not change much against  $R''_{\text{Si,SiC}}$  until it is larger than  $10^{-7} \text{ m}^2 \cdot \text{K/W}$ , so the amplitude method is not sensitive to  $R''_{\text{Si,SiC}}$ . (b) The ratio  $A_{\text{nor},f} / A_{\text{nor},400 \text{ Hz}}$  against the frequency with all parameters from sample 1. The rest parameters for sample 1 are fixed for these two plots:  $k$  is  $3.58 \text{ W/m K}$ ,  $\rho$  is  $3160 \text{ kg/m}^3$ ,  $c_p$  is  $690 \text{ J/kg K}$ , and  $d$  is  $2.5 \text{ }\mu\text{m}$ , and  $R''_{\text{Si,SiC}}$  is  $1.51 \times 10^{-7} \text{ m}^2 \text{ K/W}$  for Fig. 2.4b.

### 2.3.2. Importance of effusivity

From the physical model described in Sec. 2.1, the interfacial transmission matrix of heat and then  $k_i \sigma_i$  and  $\sigma_i L_i$  in Eq. 2.4a for each layer in the sample are obtained directly and independently. Thus, in the fitting process,  $k \rho c_p$  (thermal effusivity) and  $L/k$  (thermal resistance

per unit area) can be determined with high accuracy and will not be affected by the uncertainty of thickness measurement. Individual thermal parameter,  $k$  and  $\rho c_p$ , needs further calculation which will give rise to their experimental uncertainty. Alternatively, the thermal effusivity is an important and reliable parameter for evaluating the amplitude method.

In the amplitude method, the normalized amplitude  $A_{nor}$  directly shows the effect of thermal diffusion length changing against an increasing frequency. The thermal diffusion length is proportional to  $1/\sqrt{f}$ . At a low modulated frequency, the thermal diffusion length is long and may be longer than the thickness of the sample layer. The thermal radiation signal in this situation will be affected by the thermophysical properties of both the sample layer and the substrate. As the thermal diffusion length decreases at a high frequency, the sample layer's property contributes primarily to the radiation signal. Based on this analysis, a simple assessment of the accuracy of the amplitude method can be thereby conducted directly from  $A_{nor}$ .

The ratio  $A_{nor,f}/A_{nor,400 \text{ Hz}}$  is introduced to study the accuracy of the amplitude normalization and the amplitude method. This relationship between  $A_{nor,f}/A_{nor,400 \text{ Hz}}$  and the frequency is shown in Fig. 2.5b with determined parameters from sample 1: density  $\rho = 3160 \text{ kg/m}^3$ , thermal conductivity  $k = 3.58 \text{ W/m K}$ , specific heat  $c_p = 690 \text{ J/kg K}$ , and the thickness of the film  $L = 2.5 \text{ }\mu\text{m}$ . The calculation of the curve starts at 400 Hz to guarantee the assumption of the 1D model. Also, 400 Hz is the same as the start frequency in the experiment. The frequency ends at 0.9 MHz in assessment, which is much larger than 20 kHz in the experiment. The theoretical calculation to this high frequency is for exploring the effect of the Cr layer on the thermal radiation signals, though such high frequency is unnecessary in the experiment. Figure

2.5b shows a gradual increase for the curve against the modulated frequency when the frequency is lower than 100 kHz. After rising to a maximum of 100 kHz, the amplitude ratio begins to decrease.

According to the expression of thermal diffusion length  $\mu_i = \sqrt{\alpha_i / \pi f}$ , the diffusion depth is longer at low frequencies.  $\mu_{\text{SiC},400 \text{ Hz}}$  is approximately 36  $\mu\text{m}$  at 400 Hz which is longer than the thickness of the SiC film (2.5  $\mu\text{m}$ ). The thermal energy can pass through the SiC film and significantly penetrating into the Si substrate. The effusivity of Si dominates the effective effusivity of the sample. When the frequency rises to 100 kHz,  $\mu_{\text{SiC},100 \text{ kHz}}$  becomes 2.29  $\mu\text{m}$ . The thermal energy is only transferred inside the SiC film and the radiation signal is mainly related to the SiC properties. The data point at 100 kHz in Fig. 2.5b is selected for further discussion. The theoretical fitted value of the ratio  $A_{\text{nor},100 \text{ kHz}} / A_{\text{nor},400 \text{ Hz}}$  is 4.10 in the experiment. In contrast, it has  $A_{\text{nor},100 \text{ kHz}} / A_{\text{nor},400 \text{ Hz}} \approx \sqrt{(k\rho c_p)_{\text{Si}} / (k\rho c_p)_{\text{SiC}}} = 5.60$  based on Eq. 2.7, which is slightly larger than the theoretical fitted ratio.  $A_{\text{nor},400 \text{ Hz}}$  is a combined result of both SiC and Si effects at the low frequency of 400 Hz because both SiC and Si contribute portions of the amplitude of the total thermal radiation from the Cr surface. Since  $e_{\text{SiC}}$  ( $2.85 \times 10^3 \text{ W/m}^2 \text{ K s}^{0.5}$ ) is smaller than  $e_{\text{Si}}$  ( $1.57 \times 10^4 \text{ W/m}^2 \text{ K s}^{0.5}$ ), this combination lowers  $\sqrt{(k\rho c_p)}$  at 400 Hz. The effect of Cr is negligible at 400 Hz.

At the frequency of 100 kHz, the thermal diffusion length in SiC becomes shorter (2.29  $\mu\text{m}$ ) than the SiC film's thickness, and thus the effect of the Si substrate on the thermal radiation becomes negligible. Instead, the Cr film plays an more important role in determining the

effective effusivity. Since the effusivity of Cr ( $1.74 \times 10^4 \text{ W/m}^2 \text{ K s}^{0.5}$ ) is much higher than that of SiC ( $2.85 \times 10^3 \text{ W/m}^2 \text{ K s}^{0.5}$ ),  $e_{\text{Cr}}$  increases  $e_{\text{eff}}$  that determines the thermal radiation signal. Both of these two factors cause the deviation in the amplitude ratio between our theoretical fitting and the real effusivity. When the frequency is higher than 100 kHz, the normalized amplitude ratio gradually decays compared with the ratio at 100 kHz in Fig. 2.5b. The reduction results from the increasing effect of the Cr film. At frequencies higher than 100 kHz, the SiC's thermophysical property contributes less to the thermal radiation because the thermal diffusion length in the SiC film continues decreasing. The effective effusivity to determine the amplitude is a combined effect of  $e_{\text{Cr}}$  and  $e_{\text{SiC}}$ . The ratio  $A_{\text{nor}, >100\text{kHz}} / A_{\text{nor}, 400\text{Hz}} = \sqrt{(k\rho c_p)_{\text{Si}} / (k\rho c_p)_{\text{eff}}}$  thereby decreases against the frequency increasing. It is easily understood that the amplitude of thermal radiation is a constant for a pure bulk material because of the constant effusivity. Nevertheless, the ratio of the normalized amplitude at sufficiently high frequencies to that at low frequencies can be used as a quick indicator to evaluate the effusivity ratio of the film to the substrate.

The amplitude method has the feature that the interfacial thermal contact resistance is less sensitive. It can thereby help determine the thermal conductivity of a film precisely with little effect from the unknown interfacial resistance. Moreover, the ratio of normalized amplitude provides a good way to directly evaluate the effusivity of the film of interest.

## CHAPTER 3

PHOTOTHERMAL CHARACTERIZATION OF CROSS-PLANE THERMAL TRANSPORT  
IN SPIDER SILK FILM

This chapter focuses on the cross-plane thermal transport study of the films made from native spider silk protein (major ampullate) that have either been cast directly from freshly dissected glands or from glands dissolved in hexafluoroisopropanol, HFIP. Two spider species are studied: *Nephila clavipes* (golden orb-weaver) and *Latrodectus hesperus* (Western black widow). Based on the observation in the last chapter that the thermophysical properties can reflect the internal structures of the film of interest to some extent, the structure of untreated spider silk films and heat-treated HFIP films are studied and correlated with the thermophysical property change, in anticipation of revealing the unique structure of spider silk films and how energy transport is achieved. Additionally, the PT technique is used to characterize the thermophysical properties along the thickness direction of the films of interest.

## 3.1. Sample preparations

To better understand the relationship between thermophysical properties of spider silk and protein structures from different film casting methods, two types of samples from two spider species, *N. clavipes* and *L. hesperus*, are prepared in this study. The first type of films is major ampullate silk films that are cast on glass slides directly from freshly dissected major ampullate glands (as “fresh films” hereafter). For each slide, one pair of major ampullate glands is dissected from an individual adult female spider in 1X saline-sodium citrate (SSC) solution. The major ampullate glands are then moved to a water bath, where the surrounding gland tissue is

carefully removed, leaving just the silk material. The silk material remains in the gland. The silk mass is then placed on a glass slide and flattened into a film using a spatula dipped in 50% ethanol to prevent sticking. The film is air-dried. Each *L. hesperus* fresh film contains approximately 35  $\mu\text{g}$  of protein while each *N. clavipes* fresh film contains approximately 400  $\mu\text{g}$  of protein. *N. clavipes* fresh films have more protein because a *N. clavipes* major ampullate gland (Fig. 3.1a, left) is much larger than a *L. hesperus* major ampullate gland (Fig. 3.1b). *N. clavipes* major ampullate glands and films are also distinguished by a bright yellow color (Fig. 3.1a).

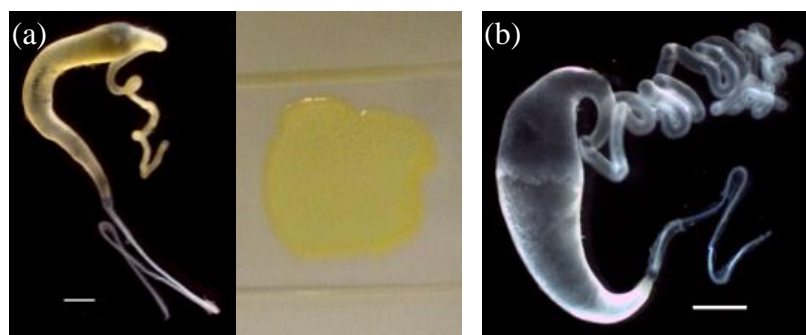


**Figure 3.1.** (a) *L. hesperus* major ampullate gland, scale bar = 1 mm. (b) *N. clavipes* major ampullate gland (left image, scale bar = 1 mm) and HFIP film (right image). Note translucence and bright yellow color of the silk.

The second type of films is made from major ampullate silk glands dissolved in HFIP (referred to as “HFIP films”). For *N. clavipes*, two pairs of major ampullate glands are combined in a microfuge tube. For *L. hesperus*, five pairs of major ampullate glands are combined in another microfuge tube. Each tube of glands is dissolved overnight in 1300  $\mu\text{L}$  HFIP, centrifuged to remove insoluble debris, and the HFIP evaporated to about 500  $\mu\text{L}$ . For each film, 100  $\mu\text{L}$  of HFIP solution is spread onto a glass slide and allowed to air dry. As with the fresh films, the *Nephila* HFIP films have a bright yellow color. The *N. clavipes* and *L. hesperus* HFIP films contain approximately 140  $\mu\text{g}$  and 40  $\mu\text{g}$  of protein, respectively.

To make thicker HFIP films for heat treatment experiments, an 8 mm diameter washer is mounted flatwise on a glass slide. The HFIP solutions are prepared similarly as above. Specifically, for *N. clavipes*, one pair of major ampullate glands is put into a microfuge tube and for *L. hesperus*, five pairs of major ampullate glands are put in another microfuge tube. Each set of glands is dissolved in approximately 1000  $\mu\text{L}$  of HFIP overnight. After centrifugation to remove insoluble debris, the HFIP is evaporated until 300  $\mu\text{L}$  for *N. clavipes* and 600  $\mu\text{L}$  for *L. hesperus*. These volumes are selected to approximate the same protein concentration as the previous HFIP films. For each species, 100  $\mu\text{L}$  of the HFIP solution is slowly pipetted onto each glass slide in the middle of the washer and allowed to air dry. The result is a thickened HFIP film. For these thickened HFIP films, the approximate protein amounts are 135  $\mu\text{g}$  and 120  $\mu\text{g}$  per *N. clavipes* and *L. hesperus* films, respectively.

### 3.2. Structure characterization using Raman spectroscopy

All spider silk films are first characterized by using Raman spectroscopy and the representative spectrum of each film is shown in Fig. 3.1. Spectra are all recorded at room temperature (20 °C) in open air. A confocal Raman spectrometer (Voyage, B&W Tek, Inc.) installed with a 532 nm excitation laser and a microscope (Olympus BX51) is employed for the characterization. A 50 $\times$  microscope objective is used to focus the laser beam. The beam is about 8  $\mu\text{m}^2$  at the focal spot. The glass slide is mounted on a three-dimensional nanostage (Max 311D). The resolution of the Raman spectrum is 1.05-1.99  $\text{cm}^{-1}$ .

### 3.2.1 Films of *Nephila clavipes*

Figures 3.2a and 3.2b contain two Raman spectra from  $500\text{ cm}^{-1}$  to  $1750\text{ cm}^{-1}$  for *N. clavipes* samples. According to previous work [85-87], most peaks in this range are related to detailed structures of the spider silk film. To get a sound spectrum, the Raman integration time is set to 10s for the *N. clavipes* films and the laser energy is  $8.6 \times 10^8\text{ W/m}^2$ . *N. clavipes* silk films have a yellow color that causes a strong background as shown in the Raman spectra. Table 3.1 lists the important observed peaks in Figs. 3.2a and 3.2b, and the corresponding chemical bonds in silk proteins are assigned.

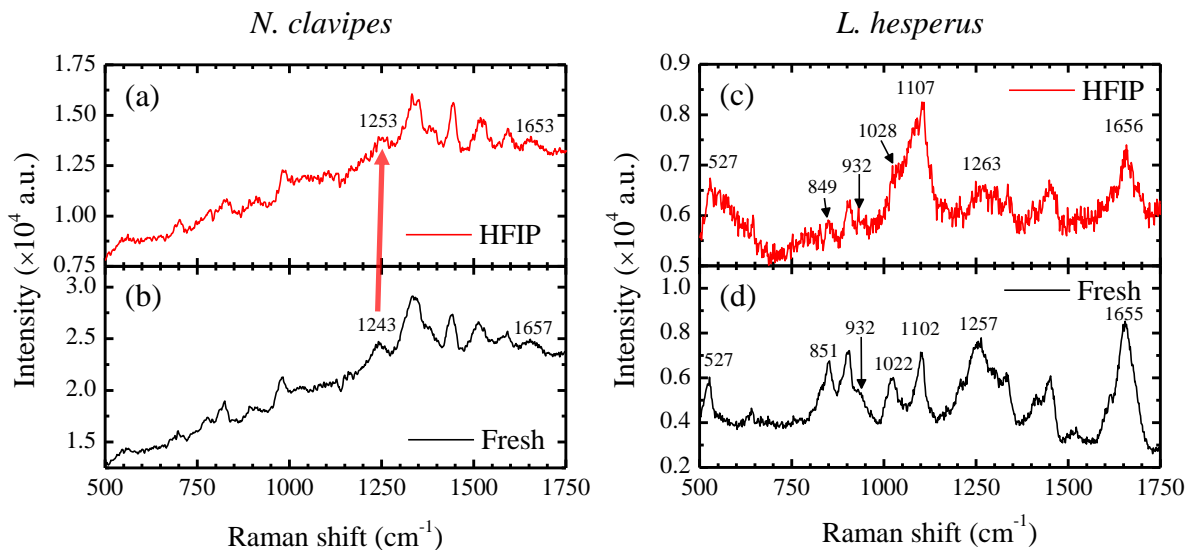


**Figure 3.2.** Raman spectra from  $500\text{ cm}^{-1}$  to  $1750\text{ cm}^{-1}$  for *N. clavipes* (a) HFIP film (b) fresh film, and for *L. hesperus* (c) HFIP film and (d) fresh film. This region is tightly related to internal structures of silk films.

In Figs. 3.2a and 3.2b, profiles of both spectra are similar since they are all extracted from major ampullate glands of *N. clavipes*. The Raman intensity of the fresh film (Fig. 3.2b) is higher because it is thicker and has more protein than the HFIP film (Fig. 3.2a). The fresh liquid silk protein from major ampullate glands is viscous and quickly solidifies during sample preparation. Thus, it is hard to make the film thin. Compared with the fresh liquid silk protein,

the silk protein-HFIP solution is less viscous. It covers a larger area on the glass slide and forms a thinner film. Furthermore, the fresh film contains more proteins than the HFIP film. Therefore, these two reasons likely cause the different intensities of Raman peaks for the fresh film and the HFIP film despite using the same conditions for the Raman spectroscopy.

**Table 3.1.** Detailed assignment of major peaks in Raman spectra of *N. clavipes* and *L. hesperus* major ampullate silk films [85, 86].

Assignment	Peak position (cm <sup>-1</sup> )			
	<i>N. clavipes</i> Fresh	HFIP	<i>L. hesperus</i> Fresh	HFIP
Ala			527	527
Fermi resonance of the Tyr doublet $\alpha$ -helices			$\alpha$ -helices	$\alpha$ -helices
			851	849
			932	932
In-plane stretching of benzene ring Skeletal C <sup><math>\alpha</math></sup> -C <sup><math>\beta</math></sup> stretching			$\alpha$ -helices	$\alpha$ -helices
			1022	1028
Amide III	1243	1253	1257	1263
	$\beta$ -sheets	Random coils	Random coils	Random coils
Amide I	1653	1657	1655	1656
	$\alpha$ -helices and Random coils			
Mass of protein	400 $\mu$ g	140 $\mu$ g	35 $\mu$ g	40 $\mu$ g

The most obvious difference between the HFIP film and the fresh film is the location of the amide III peak. The location of this peak differs in the two spectra, indicating the difference in the structures of protein crystals between these two samples. The broad amide III peak locates between 1243 cm<sup>-1</sup> and 1253 cm<sup>-1</sup> in HFIP film. It may be composed of multiple split peaks, which implies the existence of both random coils and antiparallel  $\beta$ -sheets. However, for the fresh film, the clear amide III peak at 1243 cm<sup>-1</sup> indicates antiparallel  $\beta$ -sheets. They may be

formed in fresh film during quick solidification. The difference between these two films could result from the solvent used in the production of the HFIP film. The chemical  $(\text{CF}_3)_2\text{CHOH}$  contains F and O elements, which can form a stronger hydrogen bond with N element in silk protein and thus will prevent protein crystals of secondary structures from forming. Therefore, it explains why fewer antiparallel  $\beta$ -sheets exist in HFIP film.

### 3.2.2. Films of *Latrodectus hesperus*

The same analysis is applied to Raman spectra of *L. hesperus* films. Two spectra are shown in Figs 3.2c and 3.2d and detailed assignments of main peaks are also listed in Table 3.1. Although the HFIP film and fresh film have similar amounts of protein, as the *N. clavipes* films, the HFIP film is spread over a larger area. Therefore, the lower concentration of protein in the HFIP film compared to the fresh film is reflected by the weaker intensity of all peaks. The HFIP film has a very weak amide III peak at  $1263\text{ cm}^{-1}$  and an amide I peak at  $1656\text{ cm}^{-1}$ . These two locations are characteristic locations for the amide III and amide I peaks in random coils, respectively. A relatively weak and broad peak is near  $527\text{ cm}^{-1}$ , which is assigned to alanine (Ala) configuration in  $\alpha$ -helices. For the fresh film in Fig. 3.2d, it has qualitatively the same structure as the HFIP film because some locations of peaks of the fresh film match those of the HFIP film. The amide III peak of fresh film is at  $1257\text{ cm}^{-1}$  and amide I peak is at  $1655\text{ cm}^{-1}$ , and both of them represent the random coils. However, compared with the HFIP film, the fresh film has a relatively strong sharp peak at  $527\text{ cm}^{-1}$ , indicating the existence of more  $\alpha$ -helices. Another peak at  $932\text{ cm}^{-1}$  refers to  $\alpha$ -helices appearing as a shoulder in both spectra of fresh and HFIP films.

Some differences exist between these two spectra in Figs. 3.2c and 3.2d. The peak at  $1022\text{ cm}^{-1}$  for the fresh film (Fig. 3.2d) is clear and a little lower than the peak at  $1102\text{ cm}^{-1}$ , but for the HFIP film, this peak (approximately at  $1028\text{ cm}^{-1}$  in Fig. 3.2c) is weak and is overlapped by the one at  $1107\text{ cm}^{-1}$ . This peak ( $1022\text{ cm}^{-1}$ ) is assigned to the in-plane stretching of benzene ring (Phenylalanine). The fresh film has another strong peak at  $851\text{ cm}^{-1}$ , which represents the fermi resonance of the Tyrosine (Tyr) doublet. Instead, the HFIP film shows a corresponding peak approximately at  $849\text{ cm}^{-1}$  in Fig. 3.2c but its intensity is near the noise level. Both  $851\text{ cm}^{-1}$  and  $1022\text{ cm}^{-1}$  peaks refer to two amino side chains and can be easily detected in fresh film because the fresh film has more proteins under the focal spot. Also, more crystals in fresh film help increase the protein density. For *L. hesperus* samples, the solvent reduces the formation of protein secondary structures in HFIP films, resulting in more random coils than in fresh films.

Both *N. clavipes* and *L. hesperus* films have major peaks for random coils and  $\alpha$ -helices mixtures. The  $\alpha$ -helices and some other structural bonds are more clearly found in *L. hesperus* films than in *N. clavipes* films. The difference in structure between *L. hesperus* and *N. clavipes* films may be due to the proportion of MaSp1 to MaSp2. Both MaSp1 and MaSp2 have poly-alanine regions, which are expected to contribute to the  $\alpha$ -helices. MaSp2, however, contains appreciable amounts of proline, which are less favorable for  $\alpha$ -helices. Based on amino acid composition data, *L. hesperus* major ampullate silk has a higher ratio of MaSp1 to MaSp2 compared to *N. clavipes* major ampullate silk (5:2 vs. 3:2, respectively) [88-91]. Raman peaks for other functional groups in random coils are more obvious for *L. hesperus* film.

### 3.3. Thermal energy transport

#### 3.3.1. Fundamentals of the photothermal technique

For the PT characterization of energy transport along the thickness direction in the spider silks films, the original film is first coated with a 100 nm thick Au film in our sputter coating system (Denton: Desk V). Au is chosen for the surface coating due to its high thermal conductivity, which improves the thermal conduction between Au and samples. The optical absorption length of Au for the laser with a wavelength  $\lambda = 809$  nm is 13.2 nm [80] noting that 100 nm is thick enough to protect samples from being directly excited by the laser. A modulated laser is then used to irradiate and heat the surface of the Au film (Fig. 3.3a). The temperature of the surface rises as the surface absorbs the laser energy. Thus, when the heating laser is modulated periodically, a periodic temperature variation will occur at its surface. This temperature variation will have a phase shift relative to the modulated laser beam. This phase shift largely depends on thermophysical properties of underlayers (silk films in this work). By fitting the phase shift variation against the modulation frequency, thermophysical properties of underlayers can be determined. Details of the PT principles and theoretical solution can be found in previous works [18-21].

The setup of the PT measurement is the same as in Fig. 2.1b. A modulated infrared diode laser (BWF-2, BWTEK) with a wavelength of 809 nm irradiates the surface of the Au layer that is on the spider silk film. The laser beam follows the Gaussian distribution and the spot size of the laser focused on the sample surface is approximately 0.7 mm  $\times$  1.4 mm [19]. It is modulated in a wide frequency range from 17 Hz to 20 kHz. Its power is about 2.1 W after modulation. The thermal emission due to temperature variation on the Au surface is measured by an infrared

detector (J15D12, Judson Technology). A Germanium (Ge) window is placed in front of the detector to filter the diffuse reflection and only allows the thermal emission to pass through. The signal from the infrared detector is transferred to a pre-amplifier and collected by a lock-in amplifier (SR830, Stanford Research) that is controlled by a PC for data acquisition.

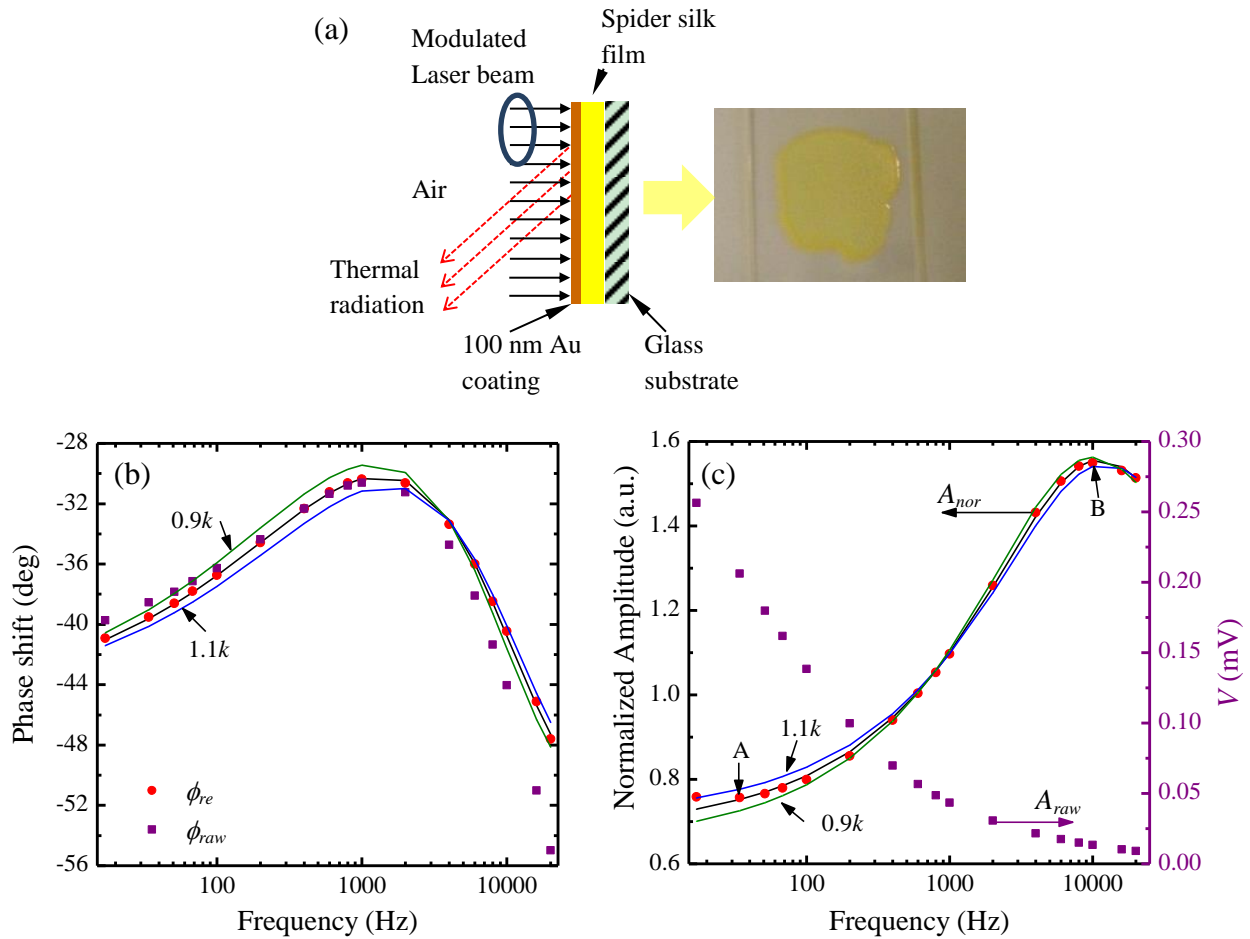


**Figure 3.3.** (a) The mechanism of the PT experiment showing the sample structure. (b) Raw phase shift  $\phi_{raw}$  (purple squares), real phase shift  $\phi_{re}$  after calibration (red dots), and the fitting curve (black line). The thermal conductivity is determined at 0.270 W/m·K. Theoretical curves with thermal conductivity of 0.243 W/m·K (green line) and 0.297 W/m·K (blue line) demonstrate the fitting uncertainty. The theoretical fitting agrees well with experimental data. (c) Normalized amplitude  $A_{nor}$  (red dots) and raw amplitude  $A_{raw}$  (purple squares) change with the frequency.

In the characterization, the experimental setup will inevitably induce systematic time delay. The PT measurement is run with a clean silicon wafer with 100 nm gold coating for

system time delay calibration. The Ge window is moved away and the detector collects the scattered laser light. The measured phase shift and amplitude are both used in phase shift data processing and amplitude-based data analysis as detailed below.

### 3.3.2. Thermophysical properties determination based on phase shift

After the experimental setup is calibrated, the system phase shift ( $\phi_{cal}$ ) is ruled out by directly subtracting calibration phase shift from the raw data ( $\phi_{raw}$ ) of samples. A program developed in our lab is used to fit the phase shift to determine the film properties. The results with the *L. hesperus* HFIP film (HFIP2) is shown in Fig. 3.3b. The purple squares represent the raw data, and the red dots are real phase shift:  $\phi_{re} = \phi_{raw} - \phi_{cal}$ . The black solid line is the best theoretical fitting curve for the real phase shift. The thickness of this HFIP2 film is 2.24  $\mu\text{m}$  in the tested area. Using the known properties of glass substrate, gold and air [80], the calculated effective thermal conductivity  $k$  is 0.270 W/m·K and the heat capacity per unit volume  $\rho c_p$  is  $1.40 \times 10^6$  J/K·m<sup>3</sup>, where  $\rho$  is density and  $c_p$  is specific heat. Figure 3.3b also shows the experimental uncertainty with 10% variation in  $k$ . It is evident when the  $k$  value is changed by 10% from the best one, significant difference can be observed between the theoretical calculation and experimental data. Thus, the determined  $k$  and  $\rho c_p$  have an uncertainty better than 10%.

All thicknesses  $d$ , fitted effective thermophysical properties  $k$  and  $\rho c_p$ , and thermal effusivity,  $e$ , of films for both *N. clavipes* and *L. hesperus* are summarized in Table 3.2. For *N. clavipes*, two fresh films and two HFIP films have similar  $k$  around 0.370 W/m·K. The thickened HFIP2 film (17.34  $\mu\text{m}$  thick) has the largest  $k$  among four samples, which is 0.404 W/m·K. The thickened film is less smooth and uniform than other types of films. This can be explained by

substances, such as protein crystals, not being well distributed during solidification. The laser spot is quite small when focused on the sample surface and that area might have higher content of substances of thermal conductivity. As revealed before in Figs. 3.2a and 3.2b, the fresh film has some antiparallel  $\beta$ -sheet crystals that the HFIP film does not have. Such structure difference gives negligible difference in thermophysical properties considering the 10% experimental uncertainty. It is hypothesized that the antiparallel  $\beta$ -sheet crystal in the fresh film is randomly aligned since it does not increase the thermal conductivity.

**Table 3.2.** Thermophysical properties determination based on phase shift and amplitude.

Sample index	Phase shift fitting				Amplitude fitting		
	$d$ ( $\mu\text{m}$ )	$\rho \cdot c_p$ ( $10^6 \text{ J/K}\cdot\text{m}^3$ )	$k$ ( $\text{W/m}\cdot\text{K}$ )	$e$ ( $\text{W}\cdot\text{s}^{1/2}/\text{m}^2\cdot\text{K}$ )	$\rho \cdot c_p$ ( $10^6 \text{ J/K}\cdot\text{m}^3$ )	$k$ ( $\text{W/m}\cdot\text{K}$ )	$e$ ( $\text{W}\cdot\text{s}^{1/2}/\text{m}^2\cdot\text{K}$ )
<i>N. clavipes</i> (golden orb-weaver)							
fresh1	18.58	1.57	0.365	757.0	1.53	0.547	914.8
fresh2	28.19	1.34	0.388	721.0	1.48	0.448	814.3
HFIP1	5.69	1.73	0.343	770.3	1.39	0.359	706.4
HFIP2	17.34	1.57	0.404	796.4	1.38	0.610	917.5
<i>L. hesperus</i> (Western black widow)							
fresh1	21.32	1.74	0.306	729.7	2.08	0.396	907.6
fresh2	6.53	1.78	0.355	794.9	1.68	0.397	816.7
HFIP1	3.39	1.14	0.435	704.2	1.20	0.668	895.3
HFIP2	2.24	1.37	0.270	608.2	1.55	0.264	639.7
HFIP3	2.06	1.31	0.280	605.6	1.67	0.270	671.5

For all *L. hesperus* samples, the obtained average  $k$  and  $\rho c_p$  from two fresh films are slightly larger than HFIP films. For example, they are 0.355 W/m·K and  $1.78 \times 10^6 \text{ J/K}\cdot\text{m}^3$  for the fresh2 film, while for the HFIP2 film,  $k$  is about 0.270 W/m·K and  $\rho c_p$  is  $1.37 \times 10^6 \text{ J/K}\cdot\text{m}^3$ . The difference between fresh and HFIP films should be caused by the different preparation methods. Solubilization of proteins affects the formation of internal structures when preparing HFIP films.

In agreement with Raman spectra of these two kinds of samples, the HFIP film has weaker and broader Raman peaks of structures than the fresh film since the HFIP blocks the formation of hydrogen bonds in silk protein and then reduces protein crystals of secondary structures. It is well known that crystals have structures favoring thermal energy transport that random coils do not. HFIP films have more random coils than fresh films, so they have a weaker capability of transferring the heat and thus a lower  $k$ . The conclusion that the HFIP film has a lower thermal conductivity than the fresh film is not very strong since we do observe one HFIP film (HFIP1) with a higher thermal conductivity (0.435 W/m·K) than all other four films. Furthermore, due to a larger quantity of crystals, fresh films have more compact structures and thus higher  $\rho c_p$  than HFIP films. Also, it is known that hydrogen bonds are good at storing thermal energy. Therefore, the low hydrogen bond concentration caused by the HFIP solution in the HFIP film will lower its heat capacitance.

Comparing the thermophysical properties of *N. clavipes* and *L. hesperus* samples, all films of *N. clavipes* have similar  $k$ , while the two types of *L. hesperus* films have different  $k$ . The  $k$  of fresh films of *L. hesperus* is similar to the *N. clavipes* samples, but the  $k$  of HFIP films of *L. hesperus* is lower, which can be attributed to their less crystalline structure. When comparing the heat capacity per unit volume:  $\rho c_p$ , films of *N. clavipes* have similar heat capacities. However, the *L. hesperus* films are significantly different in that the heat capacity of HFIP films is lower than fresh films because of the looser internal structures of HFIP films. Evidently, HFIP solvent has a large effect on the internal structures that form during solidification of *L. hesperus* films. This could be explained by the thin *L. hesperus* HFIP films being composed of less concentrated protein than either fresh or thickened HFIP *N. clavipes* films. With less protein, there is less opportunity for

structure formation. Therefore, *L. hesperus* HFIP films have the most random coils, the smallest thermal conductivity and the lowest heat capacity.

### 3.3.3. Thermophysical properties determination based on amplitude

The amplitude of thermal radiation from the Au surface is another significant parameter we measure for calculating the thermophysical properties of samples. The  $k$  of spider silk will strongly affect the temperature rise at the Au surface during heating. If  $k$  is larger, the thermal energy in the Au layer will easily and quickly transfer into the spider silk layer so that the temperature on the Au surface will be lower than that with a lower  $k$  underlayer. We can determine the  $k$  of spider silk layer through fitting the amplitude of thermal radiation from the Au surface under different frequencies as we do in the phase shift fitting.

This amplitude fitting is a new analysis method that we developed and applied in this work. Figure 3.3c shows the raw ( $A_{raw}$ ) amplitude data of HFIP2 film of *L. hesperus* (purple square dots). The amplitude quickly decreases as the frequency increases. However, the experimental system will inevitably produce systematic uncertainty and the random amplitude oscillation of the incident laser will also affect radiation signals. These systematic and laser effects can be eliminated by dividing the raw data of the laser amplitude ( $A_{cal}$ ) measured in calibration.

Furthermore, the incident laser is modulated by a function generator during the whole PT experiment. The raw amplitude is also affected by frequency  $f$ . The measured amplitude decreases quickly as the frequency increases since the heating time is shorter in each period in

the higher frequency range. The sensitivity is thus lower in the higher frequency range so that the modulation effect should be considered. The processed result  $A_{raw}/A_{cal}$  is further normalized by multiplying  $\sqrt{f}$  (the physics discussed below). The final normalized amplitude,  $A_{nor}$ , is shown in Fig. 3.3c. Opposite to the raw data,  $A_{nor}$  is increasing with the frequency and becomes more sensitive especially in the high frequency range.

Figure 3.3c also shows the fitting result (black curve) of HFIP2 film of *Latrodectus hesperus* for the normalized amplitude. The same parameters of other materials used in phase shift fitting are used in this amplitude fitting, and the fitted  $k$  and  $\rho c_p$  for the spider silk film is 0.264 W/m·K and  $1.55 \times 10^6$  J/K·m<sup>3</sup>, respectively. The theoretical fitting matches the experimental results well. The uncertainty of the fitting process is also plotted as two other curves with 10% variation of  $k$ . The green curve is the curve with  $k = 0.238$  W/m·K and blue curve is the curve with  $k = 0.292$  W/m·K. The  $k$  from the phase shift and the amplitude fitting methods are very close to each other while there is only a slight difference between  $\rho c_p$ . Deviations between the two fitting methods may come from the residual calculation in the theoretical computing. Fitted results based on amplitude are summarized in Table 3.2 for all samples. Briefly, the amplitude fitting gives the same conclusion as the phase shift fitting about how the HFIP affects the film structure and thermophysical properties. It needs to be pointed out the amplitude fitting is based on how the normalized amplitude changes with frequency, and does not use absolute values. It has less accuracy when compared with the phase shift fitting. Nevertheless, it provides a reasonable comparison to check the phase shift fitting results.

When the laser irradiates the Au surface of the sample, the energy input amount depends on the irradiation time and incident intensity. In accordance with Eq. 2.7, the normalized amplitude is related to effusivity of the sample:  $e = \sqrt{k \cdot \rho \cdot c_p}$ , including that of the spider silk film and glass substrate.

Data points A ( $f_A = 51$  Hz) and B ( $f_B = 10000$  Hz) in Fig. 3.3c are selected for further discussion of the amplitude fitting method. Point A is in the low frequency region and B is in the high frequency region, and then we have  $A_{nor,B} / A_{nor,A} = 2.07$ . The amplitude value at point B is largely determined by the properties of spider silk since the thermal diffusion length is very short, mostly constrained within the film thickness. In the low frequency range, heat transfer has a long diffusion depth, passing the film, and significantly penetrating into the glass substrate. So  $k \cdot \rho \cdot c_p$  is mostly the property of pure glass slide. To test our results, the values of density, specific heat and thermal conductivity of glass from references [80] and spider silk we measured based on phase shift are used here. The ratio of  $k \cdot \rho \cdot c_p$  of glass to that of the spider silk is 5.6. Thus, based on Eq. 2.7, we have  $A_{nor,B} / A_{nor,A} \sim \sqrt{(k \rho c_p)_{spider} / (k \rho c_p)_{glass}} = 2.37$ , which is very close to the ratio directly calculated from the normalized amplitude: 2.07. This estimation is slightly larger than the experimental figure because  $k \cdot \rho \cdot c_p$  is not the exact value of the pure glass in the low frequency range. Both spider silk and glass will affect the amplitude of thermal radiation from the Au surface. In the high frequency range, glass has a very weak effect on the surface radiation since the thermal diffusion length is quite short in the spider silk layer.

### 3.3.4. Thermal treatment

Heat treatment can provide an opportunity to transform the internal structure of spider silk proteins. Previous works showed that random coils will transform into secondary structures by using heating process, such as  $\alpha$ -helices and antiparallel  $\beta$ -sheets [92]. Here, heat treatment is applied to the thickened HFIP films to study the transformation of protein structures. Films are heated at 20 °C, 40 °C, 60 °C, 80 °C, 95 °C, 120 °C, 140 °C, 160 °C, and 180 °C, respectively, with one temperature per run. For temperatures below 100 °C, films are placed in a glass jar sealed with a cap in a water bath. The temperature of the water around the glass container is maintained for 4 hours. For temperature over 100 °C, the sample is directly heated in an oven. A thermal couple is placed next to the sample to verify that the heating temperature achieved in the oven matches the instrument setting. Both *N. clavipes* and *L. hesperus* thickened HFIP films are heated at every temperature. All films burned at 200 °C. Since the PT experiments are done at room temperature, for consistency between PT and Raman measurements, Raman spectra are collected after each sample is cooled down at ambient room temperature for about one hour, and then the PT technique is applied to study the sample's thermophysical properties.

For the *N. clavipes* thickened HFIP film, figures 3.4a and 3.4b show variations of Raman spectra and effusivity with increasing heat treatment temperatures. Comparing the spectrum in Fig. 3.1a and the one of 20 °C in Fig. 3.4a, we find that the former has more peaks. The only difference in producing these two kinds of films is the solidification process; the protein stock and solvents are the same. It may be caused by the different surface extension. For the HFIP film used in the previous section, the spider silk solution is dropped on a glass slide to form a film without restriction, and the surface extension is the only factor affecting the film shape. However,

for the thickened HFIP film, the solution is pipetted slowly in a fixed washer and the shape of the film is maintained during drying. The effect of surface extension should be smaller.

For the *N. clavipes* thickened HFIP film, figures 3.4a and 3.4b show variations of Raman spectra and effusivity with increasing heat treatment temperatures. Comparing the spectrum in Fig. 3.2a and the one of 20 °C in Fig. 3.4a, we find that the former has more peaks. The only difference in producing these two kinds of films is the solidification process; the protein stock and solvents are the same. It may be caused by the different surface extension. For the HFIP film used in the previous section, the spider silk solution is dropped on a glass slide to form a film without restriction, and the surface extension is the only factor affecting the film shape. However, for the thickened HFIP film, the solution is pipetted slowly in a fixed washer and the shape of the film is maintained during drying. The effect of surface extension should be smaller.

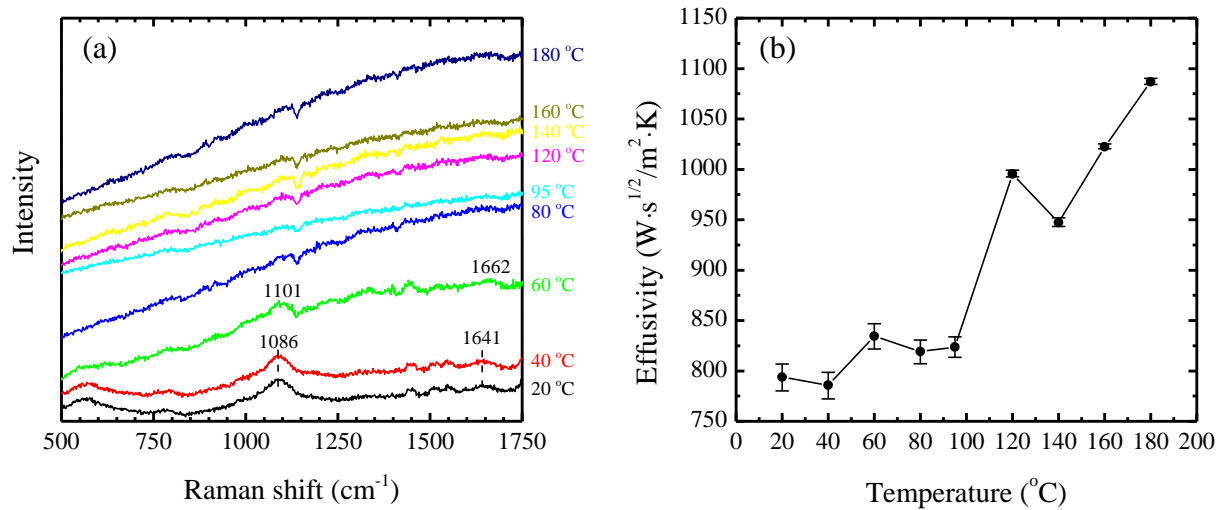


**Figure 3.4.** (a) Raman spectra of the thickened major ampullate HFIP silk film of *N. clavipes* heated under different temperatures. The observed crystallization happens at 60 °C as peaks shift to the wavenumber representing  $\alpha$ -helices in the Raman spectrum. These Raman peaks weaken and disappear gradually under continued heating processes. (b) The effusivity with error bars of this film after heat treatment at different temperatures.

The Raman spectra remain the same for this film at 20 °C and 40 °C as shown in Fig 3.4a. The crystallization starts at 60 °C demonstrated by the shift of peaks. The 1086 cm<sup>-1</sup> peak at 20 and 40 °C shifts to 1101 cm<sup>-1</sup> at 60 °C. This means the C-C skeletal bond configuration changes from unordered status to  $\alpha$ -helices [93]. It could be caused by the high thermal energy and the evaporation of residual HFIP in the film. Heat energy enhances the movement of molecules and more hydrogen bonds form between polar groups in proteins and favor crystal formation. Furthermore, the boiling point of HFIP is 58.2 °C. Since all film samples are air dried, there should be a small amount of HFIP in them. When the heating temperature reaches 60 °C, the hydrogen bond between HFIP and protein breaks and the HFIP molecules dissipate into the air. The left polar groups can then connect with others and thus increase the hydrogen bonding within and among protein molecules. Moreover, the 1641 cm<sup>-1</sup> peak at 20 °C and 40 °C shifts to 1662 cm<sup>-1</sup> after heat treatment at 60 °C. This is also caused by the formation of  $\alpha$ -helices [94]. As the temperature continues to increase, peaks become weaker in the Raman spectrum and the background of the spectrum increases. This background of the spectrum is caused by the yellow color of the film itself and the carbonization of protein at high temperatures since films are heated in the open air. During heating, the high thermal energy and the interaction between proteins and gas molecule may cause the unstableness and the break of the hydrogen bonds.

Figure 3.4b shows the measured effect of heat treatment on effusivity. One film is continuously used in all heating runs and the thickness of this film is considered to be constant throughout the experiment. The thickness is about 11.43  $\mu\text{m}$  for the *N. clavipes* thickened HFIP film. The thermal effusivity is used to explain the thermophysical properties of the film in the PT experiment because the error induced by thickness can be ruled out during the fitting process.

Below 60 °C, the effusivity is about  $800 \text{ W}\cdot\text{s}^{1/2}/\text{m}^2\cdot\text{K}$ , and it starts increasing at 60 °C, the beginning of crystalline formation. A sharp decrease appears in the effusivity curve at 140 °C. This temperature is close to the burning point, and silk proteins begin degrading due to the dehydration and oxidation at such high temperature. Random coils fragment into small pieces. The carbonization of proteins also starts at this temperature, with the film darkening due to some proteins becoming carbon. After the temperature exceeds 140 °C, the thermal effusivity and conductivity increase largely because of the increase of carbon content. At 200 °C, the film is completely dark and burned in appearance.  $\rho c_p$  is expected to be constant since the heating process does not change the profile of the film before it is burned, so the thermal conductivity should increase just like the effusivity.

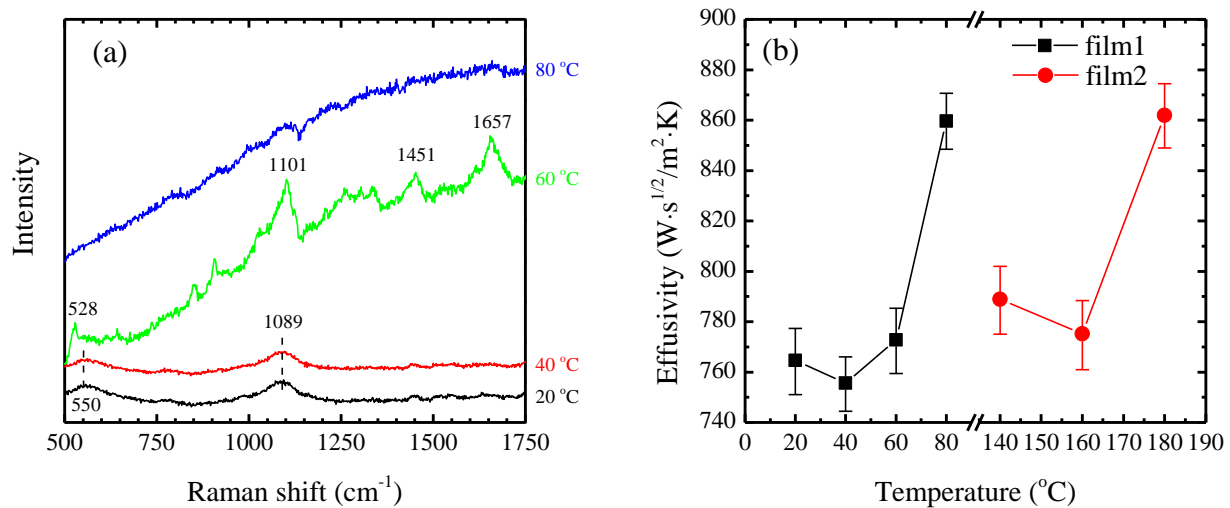


**Figure 3.5.** (a) Raman spectra of the thickened major ampullate HFIP silk film of *L. hesperus* heated under different temperatures. The observed crystallization happens at 60 °C as some clear and representative peaks appear in the Raman spectrum. This crystal structure disappears after being heated at 80 °C. (b) The effusivity with error bars of this film after heat treatment at different temperatures.

Compared to the equivalent sample from *N. clavipes*, the *L. hesperus* thickened HFIP film shows poor adhesion to the glass substrate. It easily peels off after heating at 95 °C so only

four Raman spectra and effusivity are recorded for this film. The film thickness is 10.43  $\mu\text{m}$  for the *L. hesperus* thickened HFIP film (film 1). Before heating the film, the Raman spectrum only has two observed peaks at 550  $\text{cm}^{-1}$  and 1089  $\text{cm}^{-1}$ , as shown in Fig. 3.5a. This characterization is different from the thin *L. hesperus* HFIP film described in the previous section. The thin HFIP film contains some  $\alpha$ -helices while the thickened HFIP films mainly contain random coils before heat treatment. Although the thickened HFIP films have a higher amount of protein (120  $\mu\text{g}$ ), few crystals form in this film. However, the Raman spectrum of the thickened HFIP film is similar to that for *N. clavipes* at 20  $^{\circ}\text{C}$ . This similarity indicates that both films contain mostly random coils in films and no protein crystal is observed. In Fig. 3.5a, no change happens in the Raman spectrum after heat treatment at 40  $^{\circ}\text{C}$ . However, for the spectrum after 60  $^{\circ}\text{C}$  treatment, new peaks suddenly appear in the spectrum. Peaks at 528  $\text{cm}^{-1}$ , 1101  $\text{cm}^{-1}$  and 1657  $\text{cm}^{-1}$  represent the existence of  $\alpha$ -helices in the film. Those peaks begin to disappear when the heating temperature continuously increases beyond 60  $^{\circ}\text{C}$ . This can be explained by the heat treatment enhancing the movement of molecules and the breaking of hydrogen bonds.

In Fig. 3.5b, the effusivity of the HFIP film remains nearly constant before 60  $^{\circ}\text{C}$  and starts increasing largely after that. For the effusivity increase from 60 to 80  $^{\circ}\text{C}$ , although the crystallinity structure disappears, the temperature increase in heating will induce H-bond breaking among molecular chains. This will reduce the phonon scattering among molecular chains, and lead to an increased phonon mean free path. Therefore, the thermal transport capacity will increase, and the thermal effusivity will increase as well. This also explains the effusivity increase from 100 to 120  $^{\circ}\text{C}$  for *N. clavipes* films shown in Fig. 3.4b. Another *L. hesperus* thickened HFIP film (film 2) is heated from 140  $^{\circ}\text{C}$ . It also shows an obvious decrease before

burning at 160 °C, as with the *N. clavipes* film. Random coils in these thickened HFIP films of spiders will transform into  $\alpha$ -helices and no  $\beta$ -sheet is observed during heat treatment. The formation of  $\alpha$ -helices will increase the thermal effusivity and conductivity as the heating temperature increases, but a sharp decrease is observed for these two types of films before they are burned.

## CHAPTER 4

## RAMAN SPECTROSCOPY FOR NANOSTRUCTURE PROBING

This chapter is to explore the very sensitive change of the Raman intensity with various grain size of nanocrystalline silicon on the cleaving edge of a silicon wafer. Raman spectroscopy is utilized to ascertain the size of nanocrystalline silicon in the sub-surface region with a formula in ref. [52], and to study the maximum intensity of the Raman peak. The analyzed Raman results are used to exclude other factors causing the change of the spectroscopy and prove the very high sensitivity of Raman intensity in terms of examining grain size.

## 4.1. Experimental details

A 270  $\mu\text{m}$  silicon (100) wafer (University Wafer) and a 7  $\mu\text{m}$  silicon wafer are used and cleaved by a traditional method. A silicon wafer is placed on a desk and cut on its edge with a knife to make a sharp notch. Then a small needle is placed under the notch and forces applied on both sides of the notch to break the wafer. The sample edge is finally formed when the silicon naturally cleaves along its crystal face. The cleaved silicon edge is cleaned with ethanol before all tests. A confocal Raman spectrometer (Voyage, B&W Tek, Inc.) installed with a 532 nm excitation laser and a microscope (BX51, Olympos) is employed to focus the laser. The spectral resolution is 1-2  $\text{cm}^{-1}$ . During the experiment, a 100 $\times$  microscope objective is used to focus the laser beam and the beam size is about 0.5  $\mu\text{m}$  in diameter at the focal spot as will be detailed later. There is a two-dimensional stage used for mounting the sample, which consists of two one-dimensional stages. One is in the  $x$  direction (NFL5DP20S, ThorLabs) and the other one is in the  $z$  direction (MT1-Z8, ThorLabs). The movement ranges of those two stages are 20  $\mu\text{m}$  in the  $x$

direction with a resolution of 20 nm and 13 mm in the  $z$  direction with a resolution of 0.2  $\mu\text{m}$ . The combined stage is located under the focal spot of the laser beam and can move around the focal spot in the  $z$  direction. When mounting the sample wafer, the optical trace is perpendicular to the cleaved edge of the wafer which is along the  $y$  direction.

The experiment setup is shown in Fig. 4.1a. The laser is focused on the surface of the cleaved silicon wafer, and the scattering signal and Rayleigh scattering signal are both collected by the same objective in the backscattering mode. During the experiment, the stage makes the laser spot move from the center of the cleaved silicon wafer to the edge with a step of 266 nm at the beginning and then the step length is changed into 133 nm after the intensity starts increasing. The step is controlled by adjusting the voltage on an electronic-control box and 1 V adjustment is for 266 nm movement. 1 second integral time is used in this measurement to obtain a strong Raman signal from silicon. The whole measuring system is placed in open air. Due to the resolution limit of the spectrometer, Raman signals are processed to calculate the linewidth, maximum intensity and the precise peak wavenumber shift after all the spectra data obtained. The fitting procedure can be simply described as picking up a segment of Raman data (from  $492.11\text{ cm}^{-1}$  to  $552.45\text{ cm}^{-1}$ ), choosing eight points on both tails of the peak with fixing the  $x$  coordinate as the baseline (four on each side), subtracting the baseline from the original data, and finally using Gaussian function to fit the peak to get the information we need.

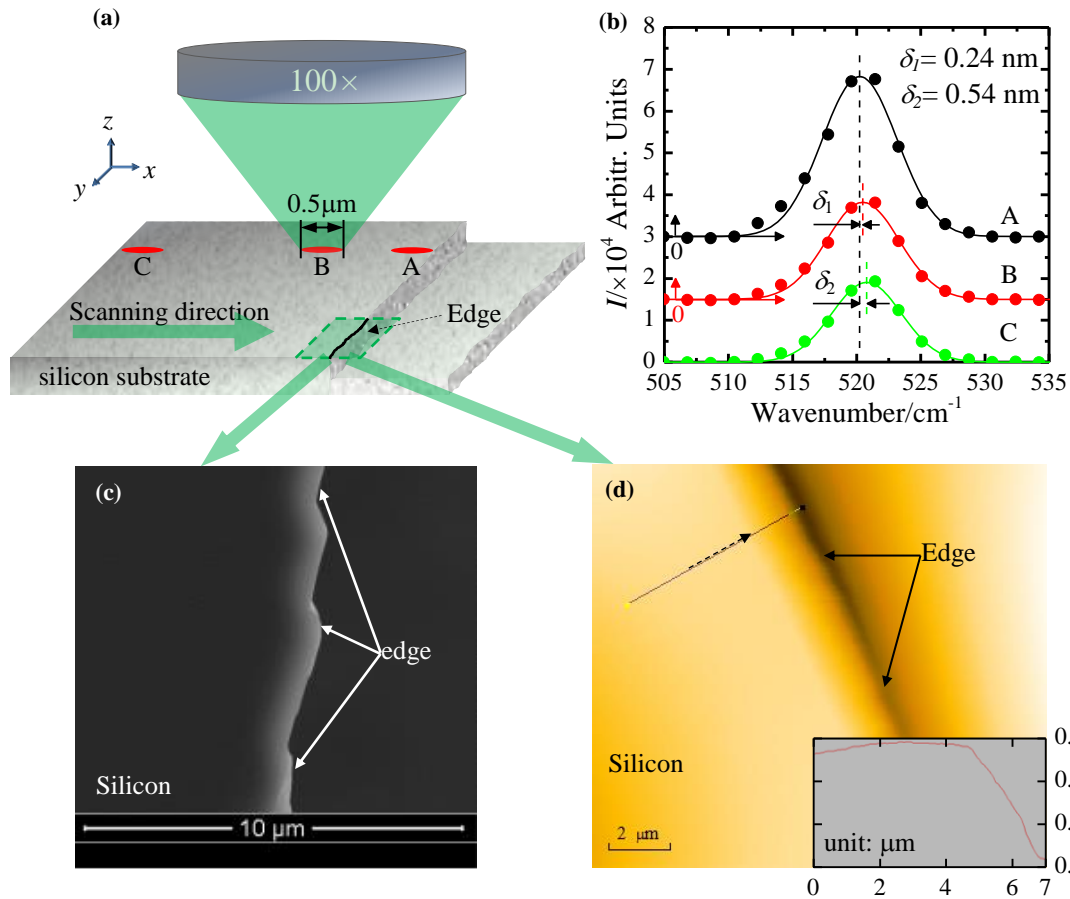


**Figure 4.1.** (a) is a schematic of the experimental setup for Raman experiment with a 100× objective lens (not to scale). The relative location of the laser spot moves along the  $x$  direction shown by green arrow. Red dots show the approximate positions of A, B, C spots. A is mostly near the edge, then B, and C is farthest to the edge; (b) are three the Raman spectra of silicon near  $521\text{ cm}^{-1}$  at selected spots A, B, and C. The dots represent the raw data and curves are from Gaussian fitting, and both of them have the baseline subtracted. For clear comparison, the curves A and B are shifted up, and 0 points of their  $y$  coordinates are shown in the plot; (c) scanning electron micrograph (SEM) shows a smooth surface. The right half of the image is the area which is out focus and shown black, while the left half is the silicon wafer surface. The boundary of the silicon wafer is indicated by white arrows. (d) Atomic force microscopy (AFM) image of the silicon wafer surface is also taken in the same place like that in SEM. The inset plot is the profile of the cross-section measured along the direction of black dash arrow in upper right side of Fig. 4.1d. The boundary of the silicon wafer is indicated by black arrows.

## 4.2. Results and discussions

### 4.2.1. Raman imaging for 270 $\mu\text{m}$ thick silicon wafer

By varying the position of the laser spot on the surface of the cleaved silicon wafer sample, a series of Raman spectra are attained and analyzed. Figure 4.1b shows three typical results of the Raman peaks of silicon with fitting curves near  $521\text{cm}^{-1}$  at selected measuring points A, B and C. The outlines of those peaks change with the location where the signal originates. These three points A, B and C, located from farthest to nearest to the edge respectively, are illustrated in Fig. 4.1a. The black line is from point A which is the nearest the edge, the red line is from B which is in the middle of A and C, and finally C, shown in green line, is the farthest point away from the edge. It is obvious that the intensity, linewidth and Raman wavenumber of these peaks change with the position. The signal from point A has the strongest intensity in Raman spectrum, point B has a weaker intensity, and point C's intensity is the weakest. This intensity change is very large and surprising, about 100% from position C to position A. The linewidth and wavenumber shift of the Raman peak also changed, though the changes are small to observe. Furthermore, there is no  $480\text{ cm}^{-1}$  broad peak appearing in the spectrum, meaning no amorphous silicon formed during cleaving.

In Raman experiment, the intensity of the Raman signal will be affected by the profile of the surface. A rough surface will enhance the Raman intensity largely because it can improve the absorption of the light on the surface [95] due to surface polaritons induced the enhancement of Raman cross-section. The roughness of the magnitude of micrometers can raise an observed enhancement in Raman spectrum. Our sample has a flat surface until the edge which is proved by the results of scanning electron microscope (SEM) and atomic force microscope (AFM)

characterization. In Fig. 4.1c, the SEM measurement is taken under 10 kV in a vacuum. The picture shows that the area is very smooth in 2-3  $\mu\text{m}$  abutting on the edge. Furthermore, contact-AFM is also employed to measure the detailed structure in a  $15 \times 15 \mu\text{m}^2$  area. In Fig. 4.1d, the right hand side of the dark line indicates the silicon surface and the edge, and the left hand side is caused by the system adjustment since the difference in height is too steep to track. The inset graph in Fig. 4.1d is the profile of the cross section at the location of the straight line drawn in the figure. Both SEM and AFM results in Figs. 4.1c and 4.1d illustrate that the surface roughness is very small, and there is no special structure which could increase the roughness. Therefore, the enhanced intensity is not caused by the roughness in the testing area. There should be another reason leading to this sensitive change in Raman intensity, so Gaussian fitting is applied to all those measurement results to obtain more accurate data to analyze.

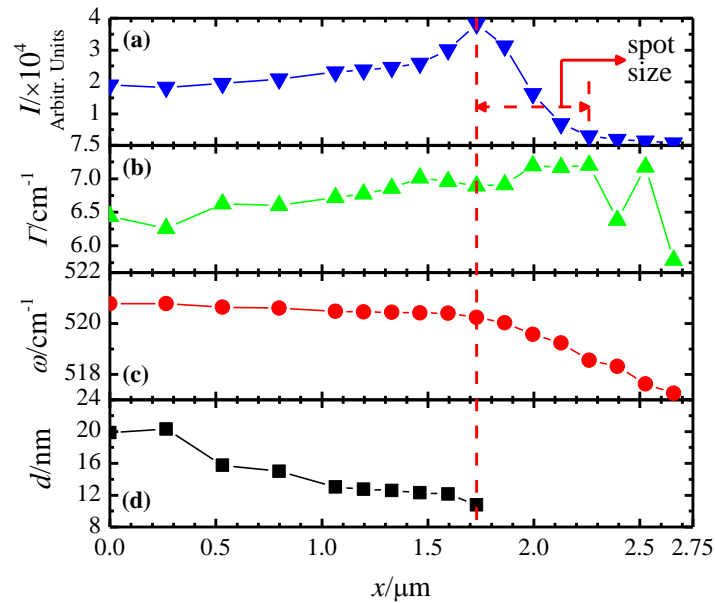


**Figure 4.2.** Raman imaging results from the center to the edge of 270  $\mu\text{m}$  thick silicon wafer. (a) Peak intensity ( $I$ ). The laser spot size is calculated from the highest intensity to 10% of maximum intensity in this plot, (b) width ( $\Gamma$ ), (c) 521  $\text{cm}^{-1}$  peak wavenumber shift ( $\omega$ ), and (d) size of nanocrystalline silicon grain ( $d$ ) change with focal spot from the center to the edge, calculated from  $d = 2\pi\sqrt{B / \Delta\omega}$  in ref.[52]. The red line in this plot shows the actual position of the edge.

With fitting of all the data, Figs. 4.2a - 4.2c show the changes of the intensity ( $I$ ), linewidth ( $\Gamma$ ) and peak wavenumber shift ( $\omega$ ) against the location in the  $x$  direction along which the laser focus spot moves to the cleaved edge of the silicon. The red dash line indicates the edge position. The spot size can be evaluated from Fig. 4.2a. The point having the maximum intensity indicates that the whole laser spot focus on silicon immediately next to the edge. Part of laser irradiates other places when the laser spot keeps moving toward the silicon wafer edge, and therefore the Raman intensity decreases quickly. 90% change of the maximum intensity is used for spot size evaluation and it is about 0.5  $\mu\text{m}$ . During the whole movement of the laser spot, the decrease of the Raman wavenumber shift can be observed while the linewidth of the peak is broadening. The intensity changes in a quite different manner. It first increases quickly and largely from the beginning till the edge. The immediate decline of Raman intensity is caused by decreased power of the laser irradiating the sample when the laser spot gradually moves away from the edge. The location of the focal spot is measured by using a CCD camera and this phenomenon is repeated three times to ensure the reliability. In Fig. 4.2, the range of the change is 4  $\text{cm}^{-1}$  for Raman wavenumber shift and 2  $\text{cm}^{-1}$  for the linewidth. On contrast, the intensity increases by almost 100% from the beginning to the edge, and it is extremely obvious and sensitive with the location of the focal spot.

In ordinary Raman experiments, many factors will affect the spectrum, and the most important one is the focal level because it can cause many other effects. The out-of-focus effect will lower the density of the incident light and therefore lead to effect of heating and the stress decreasing in the sample surface. Both the heat and stress effect will cause the change of the wavenumber shift and Raman linewidth. Also the out-of-focus effect will change the incident

angle of the backscattered Raman signal into the spectrometer, which may cause some Raman signal change. In this experiment, the stage in the  $z$  direction is locked mechanically. However, it may still have a little shift due to vibrations in the surrounding which will finally cause the sample out of focus. To study the out-of-focus effect in our results, a group of Raman spectra are obtained from the middle area of the same sample silicon wafer located in different distances to the focal level in the  $z$  direction. The sample surface level is adjusted near the focal level in a range smaller than  $1\ \mu\text{m}$  in order to analyze the out-focus effect on the silicon surface. The moving step is around  $50\ \text{nm}$ . Raman spectra are recorded at each step with an integration time of  $2\ \text{s}$ , and the background signal is subtracted to obtain sound Raman signals.

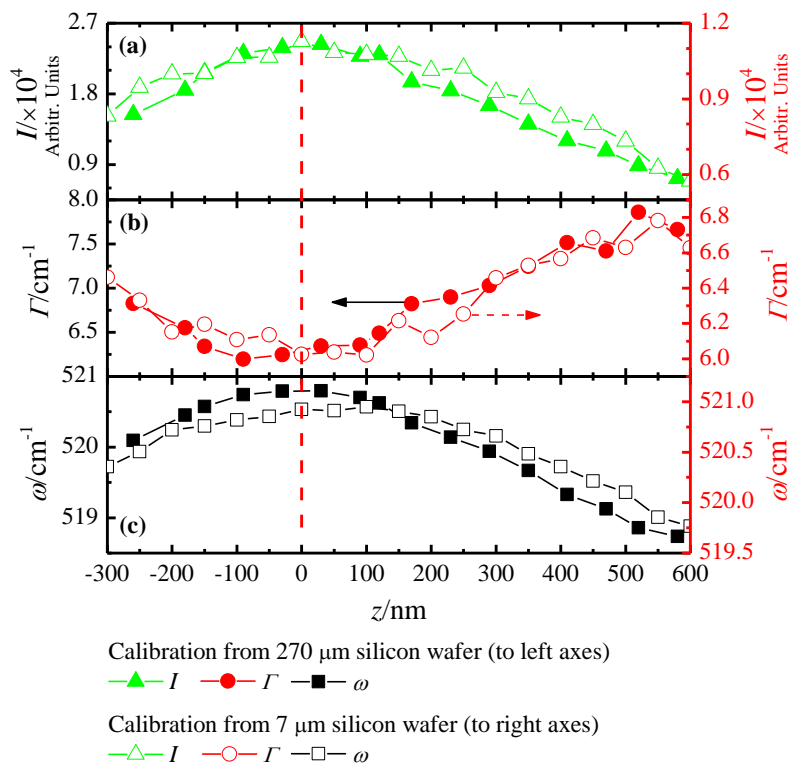


**Figure 4.3.** Variation of the Raman spectrum from different focal levels on two single crystal silicon wafers. (a) Peak intensity ( $I$ ), (b) width ( $\Gamma$ ), and (c)  $521\ \text{cm}^{-1}$  peak wavenumber shift ( $\omega$ ) change with the distance to the focal point. The solid legends represent Raman information for the  $270\ \mu\text{m}$  thick Si wafer and the hollow ones are for the  $7\ \mu\text{m}$  thick Si wafer. The red line in this plot shows the  $0\ \text{nm}$  position in the  $z$  direction and the laser beam is well focused on this level.

Figure 4.3 shows how the Raman wavenumber, linewidth, and intensity change with the  $z$  location. Those solid legends represent the Raman data from 270  $\mu\text{m}$  Si wafer and hollow legends are for 7  $\mu\text{m}$  Si wafer, which is used later. At the beginning, the focal level is below the sample surface. When the sample approaches the focal spot from the upper side, both the laser spot size and the linewidth are decreasing while the peak wavenumber shift and intensity increase. After the surface passes the focal level to a lower position, it reverses the former process: the laser spot and the linewidth become larger, but the Raman intensity and wavenumber shift decrease. Moreover, the maximums of wavenumber and Raman intensity and the minimum Raman linewidth appear at the same focal level, which is indicated at 0 nm with a red dash line in Fig. 4.3.

Compared with the result in Fig. 4.2, although the variation of the peak shift and linewidth are similar, the trend of the intensity change is totally different from the out-of-focus situation. The change ranges are about  $2.5\text{ cm}^{-1}$  for the linewidth and  $2.5\text{ cm}^{-1}$  for the wavenumber in the condition of 600 nm away from the focal point. These ranges are a little larger than those in aforementioned Raman results. Nevertheless, the moving distance in the  $x$  direction is about  $2.6\text{ }\mu\text{m}$  in the whole measurement. If there were a difference in the  $z$  direction from the beginning to the end in our experiment, the tilt angle would be as large as 13 degrees which can be easily detected. Furthermore, the intensity increases and becomes anomalously large when the stage moves in the  $x$  direction. So if there were any movement in the  $z$  direction to make the sample shift from the focal plane, the intensity would become smaller instead of larger. Therefore the results observed in Fig. 4.2 are not induced by the out-of-focus effect due to the stage shift.

Previous work by Webster *et al.*, has mentioned that the residual stress was preserved in and affected the Raman spectrum, too [53]. In that work, a single crystal silicon wafer with a scratch in its surface was used as a test sample. They found that a positive shift of wavenumber of  $521 \text{ cm}^{-1}$  peak when approaching the scratch, meaning compressive stress in the silicon surface. Based on their results, the residual stress will cause different changes in Raman spectrum from ours. Theoretical studies on the electronic structure of Si nanospheres, assuming spherical confinement of phonons, have been reported and its results showed the wavenumber would increase when the diameter became larger [96-99]. This shift was explained as due to localization of phonons at the quasi-isolated crystallites [100].

#### 4.2.2. Nanocrystalline grain size

Our results on the Raman linewidth and wavenumber shift are similar to the results in previous studies of polycrystalline silicon [100], and such similarity indicates there are nanocrystals formed in the area next to the edge during the mechanical cleaving. The formula  $d = 2\pi\sqrt{B/\Delta\omega}$  in ref. [52] is used to determine the size of silicon nanocrystalline grains.  $B$  is  $2.24 \text{ cm}^{-1} \text{ nm}^2$  for Si and  $\Delta\omega$  is the value of Raman wavenumber shift with respect to single crystalline Si peak at  $521 \text{ cm}^{-1}$ . From this formula, the nano-grain size can be calculated, and results are plotted in Fig. 4.2d. The dash line in Fig. 4.2 indicates the edge location. From the calculation, the size of Si nanocrystalline grains changes from 20 nm to 10 nm in silicon surface. Meanwhile, the Raman linewidth increases from  $6.5 \text{ cm}^{-1}$  to  $7.0 \text{ cm}^{-1}$  and the peak location down shifts from  $521 \text{ cm}^{-1}$  to  $520 \text{ cm}^{-1}$ . However, the intensity of the Raman peak increased by about 100% because of the variation of grain size.

The change of Raman intensity with the crystalline size was rarely studied in previous works because in Raman spectroscopy the intensity will be affected by many factors such as the surface roughness, optical alignment, integration time, and excitation level of Raman equipment. Here, we rigorously exclude those possibilities before the further analysis of nanocrystalline formation. The intensity of the incident light is kept the same in all measurements, and the surface is very smooth which has been proved by SEM and AFM studies.

Veprek *et al.*, [100] used a chemical transport method to produce a thin layer of nanocrystalline silicon film, about several micrometers thick, and treated it in different temperatures to form nanocrystals with various sizes. They found the Raman intensity of Si 521  $\text{cm}^{-1}$  peak varied as a parabolic function of grain size in the thin film of nanocrystalline silicon. The maximum intensity appeared at the grain size of 18 nm and then became weaker when the grain size either increased or decreased. X-ray diffraction (XRD) was also employed in their works and it showed a surface model of “amorphous-like” Si in their samples with a 480  $\text{cm}^{-1}$  “shoulder” near 521  $\text{cm}^{-1}$  peak in Raman spectra. This surface model was raised by either stretching or compression of the bond lengths in grain boundaries during nanocrystal formation, and the bonds dilatation would affect the absorption of incident energy and Raman scattering intensity. In nanocrystalline structures, both the optical absorption coefficient and Raman scattering are increased due to bond dilation in grain boundaries, which can cause fluctuating electric charge density and enhance the coupling of the electromagnetic field to the charge-density fluctuation [100]. It was observed in previous work that the absorption of nanocrystalline silicon is much higher than that of single crystalline silicon [101].

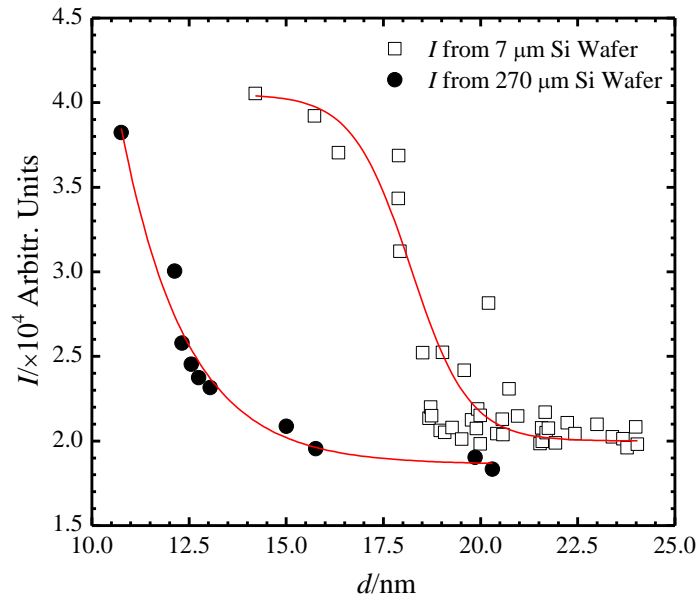


**Figure 4.4.** Relationship between Raman intensity  $I$  and nanocrystalline grain size  $d$  in the 270  $\mu\text{m}$  thick silicon wafer and 7  $\mu\text{m}$  thick silicon wafers.  $I$  is decreasing with the grain size increasing. The solid line is used to guide eyes for the data trend.

Compared with their results, figure 4.4 shows the relationship between crystalline size and Raman intensity of 270  $\mu\text{m}$  thick Si wafer. From the beginning point to the edge on the silicon wafer, the size of nanocrystals declines while Raman intensity increases by 100% because of the increased density of both nanocrystals and grain boundaries. There is a rapid increase around the size of 12 nm, and on the other side of this curve, the intensity is gradually approaching that from single crystal silicon when the grain size increases. We obtain a monotonic decreasing relationship between intensity and grain size. The differences between Veprek's and our work may result from samples' preparing methods. Our sample is formed during mechanical cleaving without heating. Generally, Si breaks easily along its (100) face. Therefore the tensile stress in Si surface next to the broken edge produces nanocrystals which do not have the  $480\text{ cm}^{-1}$  peak. In the past, effort has been taken to relate the Raman peak shape to the grain size as [96, 98]

$$I(\omega) \cong \int \frac{d^3q |C(q_0, q)|^2}{(\omega - \omega(q))^2 + (\Gamma_0/2)^2} \propto \int \frac{d^3q |C(q_0, q)|^2}{(q - q_0)^2 + [1/(2\tau_0)]^2}, \quad (4.1)$$

where  $|C(q_0, q)|^2 \cong e^{-(q-q_0)^2 d^2/4}$  is a Fourier coefficient,  $q_0$  is wave vector of optical phonon,  $|q - q_0| \leq 1/(2d)$ ,  $\omega(q)$  is the phonon dispersion curve,  $\Gamma_0$  is the natural linewidth of Raman active mode  $\Gamma_{25'}$  (521  $\text{cm}^{-1}$  peak) in single crystal silicon, and  $\tau_0$  is the mean free path of the excited optical phonons. Due to the good long range order in single crystal silicon, the restricted  $q$ -selection rule only allows phonons with wave vector  $q_0 = 0$  and gives a narrow peak at 521  $\text{cm}^{-1}$ . However, in nanocrystals, the restriction of  $q$ -selection is relaxed by the smaller crystalline grain size and more phonons are optically allowed in Raman spectrum, so the linewidth of Raman peak of  $\Gamma_{25'}$  mode broadens and peak shift decreases.

#### 4.2.3. Raman imaging for 7 $\mu\text{m}$ thick silicon wafer

The same process is also performed on an ultrathin silicon wafer to compare and confirm our previous study on the thicker silicon. A 7  $\mu\text{m}$  ultrathin silicon wafer is cleaved in the same way as that cleaves the thick Si wafer sample and the edge is used. We scan along a 1  $\mu\text{m}$  long path perpendicular to the edge with a resolution of 20 nm and collect and analyze Raman information. Fitting results of intensity, linewidth, wavenumber shift and crystal size are all shown in Figs. 4.5a - 4.5d. The changing trends of all four properties are similar to those of thick silicon sample. The intensity is gradually enhanced when the tested area is getting closer to the edge and the maximum intensity at the edge is twice of the intensity at the center. The Raman peak intensity variation against the grain size is also plotted in Fig. 4.4.

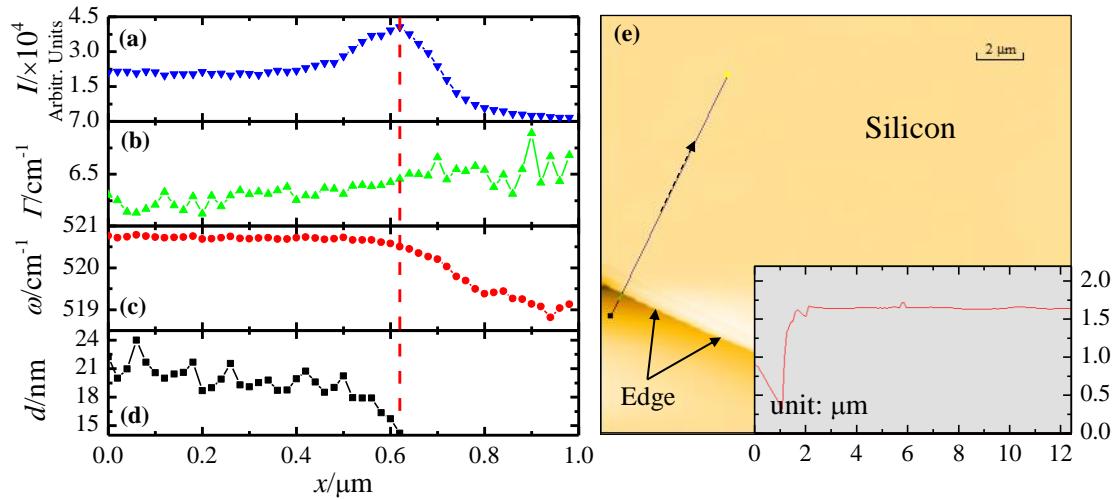


**Figure 4.5.** Raman imaging results from the center to the edge of 7  $\mu\text{m}$  thick silicon wafer. (a) Peak intensity ( $I$ ), (b) width ( $\Gamma$ ), (c) 521  $\text{cm}^{-1}$  peak wavenumber shift ( $\omega$ ), (d) size of nanocrystalline silicon ( $d$ ) change with focal spot from the center to the edge. The red line in this plot shows the actual position of the edge. (e) AFM image of the silicon wafer surface close to Raman testing area. The inset plot is the cross-sectional profile measured along the direction of black dash arrow in the left, and the edge of the wafer is located in the lower left (black area).

Differences exist between this thin Si sample and the previous thicker one. The point where the intensity starts increasing is 200 nm away from the edge and is much smaller than that in the thick Si wafer sample (about 1  $\mu\text{m}$ ), which means the area containing nanocrystals is smaller. Because of the ultrathin thickness, the wafer is easily and quickly broken and so the stress caused by cleaving impacts a smaller region. To evaluate the smooth surface of thin Si wafer near the cleaving edge, AFM study is conducted and the result is shown in Fig. 4.5e. The upper side of this image is silicon wafer and the edge is in the lower left side. The inside plot is the cross sectional profile along the black line in the left and it indicates that the surface of thin Si wafer is smooth at the edge and it will not affect the Raman intensity during testing.

## CHAPTER 5

## TIME-DOMAIN DIFFERENTIAL RAMAN FOR THERMAL PROBING

In this chapter, a brand-new and compelling transient thermal probing and characterization technology is developed based on Raman thermometry and our TET concept: time-domain differential Raman (TD Raman). This new technique overcomes the drawbacks of other techniques listed above and is able to accurately measure the thermal diffusivity of materials. The potential application of this technique is demonstrated by measuring the thermal diffusivity of a microscale Si cantilever. Physical and mathematical models are developed to relate the measured Raman spectrum to the temperature evolution of the sample, and use this information to determine the sample's thermal diffusivity.

## 5.1. Time-domain differential Raman: physics and experimental setup

**5.1.1. Concept and physics of TD Raman**

To achieve well-defined heating and transient thermal probing, a modulated single laser beam is used for both material heating and Raman excitation/thermal probing. Figure 5.1a shows the concept of the technique. In Case 1, the modulated laser cycle is designed to consist of an excitation period ( $t_e$ ) followed by a thermal relaxation period ( $t_r$ ). During the excitation period, the temperature of the sample starts to rise when the laser is on, and keeps increasing until the pulse ends. Raman scattering is also excited and collected during this period. Along with the rising temperature, the instant Raman spectrum varies: the Raman peak intensity ( $I$ ) decreases, the wavenumber ( $\omega$ ) softens and the linewidth ( $\Gamma$ ) broadens. The schematic of Raman spectrum's properties variations is shown in Case 1 in Fig. 5.1a. During the relaxation period the laser is

switched off and the sample will cool down due to thermal dissipation to the heat sink or supporting structure. As the laser is off, neither is Raman scattering excited nor collected in this period. The thermal relaxation period  $t_r$  is long enough to allow the sample to completely cool down before the next excitation cycle starts. In one entire cycle, the excited Raman scattering signals are collected and accumulated over the whole excitation period  $t_e$ . Since one single heating period is too short for Raman signal collection, multiple heating/cooling cycles are used in spectrum acquisition to ensure a sufficiently high Raman peak. Based on the number of heating/probing cycles in the measurement, the Raman signal of a single heating period can be simply obtained. The Raman spectrum in Fig. 5.1b shows the temporally accumulative Raman spectrum for this case.

After the first heating and thermal probing case is studied, we design a second modulated laser heating/probing case (Case 2). As illustrated in Fig. 5.1a, the excitation period is a little longer than Case 1 by  $\Delta t_e$ , but the relaxation period is the same as Case 1. Thus, the entire cycle is also extended by  $\Delta t_e$  while the frequency is decreased. The temperature increases further in the extended heating time ( $\Delta t_e$ ), and the instantaneous  $I$ ,  $\omega$ , and  $\Gamma$  vary with increasing temperature than at the end of the laser pulse in Case 1.

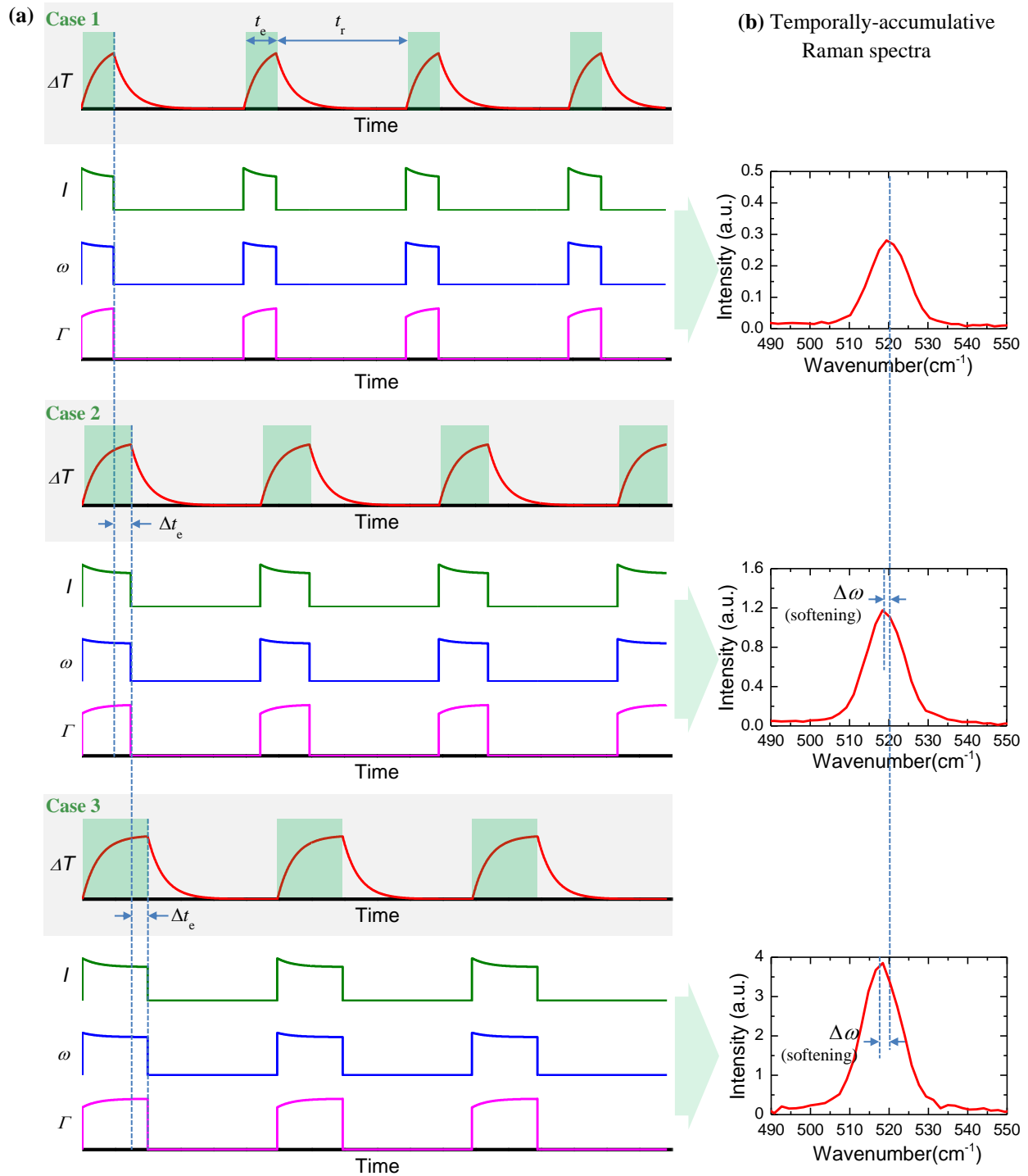


**Figure 5.1.** (a) Timing profiles of the laser pulse and the temperature evolution, and instant changes of Raman peak intensity ( $I$ ), peak shift ( $\omega$ ) and linewidth ( $\Gamma$ ). Along with the heating, the temperature in the sample increases, and then the Raman peak intensity decreases, the wavenumber softens and linewidth broadens. In TD Raman, the laser heating time is increased a little bit ( $\Delta t_e$ ) each time from Case 1 to Case 3. Therefore, the temperature of the heated region will experience more increase (before reaching the steady state) from Case 1 to Case 3. This

extended temperature rise will give rise to a slight change in the Raman spectrum collected during the heating period. (b) The corresponding temporally accumulative Raman spectra of one cycle in three cases. Slight Raman peak softening due to the increased differential heating time is marked in the figure. The peak intensity increases largely because of the longer excitation period. The heating induced intensity decrease is less obvious in these spectra, but is visible via further peak analysis.

The collected temporally accumulative Raman spectrum (shown on the right in Fig. 5.1b) will differ from the Raman spectrum of Case 1 because of  $\Delta t_e$ . First, it will have a higher intensity due to the increased excitation time, because more scattered photons are sent to the spectrometer during this period. However, this intensity differential is not proportional to  $\Delta t_e$ . As shown in Fig. 5.1a, since the excitation time is longer, the sample will have a greater temperature rise (if the steady state is not reached yet), resulting in a small reduction in the intensity increase. Second, since the collected Raman spectrum reflects the temperature information in the entire excitation cycle, the Raman spectrum with an extended excitation time will have Raman peak position softening due to the further temperature increase during  $\Delta t_e$ . In Fig. 5.1b, this slight wavenumber softening is marked. Finally, the Raman spectrum in the new excitation case should have a broadened linewidth, since the sample has a higher average temperature during the excitation than in Case 1.

After the second excitation/probing case study is done, the excitation time of the laser is extended again while the thermal relaxation time is kept the same (Case 3). The instantaneous  $\Delta T$ ,  $I$ ,  $\omega$ , and  $\Gamma$  are shown in Case 3 in Fig. 5.1a. The variations of  $\Delta T$ ,  $I$ ,  $\omega$ , and  $\Gamma$  are even smaller than those in Case 2. The frequency will then be even shorter. The sample is heated, and the accumulated Raman spectrum is collected to reflect the temperature history over the excitation period. As we can see, with the increase of the excitation period by  $\Delta t_e$  in each case, the

corresponding Raman spectrum will have a small change (differential). Such change is related to the temperature rise of the sample induced by  $\Delta t_e$ . This information can be used with further physical data handling to capture the realistic temperature evolution of the sample and to determine the thermal diffusivity of the sample.

It is better to construct a physical model for describing the normalized temperature evolution in a specific sample. Differing from other studies, the measured wavenumber, linewidth, and intensity in our work reflect an accumulative quantity of temperature variation during the pulse domain, but are not the time average. Variations in wavenumber, linewidth, and intensity against  $t_e$  are complexly related to the temperature increase. Rather, a precise physical model is needed to extract the temperature variation. With the correlation between variations of the Raman spectra and the normalized temperature rise, we can fit the normalized change of some parameters of the Raman peak to determine the sample's thermal diffusivity.

### 5.1.2. Experiment design

The TD Raman idea is realized by integrating a square-wave-modulated diode laser into a commercial confocal Raman spectrometer. A continuous wave single longitudinal mode laser (MSL-III-532-AOM-150mW, Ultralaser, Inc.) is modulated with a function generator (DS345) to output variable duty cycle pulses. The laser is reflected by several mirrors to be integrated into the original optical path of a commercial confocal Raman system (Voyage, B&W Tek, Inc. and Olympus BX51). This laser is then focused on the sample surface with an objective lens and acts as both the heating and Raman excitation source. When the pulse is on, the laser heats the sample and induces a temperature rise of the sample surface. The Raman scattering signal collected

simultaneously during this period contains temperature and thermal stress information. It is collected by the same objective lens in back scattering mode and sent to the Raman spectrometer. A beam splitter and a notch filter are placed in front of the spectrometer to filter out the reflected excitation light. Acquisition of the Raman spectrum is accomplished by using commercial software in a computer.

### 5.2. Si cantilever measurement: Raman spectrum variation against $t_e$

A carefully designed experiment for time-domain thermal probing and thermal characterization is conducted on a tipless silicon AFM cantilever (AppNano, Ltd.) in the open air at room temperature (293 K). The optical image of the tipless cantilever (Fig. 5.2a) shows that the tip is about 450.35  $\mu\text{m}$  long, 49  $\mu\text{m}$  wide and 2.5  $\mu\text{m}$  thick. The tip end is a triangle with a height of 22.95  $\mu\text{m}$ . The laser is focused on the tip end of the cantilever with a 4 $\times$  objective lens. The laser spot size is 31.4 $\times$ 65.3  $\mu\text{m}^2$  at the focal level. The long axis of the laser spot is perpendicular to the cantilever and the short axis is parallel to it in the horizontal plane (Fig. 5.2b). 7.9 mW laser energy is carefully selected to heat the cantilever, while the range of the temperature rise is still small enough that the Raman spectrum parameters are considered linearly correlated with temperature rise. Also, the small thermal energy input would not induce damage on the cantilever. It is proved by a repeated measurement on the same irradiated spot that no obvious change in the spectrum was observed. To simplify the evaluation of the temperature-induced change of Raman signals, an approximation of a square tip end is applied to our physical model as shown in Fig. 5.2b. The total length  $L$  used in the physical model is 438.9  $\mu\text{m}$  and the length of irradiation area  $l_e$  is 19.9  $\mu\text{m}$ .

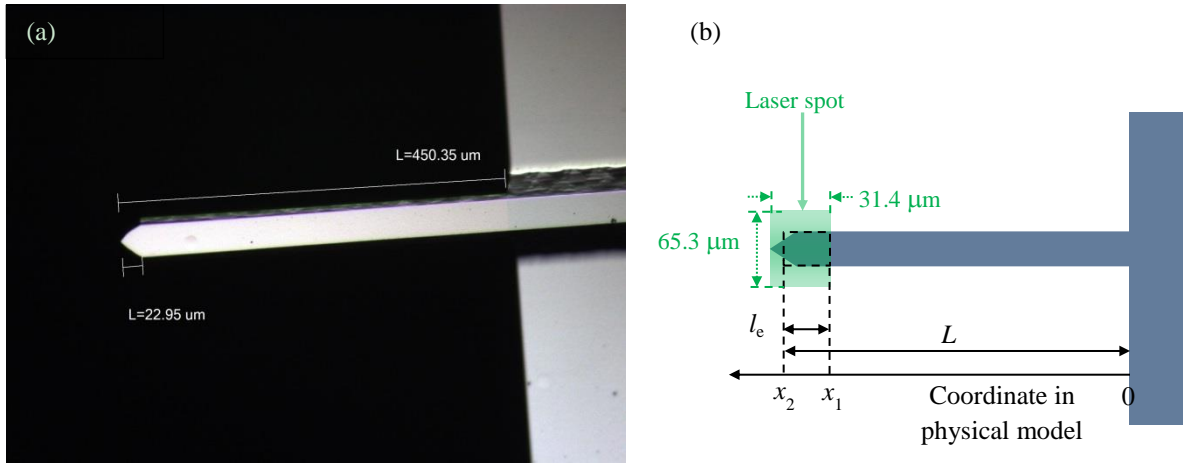


**Figure 5.2.** (a) The optical microscope view of the tipless Si cantilever. It is  $450.35 \mu\text{m}$  long and  $49 \mu\text{m}$  wide. The tip has a height of  $22.95 \mu\text{m}$ . (b) Schematic of laser spot position on the cantilever tip. The effective heating region is marked with  $x_1$  and  $x_2$  on the  $x$  coordinate in the physical model.  $l_e (= x_2 - x_1)$  is  $19.9 \mu\text{m}$  indicating the effective length of the heating region on the cantilever.  $L$  is the total effective length ( $438.9 \mu\text{m}$ ) used for the cantilever in the physical model.

The characteristic heat transfer time of this cantilever in the length direction is estimated as  $0.81L^2/\alpha$  [75]. With bulk Si's reference thermal diffusivity  $\alpha$  of  $8.92 \times 10^{-5} \text{ m}^2/\text{s}$  at 300 K [80], this characteristic time is around 1.75 ms. The relaxation time ( $t_r$ ) is fixed as 10 ms during which the cantilever can definitely relax to the room temperature and the cumulative thermal effect in the cantilever can be completely eliminated. Meanwhile, the length of the excitation period is adjusted from 20  $\mu\text{s}$  to 30 ms to cover the whole transient range of temperature rise from room temperature to the steady state temperature. The increment of  $t_e$  in experiment is varied in order to best reflect the change of the Raman spectrum against the heating time. The integration time for an individual spectrum is also selected to cover many pulse cycles and obtain a strong Raman signal for analysis. Differences in collecting cycles and time will be normalized later in the data processing.

Eight selected experimental Raman spectra of the Si peak are normalized to represent the signal for one excitation cycle (Fig. 5.3a). With increased excitation time, the Si Raman peak shifts to a smaller wavenumber (softening) and broadens a little bit. This is due to an increase in temperature with increasing  $t_e$ . Also with increased  $t_e$ , the Raman intensity becomes larger because the excitation time is longer. Figures 5.3b - 5.3d show variations of both the peak intensity ( $E_\omega$ ) and the time-averaged one ( $E_\omega^* = E_\omega/t_e$ ), linewidth ( $\Gamma$ ), and wavenumber ( $\omega$ ) against the excitation time. The subscript “ $\omega$ ” means that the maximum intensity is from the peak center wavenumber  $\omega$ , which softens along with the increase of the heating time. For the Raman peak intensity,  $E_\omega$  increases with increased  $t_e$ , since when  $t_e$  is longer, the Raman excitation is longer and a stronger signal is expected. Theoretically, if there is no temperature rise (heating), the Raman peak intensity should increase linearly with  $t_e$ . However, as seen in Fig. 5.3b, in the beginning, the Raman intensity increases fast. This rate slows down and finally reaches a relatively constant rate (slope). The observed decrease in  $\partial E_\omega / \partial t_e$  is related to the laser heating time and temperature rise. Our recent studies show that when the temperature increases, the Raman intensity will decrease [69-71]. When  $t_e$  gets longer, the cantilever will reach the steady state (no further increase in the temperature), and the Raman intensity will increase with  $t_e$  linearly. The normalized Raman peak intensity  $E_\omega^*$  is calculated as  $E_\omega/t_e$ . It eliminates the effect of varied  $t_e$  and shows a decreasing trend against the excitation time. The decreasing rate is fast at the beginning while the average temperature rises more quickly. As the cantilever is approaching the steady state (longer  $t_e$ ), the average temperature rise gradually becomes a constant and so as  $E_\omega^*$ .

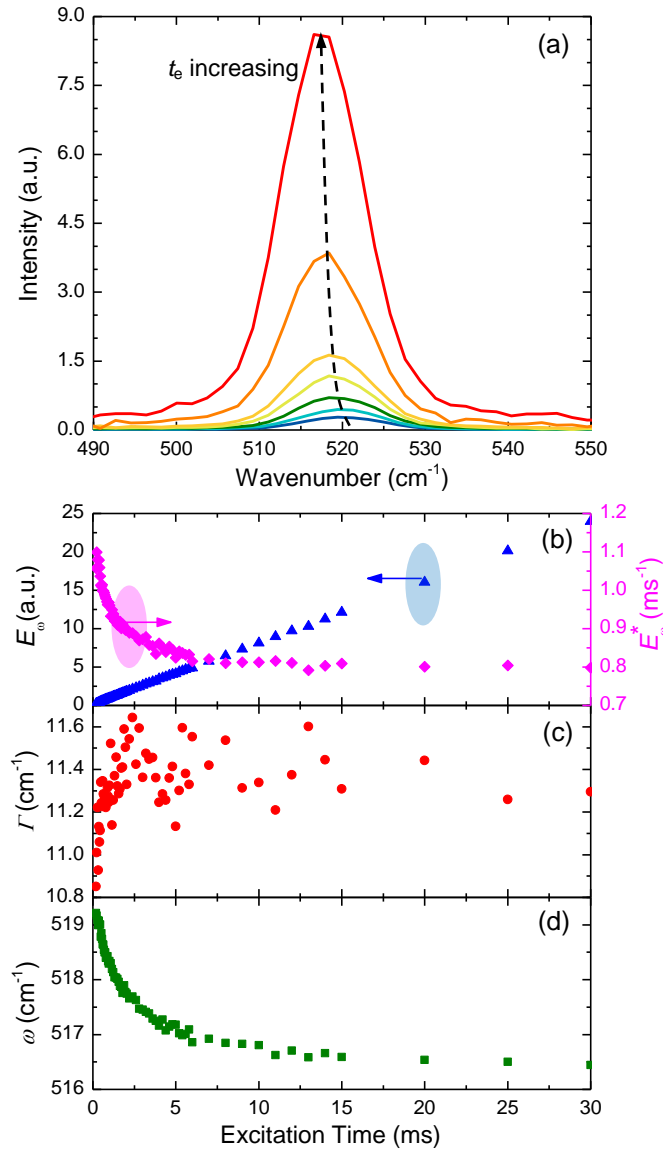


**Figure 5.3.** The evolution of the Si Raman peak against the increase of excitation/heating duty in the experiment. (a) Spectra per cycle under different excitation time of  $t_e$ : — 0.24 ms, — 0.4 ms, — 0.68 ms, — 1.16 ms, — 1.72 ms, — 4.2 ms, and — 10 ms. As the excitation/heating time becomes longer, the Raman peak in one cycle increases and softens to the left. (b) Raman emission  $E_\omega$  ( $\blacktriangle$  to the left y axis) increase against  $t_e$ , but the rate  $\partial E_\omega / \partial t_e$  declines quickly at the beginning and then slows down to a constant. The normalized Raman emission  $E_\omega^*$  ( $\blacklozenge$  to the right y axis) decreases to a steady state value as  $t_e$  become longer.  $E_\omega^*$  directly illustrates that the Raman emission per unit time decreases against the heating time. (c) Raman linewidth variation against the excitation time. Although an increasing trend is observed for the linewidth against increased excitation time, large noises are observed in linewidth data due to the less sensitivity of linewidth to temperature variation. So this data is less applicable for thermal diffusivity determination. (d) A clear decline in the wavenumber against  $t_e$  makes wavenumber  $\omega$  a good parameter for determining  $\alpha$  of the cantilever.

For the linewidth (Fig. 5.3c), although an increasing trend is observed against increased excitation time, the signal to noise ratio (SNR) is small due to the small variation of linewidth with temperature. For the wavenumber (Fig. 5.3d), it experiences quick decay because of the fast temperature increase at the beginning of the laser heating. During this period, the increasing rate of temperature is mainly determined by the heating rate since the heat conduction is weak. Along with the heating (longer  $t_e$ ), thermal transport to the heat sink (the chip) becomes more important while the laser heating rate remains the same. Thus the heat dissipation slows down the rate of the temperature rise in the sample. As a result, the wavenumber changes slower at the longer  $t_e$  than it did around the beginning. The wavenumber shown in Fig. 5.3d is Raman intensity weighted over the time:  $0 \sim t_e$ . Therefore its rate of change against  $t_e$  is slower than the real temperature changing rate. These changes are tightly associated with the temperature rise in the cantilever.

As we stated above, the measured Raman peak intensity, linewidth, and wavenumber is an intensity-weighted average over  $0 \sim t_e$ , and could not reflect the instantaneous temperature variation against time. To utilize the Raman spectrum to determine the thermal diffusivity, physical model development is necessary to describe the temperature evolution of the laser heated region, to relate the measured Raman spectrum to the temperature evolution with consideration of temperature dependent Raman intensity, and to fit the reduced Raman spectrum variation against  $t_e$ .

### 5.3. Physical model for temperature evolution

The characteristic thermal diffusion time of a material is proportional to  $l^2$ , where  $l$  is the thermal diffusion length. The cantilever is 2.5  $\mu\text{m}$  thick and 450.35  $\mu\text{m}$  long. The characteristic thermal diffusion time in the thickness direction ( $\tau_1$ ) of the cantilever is negligible in comparison with the time ( $\tau_2$ ) taken by the whole cantilever to reach the thermal steady state ( $\tau_1 \sim 3 \times 10^{-5} \tau_2$ ) in the length direction. Although the cantilever is heated at the end from the top surface, it is physically reasonable to assume that the temperature uniformly distributes across the cross-section. This 1D approximation (along the length direction) is applicable for evaluating the heat transport from the tip of the cantilever to the chip. Neglecting radiation and convection effect (discussed later), the heat transport in the cantilever along the length direction can be expressed as:

$$\rho c_p \frac{\partial \theta}{\partial t} = k \frac{\partial^2 \theta}{\partial x^2} + \dot{g}, \quad (5.1)$$

where  $\dot{g}$  is the heating induced by the laser pulse at the tip end. The  $x$  coordinate is shown in Fig. 5.2b.  $\rho$ ,  $c_p$ , and  $k$  are the density, specific heat, and thermal conductivity, respectively. Adiabatic boundary condition is imposed on the tip end, and the other end is treated as a big heat sink with a constant temperature of 293 K.  $\theta$  is the temperature rise under the pulsed laser heating. At the beginning,  $\theta$  is 0 K in the whole cantilever. The Green's function method is employed to solve Eq. 5.1:

$$G_{x11}(x, t | x', \tau) = \frac{2}{L} \sum_{m=1}^{\infty} e^{-m^2 \pi^2 \alpha (t-\tau)/L^2} \times \sin(m\pi \frac{x}{L}) \sin(m\pi \frac{x'}{L}), \quad (5.2)$$

$\alpha = k/\rho c_p$  is thermal diffusivity. The temperature rise has the expression of:

$$\theta(x, t) = \frac{\alpha}{k} \int_{\tau=0}^t \int_{x'=x_1}^{2L-x_1} G_{x11}(x, t | x', \tau) \dot{g} dx' d\tau. \quad (5.3)$$

Since the excited Raman signals are collected at the tip end, a spatially averaged temperature in the heated region is used to describe the temperature evolution probed by the Raman spectrum. This is physically reasonable since the heated region is very small, and the temperature distribution over it is very uniform. In the 1D model,  $x_1 = 427.4 \mu\text{m}$  and  $x_2 = 2L - x_1$  are the coordinates of the effective heated region on the tip surface. The origin is located at the conjunction point of the cantilever and the chip shown in Fig. 5.2b. The solution for the spatially averaged temperature rise at one instant is:

$$\bar{\theta}(t) = \frac{8\dot{g}L^3}{(L-x_1)k} \sum_{m=1}^{\infty} \frac{1}{m^4\pi^4} (1 - e^{-\frac{m^2\pi^2\alpha}{4L^2}t}) \left[ \cos \frac{m\pi}{2L} x_1 - \cos \frac{m\pi}{2L} (2L-x_1) \right]^2. \quad (5.4)$$

At the steady state ( $t \rightarrow \infty$ ), the final temperature rise  $\bar{\theta}_{ss}$  has the expression of

$$\bar{\theta}_{ss} = \frac{8\dot{g}L^3}{(L-x_1)k} \sum_{m=1}^{\infty} \frac{1}{m^4\pi^4} \left[ \cos \frac{m\pi}{2L} x_1 - \cos \frac{m\pi}{2L} (2L-x_1) \right]^2. \quad (5.5)$$

The normalized temperature rise  $\bar{\theta}^*$  with respect to  $\bar{\theta}_{ss}$  is

$$\bar{\theta}^* = \bar{\theta} / \bar{\theta}_{ss} = \frac{\sum_{m=1}^{\infty} \frac{1}{m^4\pi^4} (1 - e^{-\frac{m^2\pi^2\alpha}{4L^2}t}) \left[ \cos \frac{m\pi}{2L} x_1 - \cos \frac{m\pi}{2L} (L-x_1) \right]^2}{\sum_{m=1}^{\infty} \frac{1}{m^4\pi^4} \left[ \cos \frac{m\pi}{2L} x_1 - \cos \frac{m\pi}{2L} (L-x_1) \right]^2}. \quad (5.6)$$

Considering the linear correlations between temperature rise and variations in Raman peak intensity, wavenumber and linewidth in a small range of temperature variation, the change of the Raman spectrum in the experiment can be evaluated by considering the evolution of  $\bar{\theta}^*$ .

#### 5.4. Physical model and numerical reconstruction of Raman spectrum

At any instant  $t$  during the excitation cycle,  $0 \sim t_e$ , the Raman signal emitting rate can be expressed as [assuming the Raman peak takes the Gaussian distribution, which usually holds up]

$$I(\omega) = A_t \exp\left[-\frac{4 \ln 2 \cdot (\omega - \omega_t)^2}{\Gamma_t^2}\right]. \quad (5.7)$$

$I(\omega)$  is the Raman emission rate at frequency  $\omega$ , and  $A_t$  is the rate at the Raman peak location  $\omega_t$ .  $\Gamma_t$  is the Raman linewidth. Note that  $A_t$ ,  $\omega_t$  and  $\Gamma_t$  all depend on temperature, so they change with time  $t$  during the excitation cycle because temperature changes with  $t$ . The calibration in previous works [69-71] reveals the linear temperature-dependent feature of Si Raman peak properties over a temperature range from 20 to 200 °C. Thus, in this work, this feature can be expressed as  $A_t = A_0(1 - A\bar{\theta}^*)$ ,  $\omega_t = \omega_0 - B\bar{\theta}^*$ , and  $\Gamma_t = \Gamma_0 + C\bar{\theta}^*$ , where  $A_0$ ,  $\omega_0$ ,  $\Gamma_0$  are the corresponding Raman properties at the beginning of laser heating (no temperature rise yet). Constants  $A$ ,  $B$ , and  $C$  are the changing rate of the Raman intensity, peak location, and linewidth against the normalized temperature. The accumulative Raman emission (at wavenumber  $\omega$ ) for the entire excitation cycle from 0 to  $t_e$  can be obtained by integrating  $I(\omega)$  over time as

$$E_\omega(\omega, t_e) = A_0 \int_0^{t_e} (1 - A\bar{\theta}^*) \exp\left[-\frac{4 \ln 2 \cdot (\omega - \omega_0 + B\bar{\theta}^*)^2}{(\Gamma_0 + C\bar{\theta}^*)^2}\right] dt. \quad (5.8)$$

In Eq. 5.6, the variable  $t$  and the parameter  $\alpha$  can be grouped together as the Fourier number  $Fo$  ( $Fo = \alpha t/L^2$ ). Thus, from Eqs. 5.6 and 5.8, we can tell that both temperature rise and Raman intensity depend on  $Fo$ . Substituting  $Fo$  into Eq. 5.8, the correlation between the excitation time and Raman spectrum has the expression of

$$E_\omega(\omega, Fo_e) = A_0 \int_0^{Fo_e} (1 - A\bar{\theta}^*) \exp\left[-\frac{4 \ln 2 \cdot (\omega - \omega_0 + B\bar{\theta}^*)^2}{(\Gamma_0 + C\bar{\theta}^*)^2}\right] dFo, \quad (5.9)$$

where  $Fo_e = \alpha t_e/L^2$ . For the Raman peak intensity variation against  $t_e$  as shown in Fig. 5.3b, its increase against the excitation time carries the integration time's effect. Instead of using the

cumulative Raman emission for the entire excitation cycle, we use the time average for analysis. This is done by simply dividing the left term in Eq. 5.9 by  $Fo_e$ . The expression of this normalized intensity is

$$E_{\omega}^*(\omega, Fo_e) = \frac{A_0}{Fo_e} \int_0^{Fo_e} (1 - A\bar{\theta}^*) \exp \left[ -\frac{4 \ln 2 \cdot (\omega - \omega_0 + B\bar{\theta}^*)^2}{(\Gamma_0 + C\bar{\theta}^*)} \right] dFo, \quad (5.10)$$

where  $E_{\omega}^*(\omega, Fo_e) = E_{\omega}(\omega, Fo_e)/Fo_e$ . The values of constants  $A_0$ ,  $\omega_0$ ,  $\Gamma_0$ ,  $A$ ,  $B$ , and  $C$  in Eq. 5.10, can be extracted from the normalized peak intensity, wavenumber, and linewidth variation against  $t_e$  (shown in Fig. 5.3) by evaluating the limit at  $t_e \rightarrow 0$  and  $t_e \rightarrow \infty$ . However, because even the Raman spectrum with the shortest  $t_e$  inevitably has some heating effect, the extracted thermal properties and Raman scaling constants will deviate from the actual values. Thus, these constants are then refined to better approach the actual values which are then used for fitting experimental data. The refining process will be detailed in Section 5.5. They are finally determined as  $A = 0.31$ ,  $\omega_0 = 520.22 \text{ cm}^{-1}$ ,  $B = 3.7 \text{ cm}^{-1}$ ,  $\Gamma_0 = 11.06 \text{ cm}^{-1}$ , and  $C = 0.34 \text{ cm}^{-1}$ . Constant  $A_0$  is less important to us for we are only interested in the relative Raman intensity variation.

Based on Eq. 5.9, the reconstructed Raman spectrum per cycle at different  $Fo_e$  is shown in Fig. 5.4a. It is observed when  $Fo_e$  increases, the Raman peak shifts to the left (softening), the linewidth slightly broadens, and the Raman peak intensity increases largely as the excitation/collecting time becomes longer. Figures 5.4b and 5.4c show how the normalized Raman intensity and wavenumber vary with  $Fo_e$ . The normalized Raman intensity  $E_{\omega}^*$  decreases with increased  $Fo_e$ . This is because when  $Fo_e$  is larger, the average temperature of the sample during that period is higher. As a result, the average Raman signal becomes smaller. Also we fit

the reconstructed Raman peaks and determine their peak intensity and peak location at different  $Fo_e$ . The reconstructed  $E_\omega^*$  and  $\omega$  show the similar trends as the experimental results shown in Figs. 5.3b (the right y axis) and 5.3d. However, how fast or slow they change with time is dependent on the thermal diffusivity of the sample.  $Fo_e$  here only gives a non-dimensionalized time.

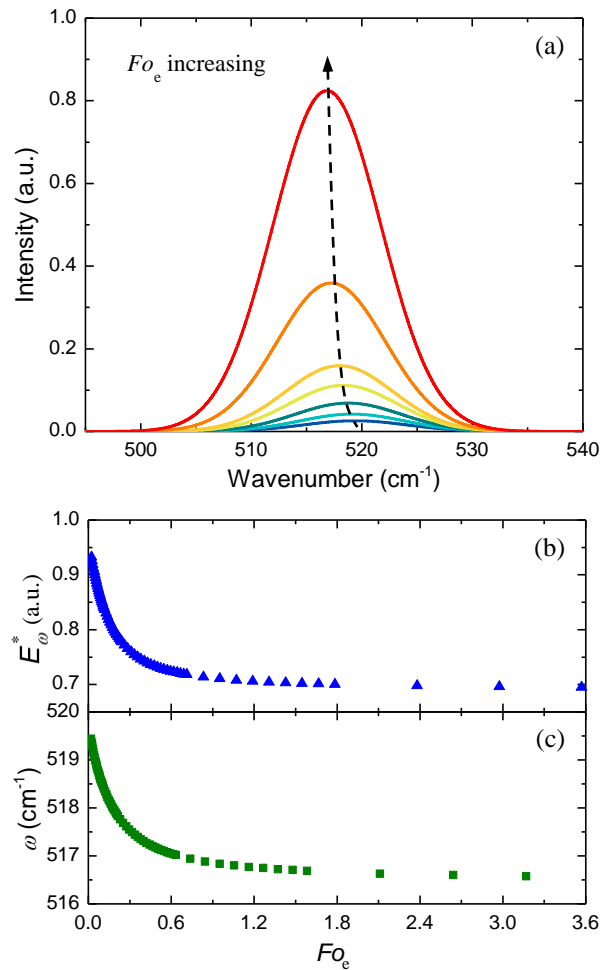


**Figure 5.4.** (a) The evolution of the reconstructed Si Raman spectrum per cycle with the numerical method against the increase of Fourier number  $Fo_e$  ( $t_e$ ): — 0.028, — 0.047, — 0.079, — 0.14, — 0.20, — 0.49, and — 1.17. The Raman peak in one cycle increases and softens to the left against the increased  $Fo_e$ . This echoes the one in Fig. 5.3a. (b) The decreasing trends of the normalized Raman intensity  $E_\omega^*$  and (c) the Raman shift  $\omega$  against the Fourier number  $Fo_e$  well agree with the trends in the experiment.

### 5.5. Thermal diffusivity determination based on $\omega$ and $E^*$

Although the Raman linewidth is directly related to temperature, the SNR for the linewidth measurement is too small to precisely determine the thermal diffusivity of the Si cantilever. Instead, we use the variations of the normalized Raman intensity and peak shift for thermal diffusivity determination. In the fitting process, the initial values of constants  $A_0$ ,  $\omega_0$ ,  $\Gamma_0$ ,  $A$ ,  $B$ , and  $C$  are directly read from the experimental data and substituted into Eq. 5.10. As mentioned above, some heating effect inevitably exists in the initial state of the experiment as we cannot make  $t_e$  extremely short while collecting a sufficient Raman signal. The extracted initial values of those constants from Fig. 5.3b will deviate from their real values. Fine adjustment of them is then performed in determining the cantilever's thermal diffusivity. If an extremely short  $t_e$  could be realized, the heating effect could be safely neglected and the  $A$ ,  $B$ , and  $\omega_0$  can thus be directly measured. The improvement of TD Raman technology with respect to shorten the excitation time will be pursued in near future.

In the fitting process,  $\omega_0$ ,  $A$  and  $B$  are scanned over a specified reasonable range. For each combination of  $\omega_0$ ,  $A$  and  $B$ , based on Eq. 5.10, we reconstruct the Raman spectrum at different  $Fo_e$ , and obtain curves like those shown in Figs. 5.4b and 5.4c. Note these curves do not have the time information yet. For each thermal diffusivity, the  $Fo_e$  can be converted to time, and the curves become time-related. Then these curves are compared with those experimental data in Figs. 5.3b and 5.3d using the least square method and obtain a deviation ( $\sigma$ : root mean square of differences) at the end of the comparison.  $A_0$  is not needed as we are only interested in the relative Raman intensity variation. Then we scan the thermal diffusivity from  $5.05 \times 10^{-5} \text{ m}^2/\text{s}$  to  $12 \times 10^{-5} \text{ m}^2/\text{s}$  with an increment of 1% each step. The whole fitting process is run to find the

smallest  $\sigma$  and returns the corresponding  $\omega_0$ ,  $A$ ,  $B$ , and  $\alpha$ . Refining is also conducted on  $\Gamma_0$  and  $C$ , but it is observed that the extracted  $\Gamma_0$  and  $C$  is very close to their initial values due to temperature sensitivities. Thus their initial values read from Fig. 5.3b are directly used in the entire fitting process. The thermal diffusivity giving the best fit of the experimental data is taken as the property of the sample. The experimental data and best fitted curves for the normalized intensity and the wavenumber based on the Eq. 5.10 are shown in Figs. 5.5a and 5.5b.

The normalized intensity decreases against the excitation time to the steady value. The best fitted curve with an  $\alpha_{E_o^*}$  of  $9.17 \times 10^{-5} \text{ m}^2/\text{s}$  follows the trend of the normalized intensity in the experiment well. The uncertainty of the normalized intensity in the peak analysis is indicated by the error bars in Fig. 5.5a. To illustrate the sensitivity of the normalized Raman intensity method, two curves of  $\pm 10\%$  variations in  $\alpha_{E_o^*}$  are plotted in blue and green in Fig. 5.5a. Across the whole  $t_e$  span, a visible change is observed for these two curves compared with the best fitting results, indicating this method is sensitive to determine thermal diffusivity. Though these two curves of  $\pm 10\%$  variations in  $\alpha_{E_o^*}$  could not cover all the measurement errors, they best limit the changing trend of the fitted curve to well follow the experiment result. The accurate changing trend is more important in our fitting process. The most experimental data fall in between the  $\pm 10\%$  curves even though the error level is much broader. Figure 5.5b shows the change in wavenumber shift against  $t_e$  and error bars show the wave number uncertainty in peak fitting. The curve with an  $\alpha_o$  of  $8.14 \times 10^{-5} \text{ m}^2/\text{s}$  gives the best fit (red), and the other two curves, varying 10% in  $\alpha_o$ , are plotted for showing the sensitivity of the wavenumber fitting method.

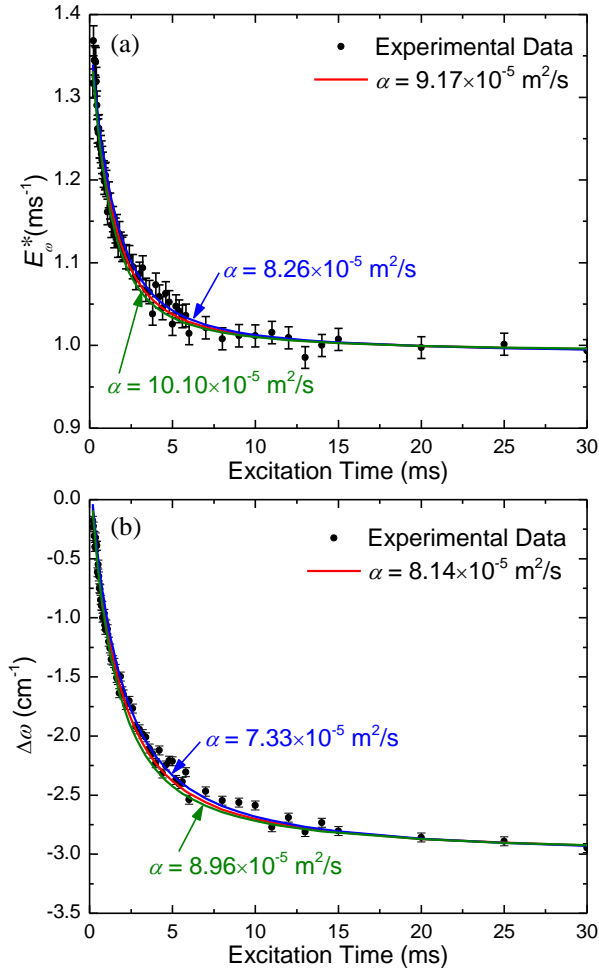


**Figure 5.5.** (a) Variation of normalized intensity against the excitation time. It decreases as  $t_e$  is increasing to a steady state value. The red curve with  $\alpha_{E^*}$  of  $9.17 \times 10^{-5} \text{ m}^2/\text{s}$  best fits the experimental data based on the intensity method. (b) Wavenumber shift to the steady state against the excitation time. The best fitted curve with  $\alpha_{\omega}$  of  $8.14 \times 10^{-5} \text{ m}^2/\text{s}$  is shown red. Error bars in both figures show the uncertainty in the measurement, and curves with 10% deviation in both thermal diffusivities are shown in blue and green. They show obvious difference from the best fitted results indicating the sensitivity of the normalized Raman intensity method and wavenumber shift method, respectively.

### 5.6. Physical analysis and experimental uncertainty evaluation

To evaluate the measured thermal diffusivity, we first estimate the temperature rise in the Si cantilever's tip end with the physical mode shown in Fig. 5.2b. The final temperature rise  $\Delta T$  in the irradiated area can be calculated with the equation  $q = kA_{\text{cross}} \Delta T_{\text{ss,tip}} / L$ .  $q$  is the absorbed

laser power which is the product of the incident laser power on the surface of the tip end and the absorbance of single crystal Si (0.626 at 532 nm).  $k$  is the thermal conductivity of bulk Si (148 W/m K) at 300 K, and  $A_{\text{cross}}$  is the cross-section area of the cantilever. The steady state temperature rise ( $\Delta T_{\text{ss,tip}}$ ) is determined to be 57 K at the tip end of the Si cantilever. The thermal diffusivity  $\alpha$  in the physical model in Eq. 5.4 reflects a spatial-average value for describing the temperature evolution in the whole cantilever. The temperature linearly decreases from the tip end to the chip, so the spatial-average temperature is the half of  $\Delta T_{\text{ss,tip}}$  at the steady state.

As discussed in Sec. 5.2, time averaging is performed in constructing the correlation between the temperature rise and the peak profile. Actually, the obtained raw Si Raman peak is an accumulated signal over the excitation period. The normalization of the intensity excludes the varied excitation time averages the peak profile. The thermal diffusivity determined by the physical model fitting contains another average in the time domain. For  $\Delta T_{\text{ss,tip}}/2$  is a sound approximate of the spatial-average temperature rise at the steady state, the final average temperature rise that determines the fitted thermal diffusivity in the cantilever is about  $\Delta T_{\text{ss,tip}}/4$ . This characteristic temperature rise is about 14 K. Our TD Raman experiment is carried out at room temperature (293 K), so the spatially-and-timely-averaged temperature of the Si cantilever is 307 K. The corresponding reference thermal diffusivity  $\alpha_{\text{ref}}$  of single crystal silicon is  $8.66 \times 10^{-5} \text{ m}^2/\text{s}$  at this temperature. In fact, considering the thickness of the cantilever, the temperature distribution could be uneven from the upper part to the bottom of the cantilever. The real average temperature rise will be even lower than 14 K and then the thermal diffusivity will be a little larger than  $8.66 \times 10^{-5} \text{ m}^2/\text{s}$ .

Due to the extremely small size and the delicate feature of the cantilever, a regular thermocouple could not be applied for real-temperature measurement. To compare with the above analysis, the temperature rise is also examined from the experimental variations in linewidth, normalized intensity, and wavenumber of the Si Raman peak. Among them, the temperature change based on linewidth is the most straightforward to analyze. However the small SNR associated with the linewidth measurement makes it difficult for accurate fitting. The linewidth of the Si peak increases by about  $0.34 \text{ cm}^{-1}$  in Fig. 5.3c from the initial state to the steady state in the experiment. So the total temperature rise at the cantilever end is 38 K and the average temperature ( $\bar{\theta}_r$ ) is 9.5 K with the temperature coefficient of  $0.009 \text{ cm}^{-1}/\text{K}$  calibrated in our previous work [70]. It is a little lower than, but very close to  $\bar{\theta}_{th}$ . The Si Raman spectrum with the shortest excitation period is taken as the initial state to evaluate the temperature rise. This experimental initial state still has some temperature rise, while the real initial state should be extracted from the Si Raman peak without heating effect. Thus, the linewidth of the real initial state should be narrower. It is reasonable that  $\bar{\theta}_r$  is a little lower than  $\bar{\theta}_{th}$ .

In the intensity method, we use the ratio of normalized intensity at the steady state to the initial state to estimate the total temperature rise. This ratio is 74.6% from Fig. 5.5a and the determined temperature is about 108.8 K based on the temperature coefficient of  $0.0024 \text{ K}^{-1}$  [70]. Analogous to  $\bar{\theta}_r$ , averaged temperature  $\bar{\theta}_{E_o^*}$  will be 27.2 K, which is higher than  $\bar{\theta}_{th}$ . Several factors could account for this deviation. One is the unevenly distributed temperature-induced thermal stress in the cantilever. This thermal stress is high in the upper irradiated area of the cantilever. The cantilever's deflection is the factor resulting from the uneven thermal stress and expansion. It will cause an out-of-focus effect during Raman spectra acquisition, though the

deflection is invisible to naked eyes under the  $4\times$  objective lens. These thermal stress induced effects will lead to the reduction in the Si Raman intensity at the steady state and increase  $\bar{\theta}_{E_{\omega}^*}$ .

Another possible reason is the inaccuracy of the initial state value in the experiment. On one hand, large noises are observed at the beginning of the experimental data in Fig. 5.5a, which will obscure the real initial intensity. On the other hand, when the excitation period is short, a long integration time is necessary to obtain a strong signal: about 15 minutes signal acquisition is needed for a sound spectrum when the excitation time is  $20\ \mu\text{s}$ . This may cause an additional out-of-focus effect due to the backlash of the sample stage and vibration in the environment. Moreover, the deficiency in the square pulse of the modulated laser will lower the temperature rise of the shortest excitation time. The modulated laser has a rising time of  $0.13\ \mu\text{s}$ . Though the total amount of thermal input is fixed, the heating rate is slower at the beginning of the excitation period than the rest and the temperature of the cantilever correspondingly rises slower in the beginning. Due to the fact that Raman intensity is highly sensitive to temperature, the instant intensity in the pulse rising time will increase the average intensity of the entire excitation period. When  $t_e$  is as short as  $20\ \mu\text{s}$ , the rising time will result  $\sim 1\%$  increase in the average temperature and the Raman intensity. When  $t_e$  is being longer in our experiment, the effect of the rising time becomes negligible. Therefore, the total variation in  $E_{\omega}^*$  is, to some extent, increased and so as  $\bar{\theta}_{E_{\omega}^*}$ . But the increase in  $\Delta E_{\omega}^*$  will “stretch” the real curve and accelerate the changing rate of the curve, and thus cause the 5.9% deviation in the measured  $\alpha_{E_{\omega}^*}$  of  $9.17\times 10^{-5}\ \text{m}^2/\text{s}$  from the reference thermal diffusivity of  $8.66\times 10^{-5}\ \text{m}^2/\text{s}$ .

In Fig. 5.5b, the total wavenumber shift is about  $2.8 \text{ cm}^{-1}$ . It is several times larger than the broadening in the linewidth, though the temperature coefficient for the wavenumber is just twice that for the linewidth. The total shift of wavenumber is the combined result from not only the sole temperature rise but also the thermal stress and other factors in the cantilever. We could not directly evaluate  $\bar{\theta}_\omega$ , but our model is still applicable for fitting the variation of the wavenumber shift. The stress and other possible factors could approximate to a first-order function of  $q$  to simplify the fitting process. They are all included in constant  $B$  in a determination in Eq. 5.8. The best fitted result  $a_w$  is  $8.14 \times 10^{-5} \text{ m}^2/\text{s}$ . It is 5.8% lower than the reference value of  $8.66 \times 10^{-5} \text{ m}^2/\text{s}$ .

The thermal radiation and convection effect in the determined thermal diffusivity of the cantilever can be evaluated with the equation of  $(8\varepsilon\sigma T_0^3 + 4h)L^2 / (\rho c_p D\pi^2)$  [76, 102].  $r$ ,  $c_p$ , and  $e$ , are density ( $2330 \text{ kg/m}^3$ ), specific heat ( $712 \text{ J/kg}\cdot\text{K}$ ), and emissivity ( $< 0.1$ ) of bulk Si at room temperature.  $h$  is the free convection coefficient, which is about  $1\sim 2 \text{ W/m}^2\cdot\text{K}$  at  $300\text{K}$ .  $L$  and  $D$  are the length ( $438.9 \text{ mm}$ ) and the thickness ( $2.5 \text{ mm}$ ) of the Si cantilever. The thermal radiation and convection effect will give a negligible error of  $\sim 4.8 \times 10^{-8} \text{ m}^2/\text{s}$  in the determined thermal diffusivity.

### 5.7. Thermal diffusivity determination based on total Raman emission

Raman peak intensity is a typical property representing the Raman scattering efficiency of a material. However, with the existence of the incident light broadening, heating effects, surface refraction and reflection, and detector efficiency, additional references and calibrations are needed if the intensity is used to analyze the Raman emission [103, 104]. Furthermore, in the

numerical model, the Raman spectrum is a complex composition of the peak intensity, the wavenumber and the linewidth. Each property will affect the determination of the other two. It is also very time consuming to reconstruct spectra for all excitation duties in the experiment.

Instead of using the Raman peak intensity, the Raman peak area could be an alternative property to evaluate the total Raman emission over the whole wavenumber range of the peak. In this model, since the total Raman emission is used, the Raman wavenumber shift is not needed. In this section, we develop a simplified physical model on the basis of the total Raman emission to fit the thermal diffusivity of the Si cantilever. The Raman peak area is proportional to the product of the linewidth and the peak intensity in the Gaussian function. The Raman wavenumber shift is not taken into consideration. In experimental data processing, the normalization is first conducted to divide the Raman peak area by the total irradiation time. This normalized peak area indicates the average Raman emission per unit time in the excitation period. It is also related to the average temperature rise in the Si cantilever. The normalized total Raman emission,  $E^*$ , is simplified as:

$$E^* = \frac{A_0'}{t_e} \int_0^{t_e} (1 - A\bar{\theta}^*)(\Gamma_0 + C\bar{\theta}^*) dt, \quad (11)$$

$A_0'$  is a multiple compensating for the difference in the peak area between the normalized experimental data and the average fitting result. It is determined by comparing experimental data with theoretical data at the steady state. As the same to  $A_0$ ,  $A_0'$  is less significant to us while the relative variation of the peak area is more useful. Constants  $\Gamma_0$  and  $C$  are directly extracted from the linewidth variation of the experimental spectra, and take the values indicated above ( $\Gamma_0 = 11.06 \text{ cm}^{-1}$  and  $C = 0.34 \text{ cm}^{-1}$ ).

$A$  and  $C$  are the changing rates of the normalized peak intensity and linewidth against the excitation time. Based on the  $A$  value extracted from Fig. 5.3b, refinement is also conducted together with the determination  $\alpha$  in the peak area fitting process.  $A$  is varied from 0.1 to 0.4 with an increment of 1%. For each  $A$ ,  $\alpha$  is scanned from  $3 \times 10^{-5} \text{ m}^2/\text{s}$  to  $12 \times 10^{-5} \text{ m}^2/\text{s}$ . The best fitted values of  $A$  and  $\alpha_{E^*}$  are  $0.32 \text{ K}^{-1}$  and  $9.51 \times 10^{-5} \text{ m}^2/\text{s}$ , respectively, for constructing a theoretical curve that fits the experimental data best (Fig. 5.6). The value of  $A$  is very close to the one determined above based on the precise physical mode:  $0.31 \text{ K}^{-1}$ . In Fig. 5.6, error bars indicate the peak area measurement uncertainty and the blue and green curves with 10% deviation in  $\alpha$  illustrate the sensitivity of the total Raman emission method.

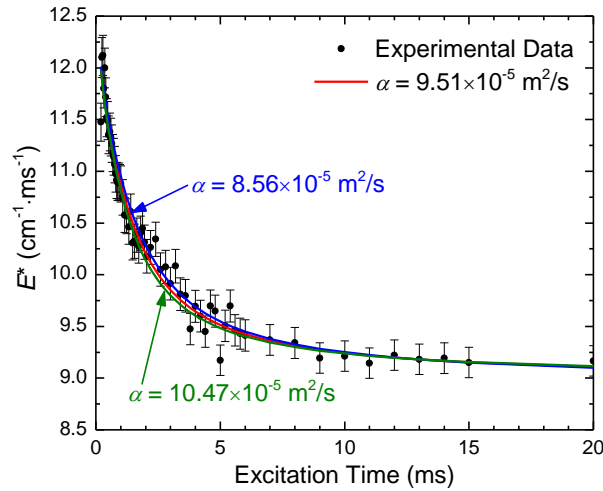


**Figure 5.6.** The experimental data fitting based on the peak area with the best fitted curve with  $\alpha_{E^*} = 9.51 \times 10^{-5} \text{ m}^2/\text{s}$ . The measurement uncertainty is shown using error bars. The sensitivity of the total Raman emission method to  $\alpha$  is shown with  $\alpha = 8.56 \times 10^{-5} \text{ m}^2/\text{s}$  and  $\alpha = 10.47 \times 10^{-5} \text{ m}^2/\text{s}$ , respectively. A visible deviation is observed from the best fitted result when  $\alpha$  changes with 10%.

Compared with the reference value in Section 5.5,  $\alpha_{E^*}$  from the total Raman emission method has a 10% deviation from  $\alpha_{\text{ref}}$ .  $\alpha_{E^*}$  has a larger error than those from the intensity

method and wavenumber method because it is the product of Raman intensity and linewidth. Errors of the normalized intensity and linewidth will be combined together during thermal diffusivity determination based on the peak area method. The advantage of the peak area fitting method (or total Raman emission method) is that it provides an alternative quick way to determine the thermal diffusivity of a material. The peak area method utilizes the linewidth variation against the excitation time. No other information is needed for the Raman wavenumber and shift. Thus, it avoids the Raman spectrum re-construction, which is very time consuming.

## CHAPTER 6

## SUMMARY AND FUTURE WORK

## 6.1. Summary

**6.1.1. Photothermal technique with amplitude profile**

An amplitude method for the PT technique has been successfully developed to analyze the thermal radiation signal from the surface of a multilayered sample. There CVD SiC film samples and a SiO<sub>2</sub> film sample on a silicon substrate were characterized using the amplitude method. The determined thermal conductivity based on the amplitude method is 3.58, 3.59, and 2.59 W/m K for SiC sample 1 to 3, respectively. The accuracy of the amplitude method was verified by comparing it with the reliable phase shift method. The resulting thermal conductivity of all SiC samples from the two methods agreed well with each other. For the SiO<sub>2</sub> film on Si substrate, the thermal conductivity is measured to be 1.68 W/m K which is a little higher than that determined by the phase shift method: 1.31 W/m K. The normalized amplitude ( $A_{nor}$ ) defined in our amplitude method is closely related to the effusivity of the film and substrate. The ratio of  $A_{nor}$  at a sufficiently high frequency to that at a low frequency provides a sound estimate of the effusivity ratio of the film to the substrate. In addition, the non-sensitive nature of thermal contact resistance in the amplitude method was observed through studying the sensitivity of parameters. The reason for weak sensitivity has been specifically discussed with the expression and physical meanings of interfacial transmission matrix. However, this feature allows for the amplitude method to fit the thermal conductivity of samples with little effect from the interfacial resistance in multilayered samples, and provides a reliable alternative to study the thermophysical properties of films in the thickness direction.

### 6.1.2. Cross-plane thermal transport in spider silk films

This study focused on the thermal transport capacity in the thickness direction for fresh films and HFIP films cast with major ampullate liquid silk protein of two spiders, *N. clavipes* and *L. hesperus*. Confocal Raman spectroscopy was conducted to characterize the structures of these samples, and the thermal properties were measured by using the PT technique. The fresh films had more crystalline secondary protein structures such as antiparallel  $\beta$ -sheets than the HFIP films for *N. clavipes*, but both films had similar thermal conductivities. A few randomly distributed antiparallel  $\beta$ -sheets in the fresh film had nearly no effect on the thermal conductivity. For *L. hesperus*, the films primarily consisted of  $\alpha$ -helices and random coils. Since the fresh film had a higher concentration of  $\alpha$ -helices than the HFIP film, its thermal conductivity and thermal capacity were larger than those of HFIP films. However, the effect of  $\alpha$ -helices on thermal conductivity increase is rather weak in comparison with its effect on heat capacity. Moreover, the thickened HFIP films were heated at different temperatures to study the effect of the heat treatment on the internal structure of spider silk films.  $\alpha$ -helices were formed during the heating process and the thermal effusivity increased when  $\alpha$ -helices appeared in the spectra for films of both kinds of spiders. Since the internal structures largely affect thermal conductivities of spider silk films, measuring thermal properties provides an alternative way to looking at the crystalline structures of spider silk proteins, their structure regularity, and energy coupling.

### 6.1.3. Raman spectroscopy for nanostructure probing

Raman spectroscopy was conducted for mechanically cleaved Si wafers of 270 and 7  $\mu\text{m}$  thicknesses. When the probe laser point was moved from the center to the cleaved edge by a distance of 1.75  $\mu\text{m}$ , a very surprising phenomenon was observed: the intensity of 521  $\text{cm}^{-1}$  peak

increased abnormally, up to 100%. Our careful study of the surface morphology near the edge by using AFM and SEM did not reveal change on the Si surface to explain such an abnormal intensity increase. Also, the out-of-focus effect was ruled out based on the observed wavenumber change and linewidth broadening. According to the Raman wavenumber change, the crystalline size within the Si wafer was evaluated. It changes from 20 to 10 nm when the laser point is moved from the center to the cleaved edge. Meanwhile, both the linewidth and wavenumber changed by about 2 and 4  $\text{cm}^{-1}$ , respectively. If instrument and surface effects are well defined, the change of Raman intensity could provide a sensitive and complementary way to characterize grain size.

#### **6.1.4. Time-domain differential Raman for thermal probing**

In this work, a time-domain differential Raman technology was successfully developed for probing and characterizing transient thermal transport in a tipless Si cantilever along the length direction. A physical model was first developed for describing the temperature evolution in the cantilever against the increased heating time. The variation of the Si Raman spectrum was also correlated with the normalized temperature rise through developing a precise physical model for Raman spectrum reconstruction. The thermal diffusivity of the cantilever was determined at  $9.17 \times 10^{-5}$ ,  $8.14 \times 10^{-5}$ , and  $9.51 \times 10^{-5}$   $\text{m}^2/\text{s}$  by fitting the variation of Raman peak intensity, wavenumber, and peak area against heating time. To evaluate this new technique, the real temperature rise (timely-and-spatially averaged for the thermal diffusivity) was calculated at 14 K. The corresponding reference thermal diffusivity  $\alpha_{\text{ref}}$  is  $8.66 \times 10^{-5}$   $\text{m}^2/\text{s}$ . All three determined results were very close to the reference value. The deviation was induced by the inaccurate definition of the initial state and the heat induced deflection and out-of-focus effect. The most

important advantage of the TD Raman technique is that the specific temperature of the sample at any instant is not needed to study its thermal transport. Only the normalized variation of the temperature rise is needed. Thus no calibration was conducted in this work. The normalized variation in the Raman intensity and wavenumber can be directly and accurately analyzed to determine the thermal diffusivity of the sample.

## 6.2. Future work: extended application of TD Raman

The TD Raman has successfully probed the transient thermal transport in a cantilever and characterized its thermal diffusivity without knowing the real temperature in the tipless Si cantilever (1D model). TD Raman can also be used for characterizing 2D or bulk materials besides 1D structure, if the lower limit of the excitation period could be even shorter. Currently, the minimum pulse width could be set to 260 ns, since the intrinsic rising time of the modulated laser pulse is 130 ns. It is too long to probe the transient thermal process in bulk materials, such as Si. On the other hand, the requirement of a sound Raman spectrum with the combination of a fixed relaxation time and the shortest excitation period ( $t_r = 10$  ms and  $t_e = 20$   $\mu$ s) limits the further reduction of excitation cycle. Theoretically, the shortest excitation time of 260 ns could work if the integration time of the spectrum acquisition is long enough, the resulting stage drifting and environment vibrations, however, could not be negligible. They will significantly affect the precise measurement of the initial state and therefore increase the experimental errors in the determined thermal diffusivity. An ultrafast laser source (picosecond) is preferred in future to reduce the minimum excitation time, to increase the TD Raman probing capacity, and to further broaden its applications to bulk materials.

In addition to characterizing the thermophysical properties of bulk materials, TD Raman is also promising in probing the thermal transport across interfaces. Compared with our previous Raman technology, TD Raman overcomes the drawbacks of other Raman thermometry techniques and has the capacity of characterizing the interfaces of high thermal conductance. To manifest the advantage of TD Raman, a laser irradiates an interface composed of a top layer and a substrate. Both the top layer and the bottom substrate will be heated by the laser. The temperature rising rates, however, are different in the two substances due to their different thermal diffusivities, and lead to a temperature difference across the interface. The interface thermal conduction happens immediately and soon reaches the steady state leading to a constant interfacial temperature difference, while both the top layer and the substrate need more time to reach the steady state.

In the case of studying the interface of small contact thermal resistance, a large thermal energy input is necessary to generate a detectable temperature difference across the interface. For the measurement at the steady state, like most Raman thermometry techniques do, the large thermal energy is inevitably accumulated over the spectra integration time in the top layer. The resulting high temperature rise will damage the top layer, especially the one with a low thermal conductivity. In contrast, using a transient Raman laser, the measurement of the interface thermal conduction can be done in the duration when the interface has been thermally steady, yet the layer and the substrate do not reach the steady state. The thermal energy accumulation will be interrupted by the followed relaxation period that prevents the layer's temperature from rising too high. Meanwhile the high repetition rate of the ultrafast laser will guarantee the sufficiently

strong signals in the Raman spectra. This remarkable feature will widely broaden the application of the TD Raman to the study of interface between 2D materials and substrates.

## REFERENCES

1. T.Y. Choi, D. Poulikakos, J. Tharian, and U. Sennhauser, Measurement of thermal conductivity of individual multiwalled carbon nanotubes by the 3-omega method. *Applied Physics Letters*, 2005. **87**(1): p. 013108.
2. T.Y. Choi, D. Poulikakos, J. Tharian, and U. Sennhauser, Measurement of the thermal conductivity of individual carbon nanotubes by the four-point three-omega method. *Nano Letters*, 2006. **6**(8): p. 1589-1593.
3. L. Lu, W. Yi, and D.L. Zhang, 3 omega method for specific heat and thermal conductivity measurements. *Review of Scientific Instruments*, 2001. **72**(7): p. 2996-3003.
4. S. Sporlein, H. Carstens, H. Satzger, C. Renner, R. Behrendt, L. Moroder, P. Tavan, W. Zinth, and J. Wachtveitl, Ultrafast spectroscopy reveals subnanosecond peptide conformational dynamics and validates molecular dynamics simulation. *Proceedings of the National Academy of Sciences of the United States of America*, 2002. **99**(12): p. 7998-8002.
5. O.J. Korovyanko, C.X. Sheng, Z.V. Vardeny, A.B. Dalton, and R.H. Baughman, Ultrafast spectroscopy of excitons in single-walled carbon nanotubes. *Physical Review Letters*, 2004. **92**(1): p. 017403.
6. C. Thomsen, H.T. Grahn, H.J. Maris, and J. Tauc, Surface Generation and Detection of Phonons by Picosecond Light-Pulses. *Physical Review B*, 1986. **34**(6): p. 4129-4138.
7. M. Ducouso, T. Dehoux, C. Rossignol, B. Audoin, O. Zouani, C. Chollet, C. Chanseau, and M.C. Durrieu, Two color probing of the ultrafast photo-acoustic response in a single biological cell. *Journal of Physics: Conference Series*, 2011. **278**(1): p. 012042.
8. R. Anastasi, *Ultrasonic and advanced methods for nondestructive testing and material characterization*. Terahertz NDE for aerospace applications, ed. C. Chen. 2007: World Scientific Publishing. 279-303.
9. C.A. Paddock and G.L. Eesley, Transient Thermorefectance from Thin Metal-Films. *Journal of Applied Physics*, 1986. **60**(1): p. 285-290.
10. K. Ujihara, Reflectivity of Metals at High-Temperatures. *Journal of Applied Physics*, 1972. **43**(5): p. 2376-2383.
11. G.L. Eesley, Surface Raman Ellipsometry. *Ieee Journal of Quantum Electronics*, 1981. **17**(7): p. 1285-1292.
12. D.G. Cahill, P.V. Braun, G. Chen, D.R. Clarke, S.H. Fan, K.E. Goodson, P. Keblinski, W.P. King, G.D. Mahan, A. Majumdar, H.J. Maris, S.R. Phillpot, E. Pop, and L. Shi, Nanoscale thermal transport. II. 2003-2012. *Applied Physics Reviews*, 2014. **1**(1).
13. A. Rosencwaig and A. Gersho, Theory of Photoacoustic Effect with Solids. *Journal of Applied Physics*, 1976. **47**(1): p. 64-69.

14. S.D. Campbell, S.S. Yee, and M.A. Fromowitz, Applications of Photoacoustic-Spectroscopy to Problems in Dermatology Research. *Ieee Transactions on Biomedical Engineering*, 1979. **26**(4): p. 220-227.
15. N.C. Fernelius, Extension of the Rosencwaig-Gersho Photoacoustic-Spectroscopy Theory to Include Effects of a Sample Coating. *Journal of Applied Physics*, 1980. **51**(1): p. 650-654.
16. T. Fujii, K. Kumosaki, and M. Inoue, Analysis of Dynamic Diffuse Wall Based on Two-Dimensional Twist Wall. *Journal of Applied Physics*, 1981. **52**(3): p. 2350-2352.
17. J. Baumann and R. Tilgner, Determining Photothermally the Thickness of a Buried Layer. *Journal of Applied Physics*, 1985. **58**(5): p. 1982-1985.
18. H.P. Hu, X.W. Wang, and X.F. Xu, Generalized theory of the photoacoustic effect in a multilayer material. *Journal of Applied Physics*, 1999. **86**(7): p. 3953-3958.
19. X.W. Wang, Z.R. Zhong, and J. Xu, Noncontact thermal characterization of multiwall carbon nanotubes. *Journal of Applied Physics*, 2005. **97**(6): p. 064302.
20. T. Wang, X.W. Wang, Y.W. Zhang, L.Y. Liu, L. Xu, Y. Liu, L.J. Zhang, Z.Y. Luo, and K.F. Cen, Effect of zirconium(IV) propoxide concentration on the thermophysical properties of hybrid organic-inorganic films. *Journal of Applied Physics*, 2008. **104**(1): p. 013528.
21. X.W. Chen, Y.P. He, Y.P. Zhao, and X.W. Wang, Thermophysical properties of hydrogenated vanadium-doped magnesium porous nanostructures. *Nanotechnology*, 2010. **21**(5): p. 055707.
22. J.Q. Guo, X.W. Wang, D.B. Geohegan, and G. Eres, Thermal Characterization of Multi-Wall Carbon Nanotube Bundles Based on Pulsed Laser-Assisted Thermal Relaxation. *Functional Materials Letters*, 2008. **1**(1): p. 71-76.
23. J.Q. Guo, X.W. Wang, D.B. Geohegan, G. Eres, and C. Vincent, Development of pulsed laser-assisted thermal relaxation technique for thermal characterization of microscale wires. *Journal of Applied Physics*, 2008. **103**(11): p. 113505.
24. X.H. Feng, G.Q. Liu, S. Xu, H. Lin, and X.W. Wang, 3-dimensional anisotropic thermal transport in microscale poly(3-hexylthiophene) thin films. *Polymer*, 2013. **54**(7): p. 1887-1895.
25. F.K. Ko, S. Kawabata, M. Inoue, M. Niwa, S. Fossey, and J.W. Song, Engineering properties of spider silk. *Materials Research Society Symposium Proceedings*, 2001. **702**: p. U1.4.1.
26. J.C. Zemlin, *A study of the mechanical behavior of spider silks*. 1968, Collaborative Research, Inc.: Waltham, Massachusetts. p. 68.
27. M. Denny, The physical properties of spider's silk and their role in the design of orb-webs. *J Exp Biol*, 1976. **65**: p. 483-506.

28. L. Romer and T. Scheibel, The elaborate structure of spider silk Structure and function of a natural high performance fiber. *Prion*, 2008. **2**(4): p. 154-161.
29. G.H. Altman, F. Diaz, C. Jakuba, T. Calabro, R.L. Horan, J. Chen, H. Lu, J. Richmond, and D.L. Kaplan, Silk-based biomaterials. *Biomaterials*, 2003. **24**(3): p. 401-416.
30. A. Leal-Egaña and T. Scheibel, Silk-based materials for biomedical applications. *Biotechnology and Applied Biochemistry*, 2010. **55**(3): p. 155-167.
31. Y. Yang, X. Chen, Z.Z. Shao, P. Zhou, D. Porter, D.P. Knight, and F. Vollrath, Toughness of spider silk at high and low temperatures. *Advanced Materials*, 2005. **17**(1): p. 84-88.
32. P.M. Cunniff, S.A. Fossey, M.A. Auerbach, J.W. Song, D.L. Kaplan, W.W. Adams, R.K. Eby, D. Mahoney, and D.L. Vezie, Mechanical and thermal properties of dragline silk from the spider *Nephila clavipes*. *Polymers for Advanced Technologies*, 1994. **5**(8): p. 401-410.
33. E.M. Pritchard, A. Wilz, L. Tianfu, L. Jing-Quan, D. Boison, and D.L. Kaplan. *Sustained-release silk biomaterials for drug delivery and tissue engineering scaffolds*. in *Bioengineering Conference, 2009 IEEE 35th Annual Northeast*. 2009.
34. A.C. MacIntosh, V.R. Kearns, A. Crawford, and P.V. Hatton, Skeletal tissue engineering using silk biomaterials. *Journal of tissue engineering and regenerative medicine*, 2008. **2**(2-3): p. 71-80.
35. Y. Cao and B. Wang, Biodegradation of Silk Biomaterials. *International Journal of Molecular Sciences*, 2009. **10**(4): p. 1514-1524.
36. C.-C.R. Wang, *Chlorophyll and Silk-based Oxygen Producing Biomaterials for Tissue Engineering*, in *Department of Biomedical Engineering*. 2010, Tufts University: Medford, MA.
37. A. Ubaldo, D.P. Ilaria, C. Anna, and F. Gi, Will silk fibroin nanofiber scaffolds ever hold a useful place in Translational Regenerative Medicine? *Int J Burn Trauma*, 2011. **1**(1): p. 27-33.
38. H.J. Kim, U.-J. Kim, H.S. Kim, C. Li, M. Wada, G.G. Leisk, and D.L. Kaplan, Bone tissue engineering with premineralized silk scaffolds. *Bone*, 2008. **42**(6): p. 1226-1234.
39. D.B. Mergenthaler, M. Pietralla, S. Roy, and H.G. Kilian, Thermal-Conductivity in Ultraoriented Polyethylene. *Macromolecules*, 1992. **25**(13): p. 3500-3502.
40. C.L. Choy, Y.W. Wong, G.W. Yang, and T. Kanamoto, Elastic modulus and thermal conductivity of ultradrawn polyethylene. *Journal of Polymer Science Part B-Polymer Physics*, 1999. **37**(23): p. 3359-3367.
41. S. Shen, A. Henry, J. Tong, R.T. Zheng, and G. Chen, Polyethylene nanofibres with very high thermal conductivities. *Nature Nanotechnology*, 2010. **5**(4): p. 251-255.

42. M. Xu and R.V. Lewis, Structure of a Protein Superfiber - Spider Dragline Silk. *Proceedings of the National Academy of Sciences of the United States of America*, 1990. **87**(18): p. 7120-7124.
43. Z.Z. Shao, F. Vollrath, Y. Yang, and H.C. Thogersen, Structure and behavior of regenerated spider silk. *Macromolecules*, 2003. **36**(4): p. 1157-1161.
44. A. Renault, J.F. Rioux-Dube, T. Lefevre, S. Beaufils, V. Vie, F. Paquet-Mercier, and M. Pezolet, Structure and Mechanical Properties of Spider Silk Films at the Air-Water Interface. *Langmuir*, 2013. **29**(25): p. 7931-7938.
45. K. Spiess, S. Wohlrab, and T. Scheibel, Structural characterization and functionalization of engineered spider silk films. *Soft Matter*, 2010. **6**(17): p. 4168-4174.
46. D. Huemmerich, U. Slotta, and T. Scheibel, Processing and modification of films made from recombinant spider silk proteins. *Applied Physics a-Materials Science & Processing*, 2006. **82**(2): p. 219-222.
47. X.P. Huang, G.Q. Liu, and X.W. Wang, New Secrets of Spider Silk: Exceptionally High Thermal Conductivity and Its Abnormal Change under Stretching. *Advanced Materials*, 2012. **24**(11): p. 1482-1486.
48. Y.N. Yue, X.W. Chen, and X.W. Wang, Noncontact Sub-10 nm Temperature Measurement in Near-Field Laser Heating. *ACS Nano*, 2011. **5**(6): p. 4466-4475.
49. T.E. Beechem and J.R. Serrane, Raman Thermometry of Microdevices: Comparing Methods to Minimize Error. *Spectroscopy*, 2011. **26**(11): p. 36-44.
50. J.K. Rath, Low temperature polycrystalline silicon: a review on deposition, physical properties and solar cell applications. *Solar Energy Materials and Solar Cells*, 2003. **76**(4): p. 431-487.
51. Y. Kolic, R. Gauthier, M.A.G. Perez, A. Sibai, J.C. Dupuy, P. Pinard, R. M'Ghaieth, and H. Maaref, Electron powder ribbon polycrystalline silicon plates used for porous layer fabrication. *Thin Solid Films*, 1995. **255**(1-2): p. 159-162.
52. G.B. Tong, Z. Aspanut, M.R. Muhamad, and S. Abdul Rahman, Optical properties and crystallinity of hydrogenated nanocrystalline silicon (nc-Si:H) thin films deposited by rf-PECVD. *Vacuum*, 2012. **86**(8): p. 1195-1202.
53. S. Webster, D.N. Batchelder, and D.A. Smith, Submicron resolution measurement of stress in silicon by near-field Raman spectroscopy. *Applied Physics Letters*, 1998. **72**(12): p. 1478-1480.
54. M. Balkanski, R.F. Wallis, and E. Haro, Anharmonic Effects in Light-Scattering Due to Optical Phonons in Silicon. *Physical Review B*, 1983. **28**(4): p. 1928-1934.

55. G.S. Doerk, C. Carraro, and R. Maboudian, Temperature dependence of Raman spectra for individual silicon nanowires. *Physical Review B*, 2009. **80**(7): p. 1-4.
56. R. Tsu and J.G. Hernandez, Temperature-Dependence of Silicon Raman Lines. *Applied Physics Letters*, 1982. **41**(11): p. 1016-1018.
57. D.G. Cahill, K.E. Goodson, and A. Majumdar, Thermometry and Thermal Transport in Micro/Nanoscale Solid-state Devices and Structures. *Journal of Heat Transfer-Transactions of the ASME*, 2002. **124**(2): p. 223-241.
58. J.R. Serrano and S.P. Kearney, Time-Resolved Micro-Raman Thermometry for Microsystems in Motion. *Journal of Heat Transfer-Transactions of the ASME*, 2008. **130**(12): p. 122401.
59. L. Song, W.J. Ma, Y. Ren, W.Y. Zhou, S.S. Xie, P.H. Tan, and L.F. Sun, Temperature Dependence of Raman Spectra in Single-walled Carbon Nanotube Rings. *Applied Physics Letters*, 2008. **92**(12): p. 121905.
60. T. Beechem, S. Graham, S.P. Kearney, L.M. Phinney, and J.R. Serrano, Invited Article: Simultaneous Mapping of Temperature and Stress in Microdevices using Micro-Raman Spectroscopy. *Review of Scientific Instruments*, 2007. **78**(6): p. 061301-9.
61. N. Lundt, S.T. Kelly, T. Rodel, B. Remez, A.M. Schwartzberg, A. Ceballos, C. Baldasseroni, P.A.F. Anastasi, M. Cox, F. Hellman, S.R. Leone, and M.K. Gilles, High Spatial Resolution Raman Thermometry Analysis of TiO<sub>2</sub> Microparticles. *Review of Scientific Instruments*, 2013. **84**(10): p. 104906.
62. A.A. Balandin, S. Ghosh, W. Bao, I. Calizo, D. Teweldebrhan, F. Miao, and C.N. Lau, Superior Thermal Conductivity of Single-Layer Graphene. *Nano Letters*, 2008. **8**(3): p. 902-907.
63. S.S. Chen, Q.Z. Wu, C. Mishra, J.Y. Kang, H.J. Zhang, K.J. Cho, W.W. Cai, A.A. Balandin, and R.S. Ruoff, Thermal conductivity of isotopically modified graphene. *Nature Materials*, 2012. **11**(3): p. 203-207.
64. Q.W. Li, C.H. Liu, X.S. Wang, and S.S. Fan, Measuring the Thermal Conductivity of Individual Carbon Nanotubes by the Raman Shift Method. *Nanotechnology*, 2009. **20**(14): p. 145702.
65. E. Chavez-Angel, J.S. Reparaz, J. Gomis-Bresco, M.R. Wagner, J. Cuffe, B. Graczykowski, A. Shchepetov, H. Jiang, M. Prunnila, J. Ahopelto, F. Alzina, and C.M.S. Torres, Reduction of the Thermal Conductivity in Free-standing Silicon Nano-membranes Investigated by Non-invasive Raman Thermometry. *APL Materials*, 2014. **2**(1): p. 012113.
66. Z. Yan, C. Jiang, T.R. Pope, C.F. Tsang, J.L. Stickney, P. Goli, J. Renteria, T.T. Salguero, and A.A. Balandin, Phonon and Thermal Properties of Exfoliated TaSe<sub>2</sub> Thin Films. *Journal of Applied Physics*, 2013. **114**(20): p. 204301.

67. S. Sahoo, A.P.S. Gaur, M. Ahmadi, M.J.F. Guinel, and R.S. Katiyar, Temperature-Dependent Raman Studies and Thermal Conductivity of Few-Layer MoS<sub>2</sub>. *Journal of Physical Chemistry C*, 2013. **117**(17): p. 9042-9047.
68. Y.N. Yue, J.C. Zhang, and X.W. Wang, Micro/Nanoscale Spatial Resolution Temperature Probing for the Interfacial Thermal Characterization of Epitaxial Graphene on 4H-SiC. *Small*, 2011. **7**(23): p. 3324-3333.
69. X.D. Tang, S. Xu, and X.W. Wang, Corrugated Epitaxial Graphene/SiC Interfaces: Photon Excitation and Probing. *Nanoscale*, 2014. **6**(15): p. 8822-30.
70. X.D. Tang, S. Xu, J.C. Zhang, and X.W. Wang, Five Orders of Magnitude Reduction in Energy Coupling across Corrugated Graphene/Substrate Interfaces. *ACS Applied Materials & Interfaces*, 2014. **6**(4): p. 2809-2818.
71. X.D. Tang, S. Xu, and X.W. Wang, Nanoscale Probing of Thermal, Stress, and Optical Fields under Near-Field Laser Heating. *Plos One*, 2013. **8**(3): p. e58030.
72. X.D. Tang, S. Xu, and X.W. Wang, Thermal Probing in Single Microparticle and Microfiber Induced Near-field Laser Focusing. *Optics Express*, 2013. **21**(12): p. 14303-14315.
73. X.D. Tang, Y.N. Yue, X.W. Chen, and X.W. Wang, Sub-wavelength Temperature Probing in Near-field Laser Heating by Particles. *Optics Express*, 2012. **20**(13): p. 14152-14167.
74. S. Xu, X.D. Tang, Y.N. Yue, and X.W. Wang, Sub-micron Imaging of Sub-surface Nanocrystalline Structure in Silicon. *Journal of Raman Spectroscopy*, 2013. **44**(11): p. 1523-1528.
75. J.Q. Guo, X.W. Wang, and T. Wang, Thermal Characterization of Microscale Conductive and Nonconductive Wires using Transient Electrothermal Technique. *Journal of Applied Physics*, 2007. **101**(6): p. 063537.
76. H. Lin, S. Xu, X.W. Wang, and N. Mei, Significantly Reduced Thermal Diffusivity of Free-standing Two-layer Graphene in Graphene Foam. *Nanotechnology*, 2013. **24**(41): p. 415706.
77. G.Q. Liu, S. Xu, T.T. Cao, H. Lin, X.D. Tang, Y.Q. Zhang, and X.W. Wang, Thermally Induced Increase in Energy Transport Capacity of Silkworm Silks. *Biopolymers*, 2014. **101**(10): p. 1029-1037.
78. Z.L. Xu, S. Xu, X.D. Tang, and X.W. Wang, Energy Transport in Crystalline DNA Composites. *AIP Advances*, 2014. **4**(1): p. 017131.
79. C.A. Bennett and R.R. Patty, Thermal Wave Interferometry - a Potential Application of the Photo-Acoustic Effect. *Applied Optics*, 1982. **21**(1): p. 49-54.
80. D.R. Lide, *CRC Handbook of Chemistry and Physics*. Internet Version 2007, (87th Edition) ed. 2007, Boca Raton, FL: Taylor and Francis.

81. G. Yu., L. M.E., and R. S.L., *Properties of Advanced Semiconductor Materials GaN, AlN, SiC, BN, SiC, SiGe*. 2001, New York: John Wiley & Sons, Inc.
82. S. Nakashima and H. Harima, Raman investigation of SiC polytypes. *Physica Status Solidi a-Applied Research*, 1997. **162**(1): p. 39-64.
83. D.W. Feldman, J.H. Parker, W.J. Choyke, and L. Patrick, Phonon Dispersion Curves by Raman Scattering in Sic Polytypes 3C,4H,6H,15R,and 21R. *Physical Review*, 1968. **173**(3): p. 787-793.
84. P. Musumeci, F. Roccaforte, and R. Reitano, Angular distortion of Si clusters in a-SiC. *Europhysics Letters*, 2001. **55**(5): p. 674-678.
85. T. Lefevre, F. Paquet-Mercier, J.F. Rioux-Dube, and M. Pezolet, Review structure of silk by raman spectromicroscopy: from the spinning glands to the fibers. *Biopolymers*, 2012. **97**(6): p. 322-36.
86. M.E. Rousseau, T. Lefevre, L. Beaulieu, T. Asakura, and M. Pezolet, Study of protein conformation and orientation in silkworm and spider silk fibers using Raman microspectroscopy. *Biomacromolecules*, 2004. **5**(6): p. 2247-2257.
87. C. Vierra, Y. Hsia, E. Gnesa, S. Tang, and F. Jeffery, *Spider Silk Composites and Applications*, in *Metal, Ceramic and Polymeric Composites for Various Uses*, J. Cuppoletti, Editor. 2011, InTech.
88. M.L. Casem, D. Turner, and K. Houchin, Protein and amino acid composition of silks from the cob weaver, *Latrodectus hesperus* (black widow). *Int J Biol Macromol*, 1999. **24**(2-3): p. 103-8.
89. M.B. Hinman and R.V. Lewis, Isolation of a clone encoding a second dragline silk fibroin. *Nephila clavipes* dragline silk is a two-protein fiber. *J Biol Chem*, 1992. **267**(27): p. 19320-4.
90. A. Sponner, B. Schlott, F. Vollrath, E. Unger, F. Grosse, and K. Weisshart, Characterization of the protein components of *Nephila clavipes* dragline silk. *Biochemistry*, 2005. **44**(12): p. 4727-4736.
91. N.A. Ayoub and C.Y. Hayashi, Multiple recombining loci encode MaSp1, the primary constituent of dragline silk, in widow spiders (*Latrodectus*: Theridiidae). *Mol Biol Evol*, 2008. **25**(2): p. 277-86.
92. J. Magoshi, Thermally induced molecular structure transformation in silkworm silk. *Kobunshi Ronbunshu*, 1974. **31**(7): p. 463-465.
93. Z. Shao, F. Vollrath, J. Sirichaisit, and R.J. Young, Analysis of spider silk in native and supercontracted states using Raman spectroscopy. *Polymer*, 1999. **40**(10): p. 2493-2500.

94. T. Lefevre, M.E. Rousseau, and M. Pezolet, Protein secondary structure and orientation in silk as revealed by Raman spectromicroscopy. *Biophysical Journal*, 2007. **92**(8): p. 2885-2895.
95. M. Fukui, Y. Kuwamura, and O. Tada, Surface-Roughness Effect on Raman-Scattering from Surface-Polaritons. *Journal of the Physical Society of Japan*, 1982. **51**(8): p. 2568-2574.
96. I.H. Campbell and P.M. Fauchet, The Effects of Microcrystal Size and Shape on the One Phonon Raman-Spectra of Crystalline Semiconductors. *Solid State Communications*, 1986. **58**(10): p. 739-741.
97. P.M. Fauchet and I.H. Campbell, Raman-Spectroscopy of Low-Dimensional Semiconductors. *Crc Critical Reviews in Solid State and Materials Sciences*, 1988. **14**: p. S79-S101.
98. H. Richter, Z.P. Wang, and L. Ley, The One Phonon Raman-Spectrum in Microcrystalline Silicon. *Solid State Communications*, 1981. **39**(5): p. 625-629.
99. J. Zi, H. Buscher, C. Falter, W. Ludwig, K.M. Zhang, and X.D. Xie, Raman shifts in Si nanocrystals. *Applied Physics Letters*, 1996. **69**(2): p. 200-202.
100. S. Veprek, F.A. Sarott, and Z. Iqbal, Effect of Grain-Boundaries on the Raman-Spectra, Optical-Absorption, and Elastic Light-Scattering in Nanometer-Sized Crystalline Silicon. *Physical Review B*, 1987. **36**(6): p. 3344-3350.
101. N. Beck, P. Torres, J. Fric, Z. Remes, A. Poruba, H. Stuchlikova, A. Fejfar, N. Wyrsh, M. Vanecek, J. Kocka, and A. Shah, Optical and electrical properties of undoped microcrystalline silicon deposited by the VHF-GD with different dilutions of silane in hydrogen. *Proc Mater Res Soc Symp* 1997. **452**: p. 761-766.
102. G.Q. Liu, H. Lin, X.D. Tang, K. Bergler, and X.W. Wang, Characterization of Thermal Transport in One-dimensional Solid Materials. *Journal of Visualized Experiments* 2014(83): p. e51144.
103. P. Klar, E. Lidorikis, A. Eckmann, I.A. Verzhbitskiy, A.C. Ferrari, and C. Casiraghi, Raman Scattering Efficiency of Graphene. *Physical Review B*, 2013. **87**(20): p. 205435-12.
104. M. Cardona, *Light Scattering in Solids II*. Topics in Applied Physics, ed. M. Cardona and G. Guntherodts. Vol. 50. 1982, Berlin: Springer.